Modelling of High-Speed Chemically Reactive Flows



Ruixuan Zhu

Exeter College

University of Oxford

A thesis submitted for the degree of

Doctor of Philosophy

Hilary 2024

Dedicated to my family

Acknowledgements

First and foremost, my profound thanks go to Prof. Martin Davy, my supervisor, for his patient guidance and encouragement throughout the journey of completing the thesis. I extend my appreciation to other academics in the Thermal Propulsion Systems Research Group (TPSRG), Prof. Richard Stone, Prof. Felix Leach, Prof. Ben Williams, and Prof. Konstantina Vogiatzaki for their insightful feedback on my work.

In the wider academic community, Prof. Huangwei Zhang, Prof. Xiaohang Fang, Prof. Zhiwei Huang, Prof. Majie Zhao, Dr. Chao Xu, Dr. Bifen Wu, Dr. Guangze Li, Prof. Shuyue Lai and Shizhi Tang have helped me a great deal as collaborators and co-authors.

The TPSRG has been a wonderful source of advice and friendship, and for that, I thank Varun Shankar, Samuel Baker, Tejo Jehart, Qichi He, Samuel White, Dr. Li Shen, Dr. Nikola Sekularac, Dr. Priyav Shah, Dr. Abdullah Bajwa, Dr. Christopher Willman, Dr. Giovanni Tretola, Dr. Maruthi Mallardi, Dr. Hannah Rana, Dr. Kharthik Chakravarthy, Zifeng Weng, James Bradley and Daniel Bundred. I would also like to thank Adan Chen and Honora Driscoll for their warm friendship.

The Advanced Research Computing (ARC) team has been brilliant with technical support, and thank you for always patiently responding to my complaints about the long-waiting queue.

I am so grateful for the financial support that China Oxford Scholarship

Fund, Henry Lester Trust, and Great Britain China Educational Trust provided to me during my DPhil study.

Last, but by no means least, I owe deep gratitude to my family – my husband Shicheng, my parents Suhua and Zhen, and my brother Xuanyao for their endless love and support.

Abstract

A new numerical Eulerian-Lagrangian solver named AHISsprayDetFoam is developed towards accurate and efficient modelling of high-speed chemically reactive flows within the framework of OpenFOAM. AHISsprayDetFoam integrates modules of built-in OpenFOAM rhoCentralFoam and Lagrangian solvers, the mixture-averaged diffusion model, optimised droplet sub-models, and a sparse stiff chemistry solver based on dynamic adaptive hybrid integration (AHI-S). The optimised droplet sub-models are verified in correct implementation by simulating ammonia droplet acceleration and cooling in the flowing and/or low-temperature air. The accuracy and efficiency gains of AHISsprayDetFoam are examined by simulating 1-D detonation propagation in ammonia droplet-free/laden ammonia-oxygen mixtures. The mixture-averaged diffusion model provides different predictions of pulsating detonation instabilities compared to the built-in OpenFOAM diffusion model. It shows better accuracy in depicting the detonation structure within the droplet-free section attributed to improved multi-component diffusion modelling. The AHI-S chemistry solver reduces the computational cost by around 50% compared to the built-in OpenFOAM EulerImplicit solver. It achieves good accuracy in calculating detonation propagation speed within the droplet-free section under optimal efficiency.

2-D numerical simulations of detonation propagation and extinction in

ammonia droplet-laden premixed ammonia-oxygen gas are performed using AHISsprayDetFoam. The detonation propagation/extinction behaviour and two-phase gas-droplet interactions are dependent on initial droplet diameter and number density. The detonative combustion and droplet evaporative, accelerative, and heating effects are higher-intensity in the post-Mach stem region than in the post-incident wave region. The detonation wave degenerates into detonative spots which then decouple into shock and reaction fronts as quenches.

3-D large eddy simulations of a supersonic lifted hydrogen flame are performed using AHISsprayDetFoam. Impacts of Lewis number on autoignition locations and strengths, and flame structures and stabilisation are numerically observed. The impacts of Lewis number are related to mass and thermal diffusions predicted at fuel-coflow and/or coflow-ambient air mixing layers, rationalised by non-negligible mass and thermal diffusions compared to convection. Impacts of turbulent Schmidt and Prandtl numbers are minor as sub-grid scale mass and thermal diffusions are subordinate to filtered diffusion.

Contents

List of Figures **ix**

List of Tables **xvii**

List of Abbreviations **xviii**

1 Introduction **1**
1.1 Motivation 1
1.2 Objective and structure of the thesis 7
1.3 List of publications 9

2 Numerical Solver Development **10**
2.1 Overview 10
2.2 Eulerian governing equations 10
2.3 Lagrangian governing equations 14
2.4 AHI-S chemistry solver 20
2.5 Numerical implementation 26
2.6 Summary 30

3 Numerical Solver Validation **32**
3.1 Overview 32
3.2 Background 33
3.3 Optimised droplet sub-model implementation 33
3.4 1-D ammonia-oxygen detonation study 42
3.5 Diffusion model analysis 51
3.6 Computational cost reduction 65
3.7 Summary 72

4 2-D Ammonia-Oxygen Detonation Study **74**
4.1 Overview . . . 74
4.2 Background . . . 75
4.3 Computational configuration and validation . . . 80
4.4 Detonation propagation/extinction diagram . . . 85
4.5 Two-phase gas-droplet interaction . . . 91
4.6 Detonation extinction transient . . . 101
4.7 Summary . . . 105

5 3-D Supersonic Lifted Hydrogen Flame Study **107**
5.1 Overview . . . 107
5.2 Background . . . 108
5.3 LES governing equations . . . 115
5.4 Experimental and computational configurations . . . 117
5.5 Mesh resolution analysis . . . 122
5.6 Impacts of Lewis number . . . 125
5.7 Impacts of turbulent Schmidt and Prandtl numbers . . . 142
5.8 Summary . . . 151

6 Conclusions, Claims for Originality, and Future Work **154**
6.1 Conclusions . . . 154
6.2 Claims for originality . . . 158
6.3 Future work . . . 158

Bibliography **160**

List of Figures

2.1 Flowchart of the AHISsprayDetFoam solver showing data exchange between the built-in OpenFOAM rhoCentralFoam solver, the built-in OpenFOAM Lagrangian solver, and the AHI-S chemistry solver. 27

3.1 Numerical results of drag coefficient with respect to droplet Reynolds number predicted with optimised and built-in OpenFOAM drag coefficient sub-models against experimental data from Ref. [53]. The optimised sub-model is based on Eq. (10) from Ref. [27]. 35

3.2 Time histories of droplet velocity under different initial droplet diameters. 37

3.3 Numerical results of Nusselt number with respect to droplet Reynolds number predicted with optimised and built-in OpenFOAM convective heat transfer coefficient sub-models against experimental data from Refs. [54–56]. The optimised sub-model is based on Whitaker correlation [28]. 38

3.4 Time histories of droplet temperature under different initial droplet diameters. 39

3.5 Numerical results of (a) drag coefficient and (b) Nusselt number with respect to droplet Reynolds number predicted with the optimised drag coefficient sub-model based on Eq. (10) from Ref. [27] and convective heat transfer coefficient sub-model based on Whitaker correlation [28] under different initial droplet diameters against experimental data from Ref. [53] and Refs. [54–56], respectively. 41

3.6 Schematics of 1-D detonation propagation in NH_3-O_2 mixtures (a) before and (b) after the detonation enters the two-phase section. Circles: ammonia droplets; HS: hot spot; DW: detonation wave; SF: shock front; RF: reaction front; CS: contact surface. 43

3.7 Numerical, experimental, and analytical results of detonation velocity as functions of (a) equivalence ratio, ϕ, and (b) initial pressure, p_0, in NH_3-O_2 mixtures. C_{base}: the baseline case with $T_0 = 295$ K, $\phi = 1.0$, $p_0 = 71$ kPa. 45

3.8 Spatial distributions of (a) temperature and (b) density at 339 μs against the ZND structure predicted by SDToolbox [83] in the NH_3-O_2 mixture when $p_0 = 71$ kPa, $\phi = 1.0$, $T_0 = 295$ K. SF: the location of shock front; RF: the location of reaction front. 47

3.9 Spatial distributions of species mass fractions at 339 μs against the ZND structure predicted by SDToolbox [83] in the NH_3-O_2 mixture when $p_0 = 71$ kPa, $\phi = 1.0$, $T_0 = 295$ K. SF: the location of shock front; RF: the location of reaction front. Dotted curves show results from the present simulation; curves show results from SDToolbox [83]. 48

3.10 Spatial distribution of droplet Reynolds number at 517 μs in the NH_3-O_2 mixture when $p_0 = 71$ kPa, $\phi = 1.0$, $T_0 = 295$ K with perturbations from ammonia droplets when $N_{d,0} = 1 \times 10^{12}/m^3$. SF: the location of shock front; RF: the location of reaction front. 50

3.11 Comparisons of the spatial and temporal distributions of temperature (in K, first column) and pressure gradient (in Pa/m, second column) predicted with (a) mixture-averaged diffusion model and (b) built-in OpenFOAM diffusion model in the NH_3-O_2 mixture when $p_0 = 71$ kPa, $\phi = 1.0$, $T_0 = 295$ K. SF: shock front; RF: reaction front; CW: compression wave; EW: expansion wave; B_1, B_2, B_1^* and B_2^*: bifurcation points. 52

3.12 (a) Time histories of reaction front propagation speeds and comparisons of the spatial distributions of temperature and thermal diffusion term in energy equation predicted with mixture-averaged diffusion model and built-in OpenFOAM diffusion model at (b) 0.27 ms, (c) 0.278 ms, (d) 0.284 ms, (e) 0.285 ms and (f) 0.286 ms in the NH_3-O_2 mixture when $p_0 = 71$ kPa, $\phi = 1.0$, $T_0 = 295$ K. SF: the location of shock front; RF: the location of reaction front. 54

3.13 Comparisons of the spatial distributions of species diffusion term in species mass fraction equation predicted with mixture-averaged diffusion model and built-in OpenFOAM diffusion model at (a) 0.27 ms and (b) 0.284 ms in the NH_3-O_2 mixture when $p_0 = 71$ kPa, $\phi = 1.0$, $T_0 = 295$ K. RF: the location of reaction front. Curves show results with mixture-averaged diffusion model; dotted curves show results with built-in OpenFOAM diffusion model. 57

3.14 Comparisons of the spatial distributions of H_2 and H mass fractions predicted with mixture-averaged diffusion model and built-in OpenFOAM diffusion model against the ZND structure predicted by SDToolbox [83] in the NH_3-O_2 mixture when $p_0 = 71$ kPa, $\phi = 1.0$, $T_0 = 295$ K. SF: the location of shock front; RF: the location of reaction front. 58

3.15 Comparisons of the spatial and temporal distributions of gaseous temperature (in K, first column), pressure gradient (in Pa/m, second column) and droplet diameter (in μm, last column) predicted with (a) mixture-averaged diffusion model and (b) built-in OpenFOAM diffusion model in the NH_3-O_2 mixture when $p_0 = 71$ kPa, $\phi = 1.0$, $T_0 = 295$ K with perturbations from ammonia droplets when $N_{d,0} = 1 \times 10^{12}/\mathrm{m}^3$. SF: shock front; RF: reaction front; CW: compression wave; EW: expansion wave; B_1 and B_2: bifurcation points; CS: contact surface. 61

3.16 Spatial distributions of heat release rate, pressure and temperature at (a) 0.638 ms and (b) 0.64 ms in the NH_3-O_2 mixture when $p_0 = 71$ kPa, $\phi = 1.0$, $T_0 = 295$ K with perturbations from ammonia droplets when $N_{d,0} = 1 \times 10^{12}/\mathrm{m}^3$. SF: the location of shock front; RF: the location of reaction front; DF: the location of detonative front; CS: the location of contact surface. 62

3.17 Comparisons of the spatial distributions of mass, momentum, and energy exchange rates predicted with mixture-averaged diffusion model and built-in OpenFOAM diffusion model at (a) 0.636 ms, (b) 0.638 ms, (c) 0.64 ms in the NH_3-O_2 mixture when $p_0 = 71$ kPa, $\phi = 1.0$, $T_0 = 295$ K with perturbations from ammonia droplets when $N_{d,0} = 1 \times 10^{12}/m^3$. SF: the location of shock front; RF: the location of reaction front; DF: the location of detonative front; CS: the location of contact surface. 63

3.18 Comparisons of execution time per simulation step using AHI-S chemistry solver and built-in OpenFOAM EulerImplicit chemistry solver. 66

3.19 Dependence of averaged execution time per simulation step on the safety factor. 67

3.20 Spatial distributions of fast (a) species and (b) reaction numbers at 339 μs in the NH_3-O_2 mixture when $p_0 = 71$ kPa, $\phi = 1.0$, $T_0 = 295$ K under different safety factors. SF: the location of shock front; RF: the location of reaction front. 68

3.21 Spatial distributions of fast (a) species and (b) reaction numbers at 517 μs in the NH_3-O_2 mixture when $p_0 = 71$ kPa, $\phi = 1.0$, $T_0 = 295$ K with perturbations from ammonia droplets when $N_{d,0} = 1 \times 10^{12}/m^3$ under different safety factors. SF: the location of shock front; RF: the location of reaction front. 69

3.22 Patterns of nontrivial entries (black pixels) in Jacobians of fast chemistry subsets in (a) droplet-free and (b) droplet-laden NH_3-O_2 mixtures when $p_0 = 71$ kPa, $\phi = 1.0$, $T_0 = 295$ K when $\beta = 0.5$. 70

3.23 Dependences of detonation velocity and its relative error against CJ detonation velocity in percentage in the NH_3-O_2 mixture when $p_0 = 71$ kPa, $\phi = 1.0$, $T_0 = 295$ K on the safety factor. D_{CJ}: CJ detonation velocity predicted by SDToolbox [83]. 71

4.1 Schematic of 2-D computational domain filled with premixed NH_3-O_2 gas. Circles: ammonia droplets. 81

4.2 Numerical, experimental, and analytical results of detonation (a) velocity, D, and (b) cell width, λ, with respect to equivalence ratio, ϕ, in droplet-free premixed NH_3-O_2 gas. C_{base}: the baseline case with $\phi = 1.0$. 84

4.3 Diagram of detonation propagation and extinction in droplet-laden premixed NH_3-O_2 gas with different initial droplet number density, $N_{d,0}$, and diameter, d_0. Squares: propagation scenarios; Circles: extinction scenarios. 86

4.4 Trajectories of detonation peak pressure in (a) droplet-free and (b)-(d) droplet-laden premixed NH_3-O_2 gas with initial droplet diameter of $d_0 =$ 10 μm. RS: reignition spot. Blue arrows mark triple point collision and thus re-amplification on detonation front; White arrows mark detonation cell merging and splitting. 88

4.5 Trajectories of detonation peak pressure in droplet-laden premixed NH_3-O_2 gas with initial droplet number density of $N_{d,0} = 1.5 \times 10^{12}$ /m^3. RS: reignition spot. Blue arrows mark triple point collision and thus re-amplification on detonation front; White arrows mark detonation cell merging and splitting. 90

4.6 Time and volume averaged (a) droplet volume fraction, V_{fd}, and inter-phase (b) mass, S_{mass}, (c) momentum along x-direction, $S_{\text{momentum},x}$, and (d) energy exchange rates, $S_{\text{energy},x}$, in droplet-laden NH_3-O_2 gas as functions of initial droplet number density, $N_{d,0}$, (black circle scatters) and diameter, d_0, (blue square scatters) when detonation propagates from $x = 0.22$ to 0.24 m. 92

4.7 Spatial profiles of y-direction averages of (a) droplet volume fraction, V_{fd}, and inter-phase (b) mass, (c) x-direction momentum, and (d) energy exchange rates (denoted as S_{mass}, $S_{\text{momentum},x}$, and S_{energy}, respectively) along x-direction in droplet-laden NH_3-O_2 gas with initial droplet diameter of $d_0 = 10$ μm at 95 μs. DW and CS: the locations of detonation wave and contact surface, respectively, for Case C_5 with $N_{d,0} = 1.5 \times 10^{12}$ /m^3. 93

4.8 Spatial profiles of y-direction averages of (a) droplet volume fraction, V_{fd}, and inter-phase (b) mass, (c) x-direction momentum, and (d) energy exchange rates (denoted as S_{mass}, $S_{\text{momentum},x}$, and S_{energy}, respectively) along x-direction in droplet-laden NH_3-O_2 gas with initial droplet number density of $N_{d,0} = 1.5 \times 10^{12}$ /m^3 at 95 μs. DW and CS: the locations of detonation wave and contact surface, respectively. . . . 95

4.9 Spatial distributions of gaseous ammonia volume fraction, X_{NH_3}, x-direction velocity, u_x, and temperature, T, in droplet-laden NH_3-O_2 gas with initial droplet density number and diameter of $N_{d,0} = 1.5 \times 10^{12}$ /m^3 and $d_0 = 10$ μm at (a) 95, (b) 105, and (c) 115 μs. DW: detonation wave; RF: reaction front; SF: shock front; DS: detonative spot; MS: Mach stem; IW: incident wave; TP: triple point. . 97

4.10 Spatial distributions of droplet diameter, d, x-direction velocity, $u_{d,x}$, and temperature, T_d, in droplet-laden NH_3-O_2 gas with initial droplet density number and diameter of $N_{d,0} = 1.5 \times 10^{12}$ /m^3 and $d_0 = 10$ μm at (a) 95, (b) 105, and (c) 115 μs. CS: contact surface. 98

4.11 Spatial profiles of (a) gaseous ammonia volume fraction, X_{NH_3}, and droplet diameter, d, (b) gaseous x-direction velocity, u_x, and droplet x-direction velocity, $u_{d,x}$, and (c) gaseous temperature, T, and droplet temperature, T_d, along x-direction in droplet-laden NH_3-O_2 gas with initial droplet density number and diameter of $N_{d,0} = 1.5 \times 10^{12}$ /m^3 and $d_0 = 10$ μm at 115 μs. MS: the location of Mach stem; IW: the location of incident wave; RF: the location of reaction front. 100

4.12 Evolution of schlieren fields during detonation extinction in droplet-laden premixed NH_3-O_2 gas with initial droplet density number and diameter of $N_{d,0} = 2.0 \times 10^{12}$ /m^3 and $d_0 = 10$ μm. DW: detonation wave; DS: detonative spot; SF: shock front; RF: reaction front. 102

4.13 Spatial profiles of y-direction averaged (a) gaseous heat release rate, $\dot{\omega}_T$, (b) gaseous pressure, p, and (c) gaseous nitric oxide volume fraction, X_{NO}, in droplet-laden NH_3-O_2 gas with initial droplet density number and diameter of $N_{d,0} = 2.0 \times 10^{12}$ /m^3 and $d_0 = 10$ μm. 104

5.1 (a) Schematic of Cheng supersonic flame burner [140], (b) experimental visual long exposure photograph [140], (c) 2-D schematic of cylindrical computational domain [74], and (d) local enlarged mesh around fuel and coflow inlets [74]. Reproduced with permission from Combust. Flame. 99, 157–173 (1994) and Combust. Flame. 238, 111756 (2022). Copyright Elsevier Inc. 118

5.2 Instantaneous scatter plots of the ratios between (a) SGS and molecular dynamic viscosities and (b) SGS and chemical timescales against heat release rate coloured by temperature on the symmetry plane in the central region of $70D_f \times 5D_f \times 2\pi$. Case ID: C_0. 123

5.3 Instantaneous percentages of the ratios between (a) SGS and molecular dynamic viscosities and (b) SGS and chemical timescales in several ranges in the central region of $70D_f \times 5D_f \times 2\pi$ (blue bars) and over the whole computational domain (orange bars). Case ID: C_0. 124

5.4 Mean (left) and instantaneous (right) distributions of species mole fraction for (a1)-(a2) H_2, (b1)-(b2) O_2, (c1)-(c2) H_2O, (d1)-(d2) N_2, (e1)-(e2) OH, and (f1)-(f2) mixture fraction on the symmetry plane in the central region of $70D_f \times 10D_f \times 2\pi$. Case ID: C_0 (top) and C_1 (bottom). 126

5.5 Radial profiles of mean (a)-(e) species mole fractions and (f) mixture fraction at $x/D_f = 32.3$. 129

5.6 Radial profiles of mean (a)-(e) species mole fractions and (f) mixture fraction at $x/D_f = 43.1$. 130

5.7 Radial profiles of mean (a)-(e) species mole fractions and (f) mixture fraction at $x/D_f = 64.7$. 131

5.8 Centreline profiles of mean mixture fraction. 132

5.9 Instantaneous distributions of heat release rate at (a1)-(a2) 0.5 ms, (b1)-(b2) 0.525 ms, (c1)-(c2) 0.55 ms, (d1)-(d2) 0.575 ms, (e1)-(e2) 0.6 ms, (f1)-(f2) 0.625 ms, (g1)-(g2) 0.65 ms, (h1)-(h2) 0.675 ms, (i1)-(i2) 0.7 ms, (j1)-(j2) 0.725 ms, and (k1)-(k2) 0.75 ms on the symmetry plane in the central region of $(20-50)D_f \times 5D_f \times 2\pi$. Case ID: C_0 (top) and C_1 (bottom). 133

5.10 Temporal evolutions of (a) flame base location tracked by (b) maximum heat release rate. 134

5.11 Instantaneous distributions of signed flame index on the symmetry plane in the central region of $70D_f \times 10D_f \times 2\pi$. Case ID: C_0 (a) and C_1 (b). 137

5.12 Instantaneous scatter plots of species diffusion term against mole fraction for (a) H_2, (b) H, (c) OH, (d) H_2O, (e) O_2, and (f) N_2 on the symmetry plane in the central region of $70D_f \times 5D_f \times 2\pi$. Case ID: C_0 (black scatters) and C_1 (blue scatters). 138

5.13 Instantaneous (a) centreline profiles, (b1)-(b2) distributions on the symmetry plane in the central region of $70D_f \times 10D_f \times 2\pi$, and (c1)-(c3) radial profiles of thermal diffusion term at $x/D_f = 10.8$, 32.3 and 43.1. Case ID: C_0 (b1) and C_1 (b2). 139

5.14 Instantaneous percentages of the absolute values of ratios between species diffusion and convection terms for (a) H_2, (b) H, (c) OH, (d) H_2O, (e) O_2, (f) N_2, and (g) thermal diffusion and convection terms in several ranges in the central region of $70D_f \times 5D_f \times 2\pi$. Case ID: C_0. . 141

5.15 Mean (left) and instantaneous (right) distributions of (a1)-(a4) temperature (in K) and (b1)-(b4) axial velocity (in m/s) on the symmetry plane in the central region of $70D_f \times 10D_f \times 2\pi$. Case ID: C_0 (first column), C_2 (second column), C_3 (third column), and C_4 (last column). 145

5.16 Radial profiles of mean (a1)-(a2) axial velocity and (b1)-(b3) temperature. 146

5.17 Centreline profiles of mean temperature. 148

5.18 Instantaneous distributions of signed flame index on the symmetry plane in the central region of $70D_f \times 10D_f \times 2\pi$. Case ID: C_0 (a), C_2 (b), C_3 (c), and C_4 (d). 149

5.19 Instantaneous percentages of the absolute values of ratios between SGS and filtered species diffusion terms for (a) H_2, (b) H, (c) OH, (d) H_2O, (e) O_2, (f) N_2, and (g) thermal diffusion terms in several ranges in the central region of $70D_f \times 5D_f \times 2\pi$. Case ID: C_4. 150

List of Tables

5.1 Summary of LES studies on Cheng supersonic flame. QLC: Quasi-Laminar Chemistry; PDF: Probability Density Function; PaSR: Partially Stirred Reactor; PSR: Perfectly Stirred Reactor; MMC: Multiple Mapping Conditioning. 109

5.2 Flow conditions of fuel and coflow jets at the exit of Cheng supersonic flame burner. p is pressure; T is temperature; Re is Reynolds number; Ma is Mach number; X_{O_2}, X_{H_2O}, X_{N_2} and X_{H_2} are species mole fractions. 119

5.3 Boundary conditions of cylindrical computational domain. p is pressure; T is temperature; $\mathbf{u}$ is velocity; O_2, H_2O, N_2 and H_2 are species. 119

5.4 Parametric LES of Cheng supersonic flame. Le_i is Lewis number of i-th species; Sc_t is turbulent Schmidt number; Pr_t is turbulent Prandtl number. 121

List of Abbreviations

AHI Adaptive Hybrid Integration

AHI-S A sparse stiff chemistry solver based on dynamic adaptive hybrid integration

BDF Backward Differentiation Formula

CFD Computational Fluid Dynamics

CFL Courant-Friedrich-Lewy

CJ Chapman–Jouguet

CRD Continuous Rotating Detonation

CS Contact Surface

CSP Computational Singular Perturbation

CW Compression Wave

DF Detonative Front

DDT Deflagration-to-Detonation Transition

DNS Direct Numerical Simulation

DRG Directed Relation Graph

DS Detonative Spot

DW Detonation Wave

ER Equivalence Ratio

EW Expansion Wave

FVM Finite Volume Method

HRL Half Reaction Length

HRR Heat Release Rate

HS Hot Spot

IW Incident Wave

KNP Kurganov, Noelle and Petrova

KT Kurganov and Tadmor

LES Large Eddy Simulation

LHV Lower Heating Value

MMC Multiple Mapping Conditioning

MS Mach Stem

ODE Ordinary Differential Equation

PaSR Partially Stirred Reactor

PDE Partial Differential Equation

PDF Probability Density Function

PDEs Pulse Detonation Engines

PSR Perfectly Stirred Reactor

QLC Quasi-Laminar Chemistry

RANS Reynolds-Averaged Navier-Stokes

RDEs Rotating Detonation Engines

RF Reaction Front

SF Shock Front

SGS Sub-Grid Scale

TP Triple Point

TVD Total Variation Diminishing

ZND Zel'dovich-Neumann-Döring

Chapter 1

Introduction

1.1 Motivation

Computational Fluid Dynamics (CFD) is widely used in simulating and understanding the behaviour of chemically reactive flows. Among various CFD packages, OpenFOAM [1], an open-source C++ finite volume toolbox, is popular with many advantages, *e.g.*, its free availability, objected-orientated framework and convenience to add multi-physical modules [2]. A built-in OpenFOAM density-based solver, rhoCentralFoam [3], is popular for modelling of high-speed shock-laden non-reactive flows. The rhoCentralFoam solver uses second-order, semi-discrete, non-staggered, and central schemes of Kurganov and Tadmor (KT) [4] or Kurganov, Noelle and Petrova (KNP) [5] for co-located variables on a mesh of polyhedral cells. Its capability to accurately capture flow discontinuities from shock and expansion waves has been validated by Greenshields *et al.* [3] and also in Refs. [6–12]. OpenFOAM-based solvers developed from rhoCentralFoam

coupled with chemistry solvers, *e.g.*, rhoCentralRfFoam [6–8] and RYrhoCentralFoam [9–12], are increasingly used in supersonic and detonative combustion research studies. However, despite these efforts, some modules can improve the numerical accuracy and computational efficiency when applying rhoCentralFoam to simulate high-speed chemically reactive flows.

More physically solid diffusion models, *i.e.*, multi-component diffusion and mixture-averaged diffusion models, than the built-in OpenFOAM diffusion model are one of the modules. They provide a more accurate description of species viscosity, mass, and thermal diffusivities in multi-component mixtures in high-fidelity simulations of chemically reactive flows. The built-in OpenFOAM diffusion model where dynamic viscosity and thermal diffusivity are predicted using Sutherland's law [13] is oversimplified. Procedurally, the dynamic viscosity is calculated as a function of temperature based on user-defined coefficients, while the thermal conductivity is calculated in proportion to dynamic viscosity using the Eucken approximation [14], and the thermal diffusivity is obtained from the thermal conductivity. OpenFOAM then calculates the species diffusivity assuming unity Lewis number, and further estimates the species mass and thermal diffusive fluxes. However, physically, multi-component diffusion is much more complex. The diffusion velocity of a given species in a gas mixture not only depends on the local mixture composition, but also, due to collisions among different molecules, on the diffusion velocity of all the other species.

The multi-component diffusion and mixture-averaged diffusion models are available within commonly used chemical kinetics packages, *e.g.*, Cantera [15] and

CHEMKIN [16]. The multi-component diffusion model considers the mass diffusion velocity of a given species with distinct contributions from each species via their gradients in the mixture. The species' thermal diffusion velocity is considered with a contribution from the thermal gradient. It is considered the most precise diffusion model for multi-component mixtures, but its application in large-scale reacting flow problems is limited by its prohibitive computational cost resulting from matrix inversion [2, 17]. The mixture-averaged model is relatively time-saving and therefore frequently used. It assumes that a certain species' effective mass diffusivity is computed from binary diffusivities between this species and other species in the mixture. Therefore, the mixture-averaged diffusion model also outperforms the built-in OpenFOAM diffusion model in physical accuracy by accounting for the effects of collisions among different molecules on species diffusion velocities in multi-component mixtures. It has shown similar performances as the multi-component diffusion model in simulations of both laminar and turbulent flames [18, 19]. This work applies the mixture-averaged diffusion model for the evaluation of multi-component diffusion properties.

In addition, the module of physically sound numerical methods and sub-models for liquid droplets in two-phase gas-droplet flows is of great significance. Gas-droplet interactions, *i.e.*, mass, momentum, energy, and species exchanges, trigger considerable variations in chemico-physical properties of the gas phase where chemical reactions proceed [20]. Compared to shock-less flows, shock/expansion waves in high-speed shock-laden flows, especially reacting ones, can cause sharply evolving gas fields around droplets, which further affect droplet

dynamics, *i.e.*, heating and evaporating, and vice versa [9]. Therefore, computationally accurate prediction of liquid droplet dynamics in high-speed chemically reactive two-phase flows is necessitated.

Both Eulerian-Eulerian [21, 22] and Eulerian-Lagrangian methods [23–26] have been used to simulate the dispersed phase of droplets and also the surrounding continuous gas phase in high-speed chemically reactive flows. Both methods are available within the framework of OpenFOAM, with respective pros and cons. The Eulerian-Eulerian method is computationally efficient, while only statistically averaged quantities of droplets instead of individual droplet behaviours are calculated. It is more applicable to simulate flows with densely distributed droplets whose motion is controlled by collisions or contacts. The Eulerian-Lagrangian method is preferred in the modelling of flows with dilute droplets where fluid forces, *e.g.*, drag and pressure gradient forces, play dominant roles in droplets' motions. In this work, only dilute sprays are studied, and the Eulerian-Lagrangian method is thus adopted by incorporating the built-in OpenFOAM Lagrangian solver to solve the dispersed droplet phase into rhoCentralFoam. Instantaneous locations and properties, *e.g.*, diameter, velocity, temperature, and density, of droplets can be computed. In addition, the gas density and inter-phase velocity difference are high in shock-laden high-speed chemically reactive flows, especially detonative combustion. This would result in high droplet Reynolds numbers. Therefore, droplet drag coefficient and convective heat transfer coefficient sub-models in OpenFOAM standard libraries are optimised to fit in the modelling of droplets at high Reynolds numbers, based on

Refs. [27, 28].

Computationally time-saving chemistry solvers for combustion modelling with detailed chemistry in high-speed reacting flow simulations is another module. Detailed chemistry is key to capturing transient ignition/extinction processes in chemically reactive flow simulations, but is computationally expensive due to its large size and severe stiffness. Even with skeletal chemical kinetic mechanisms that can be accurately reduced from detailed mechanisms through, *e.g.*, Directed Relation Graph (DRG) based methods [29–34], stiffness cannot be completely removed [35]. Compared to the relatively long timescales associated with convection and diffusion, the extremely short timescales attributed to highly reactive radicals and fast reactions lead to intrinsically stiff Partial Differential Equations (PDE) in reacting flow simulations. Consequently, the direct use of explicit PDE solvers is strongly constrained unless accompanied by a sufficiently small integration time step to solve the very fast chemical (and diffusion) processes. Built-in OpenFOAM reacting flow solvers employ a first-order splitting scheme, termed as OF-splitting scheme hereafter [17], to separately solve the chemical and the non-chemical processes. In the first step, chemistry is solved by Ordinary Differential Equation (ODE) solvers for one time step, where the temporal evolution of the local thermo-chemical state is governed by chemical reactions only. This step will provide a non-stiff chemical source term. In the second step, OpenFOAM solves the composition's "real" local thermo-chemical state by integrating the non-chemical source terms over the time step along with the chemical term calculated from the first step. A stiff ODE solver is typically

required in the first step for chemistry integration when reasonably large time steps are used.

Conventional stiff ODE solvers, *e.g.*, Backward Differentiation Formula (BDF) based solvers such as VODE [36] and DASAC [37], and extrapolation based solvers such as SEULEX [38], are high-cost implicit ODE solvers. The built-in OpenFOAM reacting flow solvers use the SEULEX solver by default for stiff chemistry integration [39]. One difficulty of built-in OpenFOAM implicit ODE solvers is regarding Jacobian evaluation and LU decomposition which are the most time-consuming components. Another issue of the default solver is that it cannot fully capture ignition problems for complex fuels [2]. To alleviate these problems, in this work, a sparse stiff chemistry solver based on dynamic adaptive hybrid integration (AHI-S) [35] is implemented into rhoCentralFoam within the framework of OpenFOAM. The AHI-S solver combines sparse matrix techniques with the dynamic Adaptive Hybrid Integration (AHI) method [40]. It speeds up the stiff chemistry integration in two aspects. First, for each time step, AHI-S splits full chemistry into fast and slow components based on species timescales with the fast chemistry solved implicitly and the slow chemistry solved explicitly. Second, analytic and sparse Jacobians are used to reduce the time complexity of an ODE solver from $O(n^2)$, where n is the number of species, for small and intermediate mechanisms, and $O(n^3)$ for large mechanisms, to $O(n)$ for mechanisms with arbitrary size. The AHI-S chemistry solver has been proven to eclipse built-in OpenFOAM implicit chemistry solvers in computational efficiency with comparable accuracy in simulations of 0-D autoignition and unsteady

Perfectly Stirred Reactor (PSR), and 1-D unstrained flames [35, 41].

1.2 Objective and structure of the thesis

The objective of the thesis is to perform accurate and efficient modelling of high-speed chemically reactive flows within the framework of OpenFOAM. Towards this, the above-mentioned modules of the mixture-averaged diffusion model, the built-in OpenFOAM Lagrangian solver coupled with optimised droplet sub-models, and the AHI-S chemistry solver are integrated into the built-in OpenFOAM rhoCentralFoam solver to form a new numerical solver, AHISsprayDetFoam. The AHISsprayDetFoam solver is thus a compressible multi-component reactive two-phase gas-droplet flow solver based on the Eulerian-Lagrangian method. It is tested on computing droplet-free/laden detonation propagation processes and supersonic turbulent combustion. The structure of the thesis is organised as below.

In Chapter 2, the methodology for the AHISsprayDetFoam solver development is introduced. The built-in OpenFOAM rhoCentralFoam and Lagrangian solvers are combined to simulate high-speed two-phase gas-droplet mixtures. The mixture-averaged diffusion model and the optimised droplet sub-models are coupled with them, respectively, towards the accuracy of the solver. The AHI-S chemistry solver is implemented for combustion modelling towards the efficiency of the solver.

In Chapter 3, the numerical accuracy and computational efficiency of the AHISsprayDetFoam solver are examined. The optimised droplet sub-models are

verified in correct implementation by simulating ammonia droplet acceleration and cooling in the flowing and/or low-temperature air. The accuracy and efficiency gains related to the mixture-averaged diffusion model and the AHI-S chemistry solver are verified by simulating 1-D detonation propagation in ammonia droplet-free/laden ammonia-oxygen mixtures. The numerical results are validated against the corresponding experimental and analytical data.

In Chapter 4, the AHISsprayDetFoam solver is applied to numerical simulations of detonation propagation and extinction in two-phase gas-droplet ammonia fuel. Detonation propagation/extinction scenarios and two-phase gas-droplet interactions, affected by the initial ammonia droplet number density and diameter, are addressed. The droplet-laden detonation physico-chemical structure is computationally visualised, and the detonation extinction process is analysed.

In Chapter 5, the AHISsprayDetFoam solver is applied to large eddy simulations of a supersonic lifted hydrogen flame. The emphases are two-fold: the impacts of Lewis number and the impacts of turbulent Schmidt and Prandtl numbers on the supersonic turbulent flame and flow structures. The former is assessed by comparing numerical solutions using the mixture-averaged diffusion model and the unity-Lewis number assumption. The latter is assessed by comparing numerical solutions using different combinations of turbulent Schmidt and Prandtl numbers.

In Chapter 6, a summary of the key conclusions from the preceding chapters is presented, and recommendations for future work are provided.

1.3 List of publications

Part of the work in the thesis has been published or submitted for publication or presented. They include:

1. **R. Zhu**, Z. Huang*, C. Xu, X. Fang, H. Zhang and M. Davy*, "Large eddy simulation of a supersonic lifted hydrogen flame: impacts of Lewis, turbulent Schmidt and Prandtl numbers", Physics of Fluids 36, 075118 (2024).

2. **R. Zhu**, G. Li*, F. Leach* and M. Davy, "Numerical simulation of detonation propagation and extinction in two-phase gas-droplet ammonia fuel", International Journal of Hydrogen Energy 90, 218-229 (2024).

3. **R. Zhu**, Z. Huang*, C. Xu, B. Wu and M. Davy, "Integration and validation of some modules for modelling of high-speed chemically reactive flows in two-phase gas-droplet mixtures", Computers & Fluids 277, 106282 (2024).

Chapter 2

Numerical Solver Development

2.1 Overview

This chapter focuses on the methodology for the AHISsprayDetFoam solver development. The Eulerian governing equations of the gas phase, the Lagrangian governing equations of the liquid phase, and the AHI-S chemistry solver are detailed in Sections 2.2, 2.3, and 2.4, respectively, followed by their numerical implementation in Section 2.5. The summary of this chapter is provided in Section 2.6.

2.2 Eulerian governing equations

The Eulerian method treats the gas phase as a continuum. For typical compressible, chemically reactive flows, the governing equations of mass, momentum, species mass fractions, and energy for the gas phase, as well as the

ideal gas equation of state, are solved in an Eulerian frame of reference, read

$$\frac{\partial \rho}{\partial t} + \nabla \cdot (\rho \mathbf{u}) = S_{\text{mass}}, \tag{2.1}$$

$$\frac{\partial (\rho \mathbf{u})}{\partial t} + \nabla \cdot [\mathbf{u}(\rho \mathbf{u})] + \nabla p - \nabla \cdot \boldsymbol{\tau} = \mathbf{S}_{\text{momentum}}, \tag{2.2}$$

$$\frac{\partial (\rho Y_i)}{\partial t} + \nabla \cdot [\mathbf{u}(\rho Y_i)] - \nabla \cdot (\rho Y_i \mathbf{V}_i) = \dot{\omega}_i + S_{\text{species},i}, (i = 1, 2, \cdots, N-1), \tag{2.3}$$

$$\frac{\partial (\rho E)}{\partial t} + \nabla \cdot [\mathbf{u}(\rho E)] + \nabla \cdot (\mathbf{u} p) - \nabla \cdot (\boldsymbol{\tau} \cdot \mathbf{u}) - \nabla \cdot (k \nabla T) = \dot{\omega}_T + S_{\text{energy}}, \tag{2.4}$$

$$\rho = p \Big/ \left(R_u T \sum_i \frac{Y_i}{W_i} \right), \tag{2.5}$$

where t is the time; ρ, $\mathbf{u}$, p and T state for the gas density, velocity vector, pressure, and temperature, respectively. R_u in Eq. (2.5) is the universal gas constant. $\boldsymbol{\tau}$ in Eq. (2.2) is the viscous stress tensor and calculated by

$$\boldsymbol{\tau} = \mu \left[\nabla \mathbf{u} + (\nabla \mathbf{u})^{\mathrm{T}} - \frac{2}{3} (\nabla \cdot \mathbf{u}) \mathbf{I} \right], \tag{2.6}$$

with μ being the dynamic viscosity and $\mathbf{I}$ being the identity matrix. μ is obtained using the mixture-averaged diffusion model [16], which specifically follows Wilke mixing rule [42],

$$\mu = \sum_i \frac{\mu_i X_i}{\sum_j \Phi_{i,j} X_j}, \tag{2.7}$$

where μ_i is the dynamic viscosity of the i-th species. X_i and X_j refer to the mole fractions of the i-th and the j-th species, and $\Phi_{i,j}$ is given by

$$\Phi_{i,j} = \frac{\left[1 + \sqrt{\left(\frac{\mu_i}{\mu_j} \sqrt{\frac{W_j}{W_i}} \right)} \right]^2}{\sqrt{8} \sqrt{1 + W_i / W_j}}, \tag{2.8}$$

with W_i and W_j being the mole weights, and μ_i and μ_j being the dynamic viscosities of the i-th and the j-th species, respectively.

Y_i in Eq. (2.3) and Eq. (2.5) is the mass fraction of the i-th species with N being the number of chemical species. $\mathbf{V}_i$ accounts for the diffusion velocity of the i-th species and is related to the species' gradient using the mixture-averaged formula,

$$\mathbf{V}_i = -\frac{D_i}{Y_i}\nabla Y_i, \tag{2.9}$$

where D_i denotes the diffusivity of the i-th species, given by

$$D_i = -\frac{1 - Y_i}{\sum_{j\neq i} X_j/\mathcal{D}_{ji}}, \tag{2.10}$$

with $\mathcal{D}_{ji}$ being the binary diffusion coefficient between the j-th and the i-th species, estimated according to Takahashi correlation [43]. The governing equation of species mass fractions, Eq. (2.3), is solved for all species except the N-th species, an "inert species" (*e.g.*, argon). Obeying the law of conservation of mass, the mass fraction of the inert species is computed by subtracting the sum of other species' mass fractions from unity. Similarly, the diffusion velocity of the inert species is explicitly obtained by obeying that the net species diffusion flux is zero, reads

$$\sum_{i=1}^{N} \rho Y_i \mathbf{V}_i = 0. \tag{2.11}$$

In Eq. (2.4), the total non-chemical energy, E, is related to the sensible internal energy, e, by

$$E = e + \frac{|\mathbf{u}|^2}{2}, \tag{2.12}$$

and the mixture-averaged thermal conductivity, k, is given by

$$k = 0.5\left(\sum_i X_i k_i + \frac{1}{\sum_i X_i/k_i}\right), \tag{2.13}$$

where k_i states for the thermal conductivity of the i-th species, and is calculated together with the i-th species' dynamic viscosity, μ_i, by expressions based on Chapman-Enskog theory [44]. As the dynamic viscosity, μ, species-specific diffusivity, D_i, and thermal conductivity, k, are approximated using the mixture-averaged formula, non-unity Lewis, Schmidt, and Prandtl numbers are assigned. In addition, radiative heat transfer, Soret and Dufour effects are ignored in this work as they play secondary roles. Note that the real gas effect on high-speed chemically reactive flows is also not referred to in this work.

S_{mass}, $\mathbf{S}_{\text{momentum}}$, $S_{\text{species},i}$ and S_{energy} in Eqs. (2.1)-(2.4) refer to the source terms based on contributions from gas-droplet interactions, termed as mass, momentum, species, and energy exchange rates, respectively. More details about their calculations can be found in Section 2.3.

$\dot{\omega}_i$ in Eq. (2.3) refers to the chemical net production rate of i-th species, and the chemical heat release rate is represented by $\dot{\omega}_T$ in Eq. (2.4). The chemical terms, *i.e.*, $\dot{\omega}_i$ and $\dot{\omega}_T$, are solved using the AHI-S chemistry solver [35], which will be detailed in Section 2.4.

2.3 Lagrangian governing equations

The mass, momentum, energy, and species exchange rates of the two-way coupling between gas and liquid phases, S_{mass}, $\mathbf{S}_{\text{momentum}}$, S_{energy}, $S_{\text{species},i}$ in Eqs. (2.1)-(2.4), are estimated by

$$S_{\text{mass}} = -\frac{1}{V_c}\sum_{1}^{N_{d,c}} \dot{m}_d, \tag{2.14}$$

$$\mathbf{S}_{\text{momentum}} = -\frac{1}{V_c}\sum_{1}^{N_{d,c}} \left(\dot{m}_d \mathbf{u}_d + \mathbf{F}_d + \mathbf{F}_p\right), \tag{2.15}$$

$$S_{\text{energy}} = -\frac{1}{V_c}\sum_{1}^{N_{d,c}} \left(\dot{m}_d h_v + \dot{Q}_c\right), \tag{2.16}$$

$$S_{\text{species},i} = \begin{cases} S_{\text{mass}}, & \text{for the liquid species} \\ 0, & \text{for other species,} \end{cases} \tag{2.17}$$

where V_c and $N_{d,c}$ denote the volume of a CFD grid and the number of droplets in the grid. $\dot{m}_d$ is the evaporation rate of a droplet, given in Eq. (2.24) later. In Eq. (2.15), $-\dot{m}_d \mathbf{u}_d$ denotes the rate of momentum transfer due to droplet evaporation with $\mathbf{u}_d$ being the velocity of the droplet. $\mathbf{F}_d$ and $\mathbf{F}_p$ state for drag force and Pressure Gradient Force (PGF) exerted on the droplet, computed by Eq. (2.35) and Eq. (2.37), respectively, while other less effective forces *e.g.*, gravity and Magnus lift force, are neglected in this work. In Eq. (2.16), $\dot{Q}_c$ is the inter-phase convective heat transfer rate, given in Eq. (2.38); h_v refers to the total enthalpy of vapour at the droplet temperature, T_d, given in Eq. (2.44).

The Lagrangian method considers the liquid phase as dispersed spherical droplets. Note that interactions among the droplets *e.g.*, coalescence and collision,

are reasonably neglected assuming flows with dilute droplets whose volume fraction is typically less than 0.1% are simulated [20]. The governing equations for the liquid phase include the evolutions of mass, velocity, and temperature for each individual droplet and take the following forms,

$$\frac{dm_d}{dt} = \dot{m}_d, \tag{2.18}$$

$$\frac{d\mathbf{u}_d}{dt} = \frac{\mathbf{F}_d + \mathbf{F}_p}{m_d}, \tag{2.19}$$

$$c_{pd}\frac{dT_d}{dt} = \frac{\dot{Q}_c + \dot{Q}_l}{m_d}, \tag{2.20}$$

where m_d is the mass of a single spherical droplet, related to the droplet density, ρ_d, and diameter, d, by

$$m_d = \frac{1}{6}\pi\rho_d d^3. \tag{2.21}$$

In Eq. (2.20), c_{pd} denotes the specific heat capacity of the droplet. Both ρ_d and c_{pd} are functions of the droplet temperature, T_d, representing the thermal expansion because of the heating of the droplet [45], read

$$\rho_d(T_d) = \frac{a_1}{a_2^{1+(1-T_d/a_3)^{a_4}}}, \tag{2.22}$$

$$c_{pd}(T_d) = b_1 + T_d\{b_2 + T_d\{b_3 + T_d[b_4 + T_d(b_5 + T_d b_6)]\}\}, \tag{2.23}$$

where a_1, a_2, a_3, a_4 and b_1, b_2, b_3, b_4, b_5, b_6 are species-specific constants [45].

The droplet evaporation rate, $\dot{m}_d$, in Eqs. (2.14)-(2.16) and Eq. (2.18) is approximated as [46]

$$\dot{m}_d = -\pi\rho_s d\mathcal{S}h D_{ab}\ln(1 + B_M), \tag{2.24}$$

where the Spalding mass transfer number, B_M, is determined by

$$B_M = \frac{Y_s - Y_g}{1 - Y_s}, \tag{2.25}$$

where Y_s and Y_g state for the vapour mass fractions at the droplet surface and in the surrounding gas phase, respectively. Y_s is obtained using

$$Y_s = \frac{W_d X_s}{W_d X_s + W_{ed}(1 - X_s)}, \tag{2.26}$$

where W_d is the mole weight of the vapour. W_{ed} denotes the averaged mole weight of the mixture excluding the vapour at the droplet surface. X_s is the vapour mole fraction at the droplet surface, calculated based on Raoult's law,

$$X_s = X_{\text{liq}} \frac{p_{\text{sat}}}{p_s}, \tag{2.27}$$

with X_{liq} being the mole fraction of the liquid species in the liquid phase. The saturated vapour pressure, p_{sat}, is a function of the droplet temperature, T_d, reads

$$p_{\text{sat}}(T_d) = p \exp\left(c_1 + \frac{c_2}{T_d} + c_3 \ln T_d + c_4 T_d^{c_5}\right), \tag{2.28}$$

and the equation is a revised version of the classical Clausius-Clapeyron equation with c_1, c_2, c_3, c_4, and c_5 being species-specific constants [45]. It adapts well to the data much above the normal boiling point and thus is expected to describe the droplet evaporation in shock-laden or reactive flows more accurately according to Refs. [47, 48]. Similarly, the vapour pressure at the droplet surface, p_s, is a function of the vapour temperature at the droplet surface, T_s, by

$$p_s(T_s) = X_{\text{liq}} p \exp\left(c_1 + \frac{c_2}{T_s} + c_3 \ln T_s + c_4 T_s^{c_5}\right), \tag{2.29}$$

where T_s is considered through the two-third rule [46],

$$T_s = \frac{2T_d + T}{3}. \tag{2.30}$$

The vapour density, ρ_s, in Eq. (2.24) is connected to the vapour pressure, p_s, and temperature, T_s, at the droplet surface by

$$\rho_s = \frac{p_s W_d}{R_u T_s}. \tag{2.31}$$

D_{ab} in Eq. (2.24) refers to the vapour mass diffusivity in the gas phase, computed by [49]

$$D_{ab} = 10^{-3} \frac{T_s^{1.75}}{p_s} \frac{\sqrt{W_d^{-1} + W^{-1}}}{\left(V_1^{1/3} + V_2^{1/3}\right)^2}, \tag{2.32}$$

where V_1 and V_2 are constants [50]; W is the mole weight of the gas. Equation (2.32) shows accuracy comparable to the Chapman-Enskog theory [44], besides, as the latter requires empirical parameters and simplifications, is more universal [50].

Sh in Eq. (2.24) is the Sherwood number, modelled by [51]

$$Sh = 2.0 + 0.6 Re_d^{1/2} Sc^{1/3}, \tag{2.33}$$

where $Sc = \mu/(\rho D_{ab})$ is the Schmidt number, and Re_d is the droplet Reynolds number, related to the slip velocity between gas and liquid phases by

$$Re_d \equiv \frac{\rho d \left|\mathbf{u} - \mathbf{u}_d\right|}{\mu}. \tag{2.34}$$

Since the droplets are assumed to be spherical, the drag force, $\mathbf{F}_d$, in Eq. (2.15) and Eq. (2.19) is predicted by [52]

$$\mathbf{F}_d = \frac{1}{8} \pi d^2 \rho C_d \left|\mathbf{u} - \mathbf{u}_d\right| (\mathbf{u} - \mathbf{u}_d), \tag{2.35}$$

with C_d being the drag coefficient. In the oversimplified built-in OpenFOAM drag coefficient sub-model, the functional form of C_d consists of power terms of Re_d when $Re_d \leq 1000$, while C_d is set as a constant, *i.e.*, 0.424, when $Re_d > 1000$ [52]. For subsequent simulations in this work, a drag coefficient sub-model whose prediction is optimised for droplets at high Reynolds numbers is desirable. As such, a series of functional forms of C_d proposed in Ref. [27] are pre-tested. The following one containing powers of logarithmic Re_d is selected, which shows the best accuracy against experimental data from Ref. [53], reads

$$C_d = d_1 + \frac{d_2}{Re_d} + d_3 \ln(Re_d) + d_4 \ln^2(Re_d) + d_5 \ln^4(Re_d), \tag{2.36}$$

where d_1, d_2, d_3, d_4 and d_5 are constants [27].

The PGF, F_p, in Eq. (2.15) and Eq. (2.19) stems from strong local pressure variations at rarefaction waves or shock discontinuities, solved by

$$\mathbf{F}_p = -\frac{1}{6}\pi d^3 \nabla p. \tag{2.37}$$

The inter-phase convective heat transfer rate, $\dot{Q}_c$, in Eq. (2.16) and Eq. (2.20) is calculated by

$$\dot{Q}_c = \pi d^2 h_c (T - T_d)\,, \tag{2.38}$$

where the convective heat transfer coefficient, h_c, is determined by the Nusselt number, Nu, where

$$Nu = \frac{h_c d}{k}, \tag{2.39}$$

and similar to that of C_d, a series of functional forms of Nu from Refs. [27, 28] are applied and validated. The Whitaker correlation between Nu and Re_d [28] with the

best performance against experimental data from Refs. [54–56] is utilised, such that

$$Nu = 2 + (e_1 Re_d^{e_2} + e_3 Re_d^{e_4}) Pr^{e_5}, \tag{2.40}$$

where e_1, e_2, e_3, e_4 and e_5 are constants [28], and $Pr = \mu c_p / k$ is the Prandtl number with c_p being the gas heat capacity at constant pressure.

The evaporation-induced heat transfer rate, $\dot{Q}_l$, in Eq. (2.20) is given by

$$\dot{Q}_l = -\dot{m}_d h_d, \tag{2.41}$$

where h_d denotes the latent heat of vaporization at the droplet temperature, T_d, and can be represented by [14]

$$h_d(T_d) = f_1 (1 - T_r)^{[(f_2 T_r + f_3) T_r + f_4] T_r + f_5}, \tag{2.42}$$

with f_1, f_2, f_3, f_4 and f_5 being species-specific constants [45], and T_r is computed by

$$T_r = \frac{T_d}{T_{\text{cr}}}, \tag{2.43}$$

where T_{cr} is the critical temperature.

The total enthalpy of vapour, h_v, in Eq. (2.16) is related to the droplet temperature, T_d, reads

$$h_v(T_d) = g_1 T_d^5 + g_2 T_d^4 + g_3 T_d^3 + g_4 T_d^2 + g_5 T_d + g_6, \tag{2.44}$$

with g_1, g_2, g_3, g_4, g_5 and g_6 being species-specific constants [45].

Note that a_1-a_4, b_1-b_6, c_1-c_5, f_1-f_5 and g_1-g_6 are species-specific constants [45] available in OpenFOAM standard libraries, while d_1-d_5 and e_1-e_5 are constants trained by available experimental data and data from well-known correlations from the literature in Refs. [27, 28].

2.4 AHI-S chemistry solver

To illustrate the OF-splitting scheme, the spatially discretized governing equations of species mass fractions and energy, *i.e.*, Eq. (2.3) and Eq. (2.4), are expressed in the following way,

$$\frac{d\boldsymbol{\Phi}}{dt} = \boldsymbol{\omega}(\boldsymbol{\Phi}) + \boldsymbol{s}(\boldsymbol{\Phi}), \tag{2.45}$$

where $\boldsymbol{\Phi} = (Y_i, T)^{\mathrm{T}}$ is the vector of dependent variables at all grid points in the multi-grid modelling, and its dimension is assumed to be n_Φ. $\boldsymbol{\omega}(\boldsymbol{\Phi})$ denotes the chemical term related to the chemical net production rate of i-th species and the chemical heat release, *i.e.*, $\dot{\omega}_i$ in Eq. (2.3) and $\dot{\omega}_T$ in Eq. (2.4); $\boldsymbol{s}(\boldsymbol{\Phi})$ denotes all non-chemical terms including the transport term (*i.e.*, the convection and diffusion terms) and the two-phase interaction source term.

The OF-splitting scheme is a first-order accurate splitting scheme by first integrating the chemical term by solving the following locally discretized ODE system with stiff ODE solvers,

$$\frac{d\boldsymbol{\Phi}^*}{dt} = \boldsymbol{\omega}(\boldsymbol{\Phi}^*), \tag{2.46}$$

and based on the first-step solution $\boldsymbol{\Phi}^*$, OpenFOAM then integrates the non-chemical term to calculate the composition's "real" local thermo-chemical state, *i.e.*, Y_i and T, by solving the following equation,

$$\frac{d\boldsymbol{\Phi}}{dt} = \frac{\boldsymbol{\Phi}^* - \boldsymbol{\Phi}_0}{\Delta t} + \boldsymbol{s}(\boldsymbol{\Phi}), \tag{2.47}$$

where Δt and $\boldsymbol{\Phi}_0$ refer to the integration time step and the initial values from the last time step, respectively.

In this work, the AHI-S chemistry solver [35] is implemented into AHISsprayDetFoam to achieve optimised efficiency for the solution of Eq. (2.46) in combustion modelling with finite-rate chemistry. Conventional stiff ODE solvers solve all dependent variables, $\mathbf{\Phi}$, in Eq. (2.46) implicitly. In the AHI-S chemistry solver, the fast chemistry, including fast species and reactions, is still solved implicitly, while the slow chemistry is solved explicitly with relatively low computational cost. The fast chemistry is identified on-the-fly with the AHI method [40] by reaction timescales defined in an analytic formulation of Computational Singular Perturbation (CSP) [57] as

$$\begin{aligned} \tau_k &\equiv \left| \frac{\partial \Omega_k}{\partial \boldsymbol{c}} \cdot \boldsymbol{\nu}_k \right|^{-1}, \\ \frac{\partial \Omega_k}{\partial \boldsymbol{c}} &= \left[\frac{\partial \Omega_k}{\partial c_1}, \frac{\partial \Omega_k}{\partial c_2}, \cdots, \frac{\partial \Omega_k}{\partial c_N} \right], \boldsymbol{\nu}_k = \left[\nu_{1,k}, \nu_{2,k}, \cdots, \nu_{N-1,k} \right]^{\mathrm{T}}, \\ &(k = 1, 2, \cdots, M), \end{aligned} \tag{2.48}$$

where τ_k and Ω_k refer to the timescale and reaction rate of the k-th chemical reaction. M is the total number of chemical reactions; N is the total number of chemical species as defined in Eq. (2.3). c_i denotes the mole concentration of the i-th species, and $\nu_{i,k}$ denotes the stoichiometric coefficient of the i-th species in the k-th reaction.

The k-th reaction is considered to be a fast one if

$$\tau_k < \tau_c / \beta, \tag{2.49}$$

where τ_c denotes a user-defined threshold timescale that is typically comparable to the integration time step, Δt. β is a safety factor that is typically mechanism-dependent. A value of 0.1-0.5 for β is recommended by Xu *et al.* [35]. The i-th

species is considered to be fast if the following criterion works for any fast reaction,

$$\left|\frac{\partial \Omega_k}{\partial c_i}\right| > \beta {\tau_c}^{-1}, (k = 1, 2, \cdots, M_f), \tag{2.50}$$

with M_f being the number of fast reactions.

The locally discretized ODE system, Eq. (2.46), can then be represented by

$$\begin{aligned} \frac{d\boldsymbol{\Phi}}{dt} &= \boldsymbol{\omega}_f(\boldsymbol{\Phi}) + \boldsymbol{\omega}_s(\boldsymbol{\Phi}), \boldsymbol{\Phi} = \begin{bmatrix} \boldsymbol{\Phi}_f \\ \\ \boldsymbol{\Phi}_s \end{bmatrix}, \\ \boldsymbol{\omega}_f &= \sum_{k=1}^{M_f} \boldsymbol{\nu}_k \Omega_k, \\ \boldsymbol{\omega}_s &= \sum_{k=M_f+1}^{M} \boldsymbol{\nu}_k \Omega_k, \end{aligned} \tag{2.51}$$

where $\boldsymbol{\Phi}_f$ and $\boldsymbol{\Phi}_s$ state for the fast and slow variables with dimensions of n_f and n_s, respectively. The ODE system in Eq. (2.51) can be further temporally discretized using a first-order Euler scheme and expressed by

$$\begin{bmatrix} \boldsymbol{\Phi}_f^{n+1} - \boldsymbol{\Phi}_f^n \\ \\ \boldsymbol{\Phi}_s^{n+1} - \boldsymbol{\Phi}_s^n \end{bmatrix} \frac{1}{\Delta t} = \boldsymbol{\omega}_f\left(\boldsymbol{\Phi}_f^{n+1}, \boldsymbol{\Phi}_s^n\right) + \boldsymbol{\omega}_s\left(\boldsymbol{\Phi}_f^n, \boldsymbol{\Phi}_s^n\right), \tag{2.52}$$

with the superscript n and $n+1$ denoting the n-th and $(n+1)$-th time step, respectively. Based on Eq. (2.52), the contributions from the fast reactions, $\boldsymbol{\omega}_f$, and from the slow reactions, $\boldsymbol{\omega}_s$, are evaluated partially implicitly and fully explicitly, respectively. The fast variables that satisfy Eq. (2.50) are solved implicitly using the first set of equations of Eq. (2.52) with a dimension of n_f; the slow variables can then be solved explicitly using the remaining set of equations of Eq. (2.52) with a dimension of n_s.

In addition, conventional stiff ODE solvers use time-consuming dense matrix techniques, *i.e.*, LU decomposition and back substitution operating algorithm in OpenFOAM standard libraries [58]. Physically, however, each species reacts with only a small portion of species out of the total species in large-scale chemical mechanisms. The chemical Jacobian of their ODE systems *i.e.*, Eq. (2.46), can be extremely sparse. It is still totally dense if the vector of dependent variables, $\mathbf{\Phi}$, consists of only the species mass fractions, Y_i, and temperature, T, *i.e.*, $\mathbf{\Phi} = (Y_i, T)^{\mathrm{T}}$, as all the dependent variables are coupled by the ideal gas equation of state, *i.e.*, Eq. (2.5). In the AHI-S chemistry solver, the sparse matrix technique proposed in Ref. [59] is applicable to AHI, which introduces more dependent variables. Consequently, the inherent sparsity in large mechanisms' Jacobian is capitalised on to further reduce the computational overhead.

To exemplify the sparse matrix technique, the ODE system of a constant-pressure auto-ignition problem is chosen for its simplicity, yet it shares common properties with those of more complex chemically reactive flows. Equation (2.3) and Eq. (2.4) are given by

$$\frac{dY_i}{dt} = \frac{\dot{\omega}_i}{\rho}, (i = 1, 2, \cdots, N-1), \tag{2.53}$$

$$\frac{dT}{dt} = -\frac{1}{\rho c_p} \sum_i h_i \dot{\omega}_i, \tag{2.54}$$

where h_i is the specific enthalpy for the i-th species. A sparser chemical Jacobian can be obtained when the density, ρ, is included in the vector of dependent variables,

i.e., $\mathbf{\Phi} = (Y_i, T, \rho)^{\mathrm{T}}$, through replacing Eq. (2.5) with the following additional ODE,

$$\frac{d\rho}{dt} = \frac{1}{c_p T}\sum_i h_i \dot{\omega}_i - \left(\sum_i \frac{Y_i}{W_i}\right)^{-1} \sum_i \frac{\dot{\omega}_i}{W_i}. \tag{2.55}$$

With the above formulations, as reported in Ref. [59], the chemical Jacobian of large chemical mechanisms was found to become significantly sparse, *e.g.*, 90% sparsity for an n-Heptane mechanism [60]. Whereas, the Jacobian of fairly large mechanisms is still rather dense, *e.g.*, only 11% and 36% sparsity for the GRI-Mech and an acetylene mechanism [61], respectively. It is because any species involved in a pressure-dependent third-body reaction triggers a dense row in the Jacobian. To produce a much sparser Jacobian, similarly, the total mole concentration, C, can be introduced in calculating the third-body concentration. Equation (2.5) is also replaced by

$$C = p \big/ (R_u T)\,, \tag{2.56}$$

$$\frac{dC}{dt} = \frac{C}{\rho c_p T}\sum_i h_i \dot{\omega}_i. \tag{2.57}$$

The ODE system for chemistry integration, *i.e.*, Eq. (2.46), now contains Eqs. (2.53), (2.54), (2.55) and (2.57) and its vector of dependent variables reads $\mathbf{\Phi} = (Y_i, T, \rho, C)^{\mathrm{T}}$, by which the Jacobians of the n-Heptane mechanism [60], the acetylene mechanism [61] and the GRI-Mech become 95%, 73% and 51% sparse, respectively [59]. In the AHI-S chemistry solver, ρ and C are grouped into the slow chemistry and solved explicitly on the premise that sufficiently small integration time steps are used. Note that only the fast chemistry is solved implicitly, but still, its Jacobian has been replaced by a much sparser one as a submatrix of the intact

ODE system Jacobian, and the Jacobian evaluation and factorization see higher computational efficiency.

The rate of each fast elementary reaction is observed to be sensitive to concentrations of only one or two fast species, leading to a few large entries in the sparse Jacobian. The unimportant entries for other fast species can be eliminated from the sparse Jacobian. More specifically, a set of fast species for the k-th fast reaction, $\mathbf{\Phi}_f^{\langle k \rangle}$, as a subset of fast species, $\mathbf{\Phi}_f$, is identified, which includes the i-th species if and only if it satisfies Eq. (2.50) for the k-th fast reaction. The rest of fast species, together with the slow species, are included in a set of reaction-specific slow species, $\mathbf{\Phi}_s^{\langle k \rangle}$. The locally and temporally discretized ODE system, Eq. (2.52), is then replaced by

$$\begin{bmatrix} \mathbf{\Phi}_f^{n+1} - \mathbf{\Phi}_f^n \\ \mathbf{\Phi}_s^{n+1} - \mathbf{\Phi}_s^n \end{bmatrix} \frac{1}{\Delta t} = \boldsymbol{\omega}_f\left(\mathbf{\Phi}_f^{\langle k \rangle, n+1}, \mathbf{\Phi}_s^{\langle k \rangle, n}\right) + \boldsymbol{\omega}_s\left(\mathbf{\Phi}_f^n, \mathbf{\Phi}_s^n\right), \tag{2.58}$$

where the dimensions of $\mathbf{\Phi}_f^{\langle k \rangle}$ and $\mathbf{\Phi}_s^{\langle k \rangle}$, symbolised by $n_f^{\langle k \rangle}$ and $n_s^{\langle k \rangle}$, respectively, are also reaction-specific. Based on Eq. (2.58), a specific fast species is not solved implicitly in every fast reaction. Instead, for a fast reaction, only the contribution from reaction-specific fast species is included in the Jacobian evaluation and factorization of fast chemistry, and thus the computational efficiency is further improved.

2.5 Numerical implementation

The above governing equations of gas and liquid phases are solved using the compressible multi-component reactive two-phase gas-droplet flow solver, AHISsprayDetFoam, based on the Eulerian-Lagrangian method. The AHISsprayDetFoam solver is customised from the built-in OpenFOAM density-based non-reactive rhoCentralFoam solver and coupled with the following modules:

(1) Application of the mixture-averaged diffusion model to consider non-unity Lewis, Schmidt, and Prandtl numbers for high-fidelity modelling of multi-component diffusion;

(2) Incorporation of the built-in OpenFOAM Lagrangian solver coupled with optimised drag coefficient and convective heat transfer coefficient sub-models for accurate prediction of droplet dynamics;

(3) Implementation of the AHI-S chemistry solver to accelerate the finite-rate chemistry integration for efficient modelling of combustion.

Figure 2.1 demonstrates how the data are exchanged between the built-in OpenFOAM rhoCentralFoam and Lagrangian solvers and the AHI-S chemistry solver.

The cell-centered Finite Volume Method (FVM) is used to discretize the gaseous equations, Eqs. (2.1)-(2.5). The OF-splitting scheme is used to separately solve the chemical terms and the non-chemical terms in species mass fraction and energy equations, *i.e.*, Eq. (2.3) and Eq. (2.4). In the first step, the chemical terms in

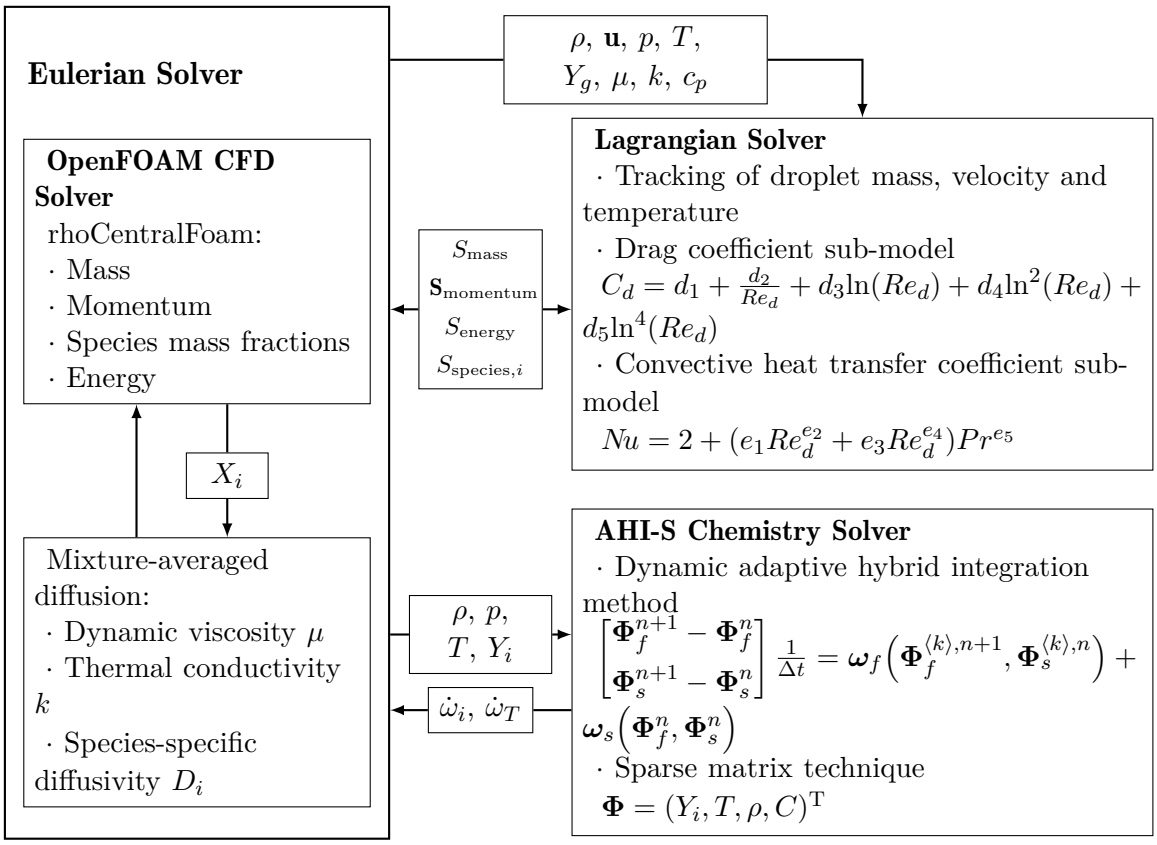


Figure 2.1: Flowchart of the AHISsprayDetFoam solver showing data exchange between the built-in OpenFOAM rhoCentralFoam solver, the built-in OpenFOAM Lagrangian solver, and the AHI-S chemistry solver.

Eq. (2.3) and Eq. (2.4) are solved using the AHI-S chemistry solver. The fast chemistry and the slow chemistry are integrated with the first-order Euler implicit and explicit schemes, respectively. In the second step, the non-chemical terms are integrated over the time step along with the chemical terms calculated from the first step. The second-order implicit Crank-Nicolson scheme [62] is used for the time discretization for the gas phase transport equations. The Courant-Friedrich-

Lewy (CFL) number of the gas phase is set, and the physical time step, Δt, is adjusted accordingly.

Inherited from rhoCentralFoam, AHISsprayDetFoam adopts an operator-splitting approach in the solution of momentum and energy transport terms in Eq. (2.2) and Eq. (2.4). In this manner, an explicit predictor equation is solved for the convection of conserved variables followed by that an implicit corrector equation is solved for the diffusion of primitive variables. The second-order semi-discrete, non-staggered, and central-upwind KNP scheme [5] with a van Leer flux limiter [63] is used for the convection terms in mass, momentum and energy equations, *i.e.*, Eqs. (2.1)-(2.2) and Eq. (2.4). The KNP scheme enables the formation of flux interpolations considering its transport in any direction due to the compressible flow and wave propagation and is inherently simple without involving a Riemann solver. It has been proved to be competitive with the other methods, *e.g.*, piecewise parabolic method and Roe solver with van Leer limiting, in reliably simulating compressible flows and performing shock capturing [3]. The convection term in the species mass fraction equation, *i.e.*, Eq. (2.3), is solved with the second-order accurate Total Variation Diminishing (TVD) scheme "Gauss limitedLinear 1" to ensure the scalar boundness. The TVD scheme preserves the species mass fractions within the physical bounds (0 to 1). The diffusion terms in Eqs. (2.2)-(2.4) are split into an orthogonal component and a non-orthogonal component to minimize the non-orthogonality error. The solution of the orthogonal part adopts the second-order Gauss scheme with linear interpolation; for the non-orthogonal part, the surface interpolation of variable

normal gradients is applied.

The droplets are computed with hybrid Lagrangian particle tracking [64] and stochastic parcel [65] method using the Lagrangian solver. In this manner, they are grouped into parcels within which all droplets share identical properties. Each parcel is then treated as a Lagrangian point and is tracked individually. Note that parcels containing more than one droplet are not addressed in this context. The governing equations of droplets, *i.e.*, Eqs. (2.18)-(2.20), are integrated with the first-order Euler implicit method. The gas phase quantities at the droplet surface, *e.g.*, T in Eq. (2.30), are linearly interpolated from the gas phase results solved from Eqs. (2.1)-(2.5). The gas and liquid phases are two-way coupled, such that the liquid phase solutions necessitate some gas phase quantities, *e.g.*, temperature, density, velocity, and pressure, at the droplet location and also provide the inter-phase exchange rates of mass, momentum, species, and energy for the gas phase solutions. The inter-phase exchange rates of the two-way coupling in the governing equations of both gas and liquid phases are updated at each time step.

The above-mentioned numerical methods and droplet sub-models, *e.g.*, the droplet evaporation model in calculating $\dot{m}_d$ in Eqs. (2.14)-(2.16) and Eq. (2.18), inherited from the built-in OpenFOAM rhoCentralFoam and Lagrangian solvers in AHISsprayDetFoam have been extensively validated. The rhoCentralFoam solver has been validated with non-reactive benchmark cases [3], including 1-D shock tube, 2-D forward-facing step, supersonic jet and hypersonic flow over a biconic. Some analogous numerical solvers coupling rhoCentralFoam with implicit chemistry solvers and/or the Lagrangian solver from OpenFOAM standard

libraries, *e.g.*, rhoCentralRfFoam [6] and RYrhoCentralFoam [9], are increasingly used in the combustion research community. They have shown capabilities in accurately capturing flow discontinuities from shock and expansion waves, shock-flame interactions, and autoignition in supersonic shock-laden reactive flows. The rhoCentralRfFoam solver functions well on computing 1-D planar hydrogen-air detonation [6], 2-D methane-air and hydrogen-oxygen-argon detonation [7, 8] propagation processes. The Eulerian-Lagrangian RYrhoCentralFoam solver further shows accuracy in numerically capturing individual droplet evaporation and two-way gas-droplet coupling in a series of benchmark cases against experimental data and/or analytical solutions [9]. Its capabilities in simulations of rotating detonations [10, 66–68], detonative combustion in two-phase gas-droplet flows [69–72], and supersonic combustors [11, 12, 73–75] have also been confirmed. Accordingly, the AHISsprayDetFoam solver is expected to function well on computing overall characteristics and transient behaviours of droplet-free/laden high-speed chemically reactive flows.

2.6 Summary

The numerical method and implementation of the modules applied for the AHISsprayDetFoam solver development are detailed. The AHISsprayDetFoam solver is a compressible multi-component reactive two-phase gas-droplet flow solver based on the Eulerian-Lagrangian method. It is customised from the built-in OpenFOAM density-based non-reactive rhoCentralFoam solver. The following

modules are integrated into the solver towards its accuracy and efficiency. First, the mixture-averaged diffusion model is applied for high-fidelity modelling of species viscosity, mass, and thermal diffusivities in multi-component mixtures. Second, the built-in OpenFOAM Lagrangian solver is incorporated, and the drag coefficient and convective heat transfer coefficient sub-models are optimised for computationally accurate prediction of liquid droplet dynamics. Last, the AHI-S chemistry solver is implemented to alleviate the large computational cost related to the large size and severe stiffness of detailed chemistry.

Chapter 3

Numerical Solver Validation

3.1 Overview

This chapter explores the numerical accuracy and computational efficiency of the AHISsprayDetFoam solver developed in Chapter 2. The research background is provided in Section 3.2. The optimised droplet sub-models are verified in the modelling of ammonia droplet acceleration and cooling in the flowing and/or low-temperature air in Section 3.3. The 1-D ammonia droplet-laden/free ammonia-oxygen detonation problem is introduced in Section 3.4. It is simulated to examine the performance of the mixture-averaged diffusion model in calculating multi-component diffusion in Section 3.5 and the performance of the AHI-S solver in reducing computational cost in Section 3.6. 2-D application of this physical problem is addressed in Chapter 4 with a more detailed research background referred to. The summary of this chapter is provided in Section 3.7.

3.2 Background

Ammonia droplet acceleration and cooling in surrounding air, as well as 1-D detonation propagation in ammonia droplet-free/laden ammonia-oxygen mixtures, are simulated for the following reasons. Zero-carbon ammonia is expected to play a significant role in future renewable energy networks. Detonative combustion in ammonia blends characterises higher pressure and temperature than deflagration [76–78]; thus lower nitrogen oxides emissions are expected [79], indicating the potential of using ammonia in detonation-based engines. Direct injection and subsequent burning of ammonia spray have been proposed to mitigate equipment and operating costs, and the start-up time of ammonia-fueled engines. Detonation propagation in ammonia blends with/without perturbations from dilute ammonia droplets, therefore, draw research interests. 2-D and 3-D applications of the configuration will be addressed in Chapter 4 and future works, respectively, on the premise that 1-D simulations shown here validate the capability of AHISsprayDetFoam in predicting this physical problem.

3.3 Optimised droplet sub-model implementation

Optimised drag coefficient and convective heat transfer coefficient sub-models related to the droplet phase are validated in correct implementation in this section. Firstly, the performances of the drag coefficient sub-models are investigated through reproducing the velocity evolution of an initially static ammonia droplet

in flowing air. Using the AHISsprayDetFoam solver, the drag-induced momentum transfer between the gas and droplet phases is simulated in a 500-m-long duct. The velocity of the air is 1,000 m/s initially. It is little affected by the single droplet and thus remains constant. The diameter of the ammonia droplet is 200 μm. The temperature of both the droplet and the air is 295 K. The pressure of the air is 2 MPa. The droplet evaporation and breakup, and the inter-phase heat transfer are not considered here by turning off the corresponding sub-models. Based on Eq. (2.34), the temporal evolution of droplet velocity results in droplet Reynolds numbers, Re_d, ranging from 0.1 to 100,000. Figure 3.1 shows the dependences of the drag coefficient, C_d, on Re_d, where numerical results are presented against Brown and Lawler's correlation developed from experimental data throughout the twentieth century [53]. Numerical simulations using the built-in OpenFOAM drag coefficient sub-model [52] and the optimised sub-model with a functional form of C_d trained by experimental data, *i.e.*, Eq. (10) in Ref. [27], are performed. Equation (10) from Ref. [27] has been given in Eq. (2.36). To verify correct implementations of the sub-models in AHISsprayDetFoam, C_d is inversely calculated from simulation results of the inter-phase momentum exchange rate, $\mathbf{S}_{\text{momentum}}$, via the drag force, $\mathbf{F}_d$, by Eq. (2.15) and Eq. (2.35). Note that in Eq. (2.15), F_p is assumed to be zero here with its sub-model turned off, and thus $\mathbf{S}_{\text{momentum}}$ is only related to $\mathbf{F}_d$ on the premise of no droplet evaporation.

In Figure 3.1, the variations of C_d with respect to Re_d predicted by the two drag coefficient sub-models agree well with Brown and Lawler's correlation when the ammonia droplet is at low and moderate Reynolds numbers. For values of Re_d

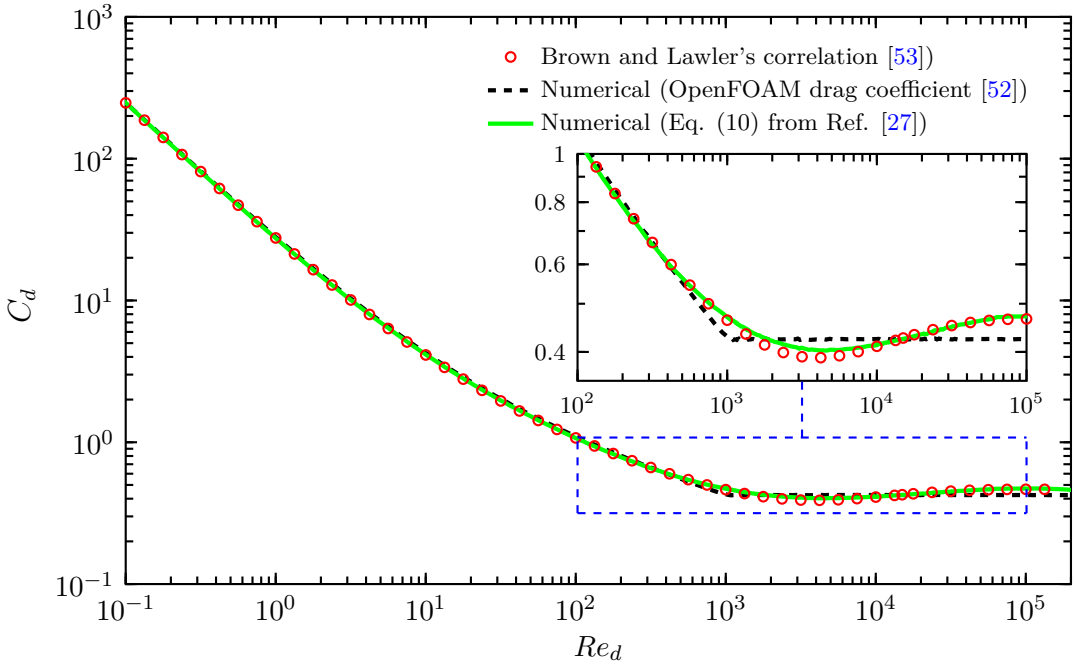


Figure 3.1: Numerical results of drag coefficient with respect to droplet Reynolds number predicted with optimised and built-in OpenFOAM drag coefficient sub-models against experimental data from Ref. [53]. The optimised sub-model is based on Eq. (10) from Ref. [27].

over 500, the optimised sub-model based on Eq. (10) from Ref. [27] continues to accurately capture the variations of C_d; the prediction using the built-in OpenFOAM drag coefficient sub-model starts to deviate from the rests. C_d predicted by the built-in OpenFOAM drag coefficient sub-model keeps constant at 0.424 when $Re_d > 1,000$, which does not perfectly follow Brown and Lawler's correlation. The prediction of C_d using the sub-model based on Eq. (10) from Ref. [27], whereas, is still valid for the droplet at high Reynolds numbers against Brown and Lawler's correlation, and is therefore selected in the following numerical

studies, as stated above, *i.e.*, Eq. (2.36).

The selected drag coefficient sub-model is further verified through comparing numerical and analytical solutions about the drag-induced acceleration of an ammonia droplet in a low-velocity air stream. With an assumption of constant momentum response time, τ_{momentum}, the analytical solution of droplet velocity can be obtained by integrating the droplet velocity equation, *i.e.*, Eq. (2.19), reads

$$\mathbf{u}_d(t) = \mathbf{u} - [\mathbf{u} - \mathbf{u}_d(t_0)]\exp\left(\frac{-t}{\tau_{\text{momentum}}}\right), \tag{3.1}$$

where t_0 is the initial time, and τ_{momentum} is calculated by [20]

$$\tau_{\text{momentum}} = \frac{\rho_d d^2}{18\mu}. \tag{3.2}$$

The assumption of constant τ_{momentum} is only valid with no droplet evaporation and Re_d far below 1. Based on this, the velocity of the air stream is set as 1 m/s, and the ammonia droplet is initially static. The temperature of both the air and the ammonia droplet is 295 K. Three numerical simulations are performed in a 1-m-long duct when the droplet diameter is 200, 300, and 400 μm, corresponding to τ_{momentum} of 0.074, 0.167, and 0.296 s, respectively. Figure 3.2 shows the temporal evolutions of droplet velocity at different τ_{momentum}. Excellent agreement is observed between the numerical results solved using AHISsprayDetFoam coupled with the optimised drag coefficient sub-model based on Eq. (10) from Ref. [27] and the analytical solutions computed by Eq. (3.1).

To examine the performances of the convective heat transfer coefficient sub-models, the temperature evolution of an ammonia droplet arising from heat

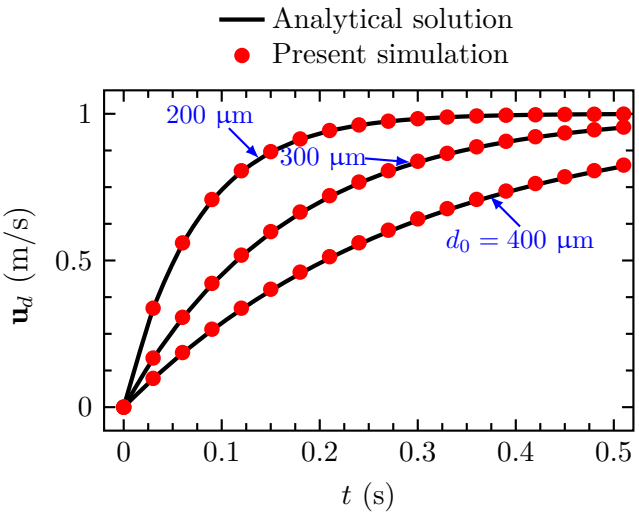


Figure 3.2: Time histories of droplet velocity under different initial droplet diameters.

transfer with a surrounding air stream under forced convection is reproduced. The 500-m-long duct is used to perform parametric simulations using the AHISsprayDetFoam solver. The temperature and velocity of the air are constant at 245 K and 1,000 m/s, respectively. Those of the ammonia droplet are 295 K and 0 m/s initially, and the droplet diameter is 200 μm. The pressure of the air is 2 MPa. The droplet is still assumed to be non-evaporating and non-breaking up by turning off the corresponding sub-models. Figure 3.3 shows the variation of the Nusselt number, Nu, with respect to Re_d. Numerical results predicted by convective heat transfer coefficient sub-models with functional forms of Nu including built-in OpenFOAM Ranz and Marshall correlation [51] and Whitaker correlation [28] are presented. The Whitaker correlation [28] has been given in Eq. (2.40). Nu is inversely calculated from simulation results of the inter-phase energy

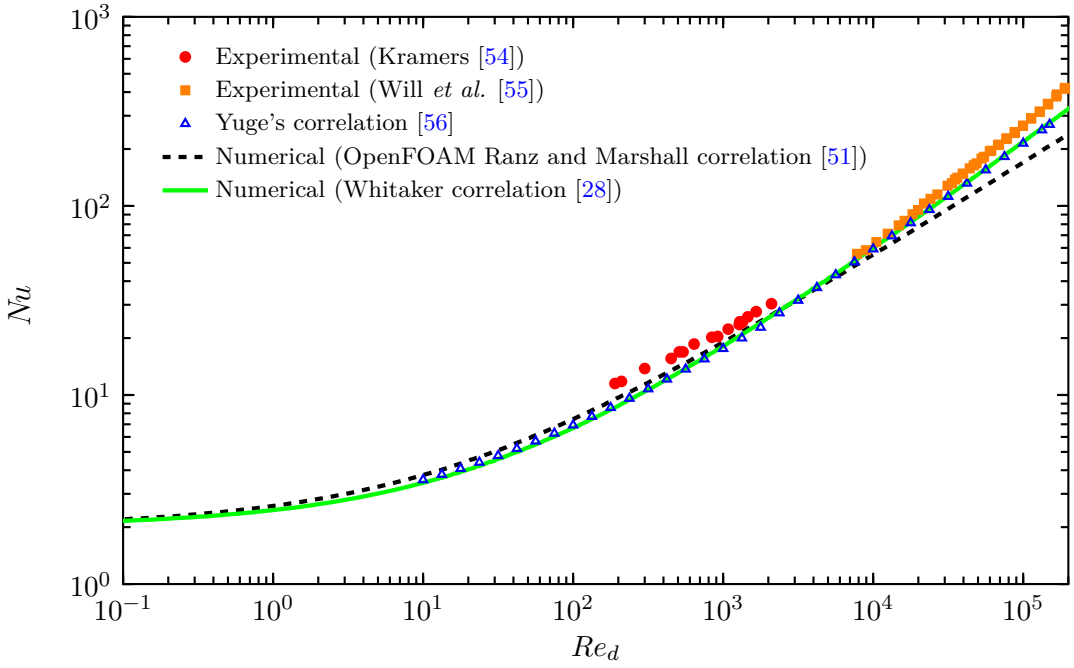


Figure 3.3: Numerical results of Nusselt number with respect to droplet Reynolds number predicted with optimised and built-in OpenFOAM convective heat transfer coefficient sub-models against experimental data from Refs. [54–56]. The optimised sub-model is based on Whitaker correlation [28].

exchange rate, S_{energy}, via the convective heat transfer rate and coefficient, $\dot{Q}_c$ and h_c, by Eq. (2.16), Eq. (2.38), and Eq. (2.39). Note that in Eq. (2.16), $(-\dot{m}_d h_v)$ is zero here on the premise of no droplet evaporation, and thus S_{energy} is only related to $\dot{Q}_c$. In addition to Re_d, Nu is also dependent on the Prandtl number, Pr, which remains unchanged at 0.69 in the simulations. Accordingly, experimental data collected by Kramers [54] ($Pr = 0.714$) and Will *et al.* [55] ($Pr \approx 0.7$), as well as Yuge's correlation [56] ($Pr = 0.715$) developed from his experiments, are presented as references.

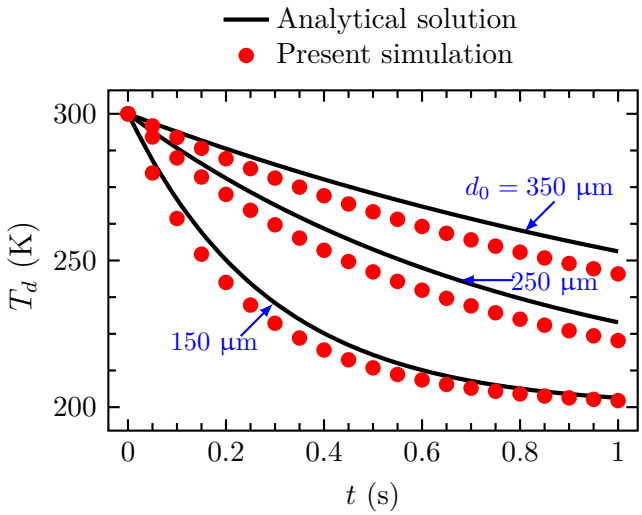


Figure 3.4: Time histories of droplet temperature under different initial droplet diameters.

In Figure 3.3, the dependences of Nu on Re_d predicted by the two convective heat transfer coefficient sub-models perfectly keep in step when the ammonia droplet is at low Reynolds numbers. For the values of Re_d between 10 and 10,000, Nu predicted by the two sub-models also closely follow the experimental data from Kramers [54] and Yuge's correlation [56]. Starting at $Re_d = 10,000$, the prediction of Nu using the built-in OpenFOAM Ranz and Marshall correlation [51] starts to deviate from that using the optimised sub-model based on the Whitaker correlation [28]. The sub-model based on the Whitaker correlation [28] show good accuracy against Yuge's correlation [56] and the experimental data from Will *et al.* [55] in capturing the variations of Nu until $Re_d = 100,000$. It is thus verified in correct implementation in AHISsprayDetFoam and will be utilised in the following studies, as stated above, *i.e.*, Eq. (2.40).

The selected convective heat transfer coefficient sub-model is further verified through simulating the heat transfer between a quiescent ammonia droplet and air against analytical solutions. Assuming a constant thermal response time, τ_{thermo}, the droplet temperature can be analytically solved by integrating the droplet temperature equation, *i.e.*, Eq. (2.20), reads

$$T_d(t) = T - [T - T_d(t_0)]\exp\left(\frac{-t}{\tau_{\text{thermo}}}\right), \tag{3.3}$$

where τ_{thermo} is calculated by [20]

$$\tau_{\text{thermo}} = \frac{c_{pd}\rho_d d^2}{6Nuk}. \tag{3.4}$$

The assumption that τ_{thermo} remains constant is likewise valid when the droplet is non-evaporating and $Re_d \ll 1$. Based on this, the velocity of both the air and the ammonia droplet is 0 m/s; the gaseous temperature is 200 K, and the droplet temperature is 300 K initially. Three initial values of the droplet diameter, *i.e.*, 150, 250, and 350 μm, are used in the numerical simulations. Figure 3.4 shows the temporal evolutions of droplet temperature in the three cases. Note that the temperature evolution of the droplet triggers varying c_{pd}, ρ_d, and thus varying d under the assumption of no evaporation. Therefore, τ_{thermo} calculated from Eq. (3.4) cannot remain unchanged. Its initial values, *i.e.*, 0.29, 0.806, and 1.58 s, corresponding to droplet diameters of 150, 250, and 350 μm, respectively, at $t = 0$, are used in generating the analytical solutions in Figure 3.4. The unstrict assumption of constant τ_{thermo} results in slight differences between the numerical

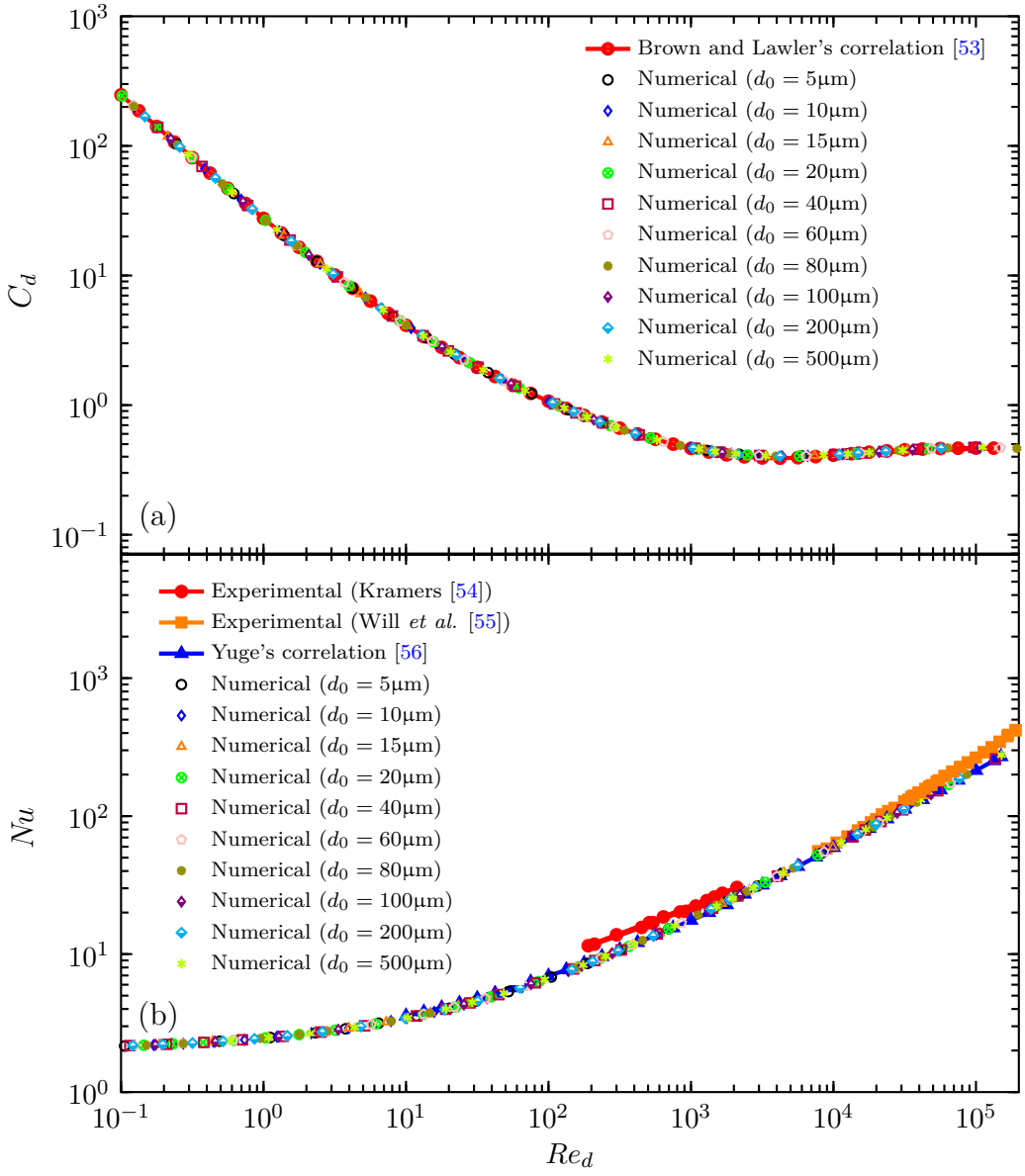


Figure 3.5: Numerical results of (a) drag coefficient and (b) Nusselt number with respect to droplet Reynolds number predicted with the optimised drag coefficient sub-model based on Eq. (10) from Ref. [27] and convective heat transfer coefficient sub-model based on Whitaker correlation [28] under different initial droplet diameters against experimental data from Ref. [53] and Refs. [54–56], respectively.

and analytical solutions as time increases, as Figure 3.4 shows. However, generally, the comparisons further verify the correct implementation of the optimised convective heat transfer coefficient sub-model based on the Whitaker correlation [28] into AHISsprayDetFoam.

The optimised drag coefficient sub-model based on Eq. (10) from Ref. [27] and convective heat transfer coefficient sub-model based on the Whitaker correlation [28] are likewise verified for ammonia droplets with a series of diameters, *i.e.*, 5-500 μm. Figures 3.5(a) and (b) show the dependences of C_d and Nu on Re_d in comparison with experimental data from Ref. [53] and Refs. [54–56], respectively. It is seen that the predictions using the optimised droplet sub-models are valid for droplets at all these sizes with Re_d ranging from 0.1 to 100,000.

3.4 1-D ammonia-oxygen detonation study

The performances of the mixture-averaged diffusion model and the AHI-S chemistry solver are examined with detonation propagation in ammonia-oxygen (NH_3-O_2) mixtures with/without perturbations from dispersed evaporating ammonia droplets. Targeted at examining the accuracy and efficiency of AHISsprayDetFoam rather than portraying the morphologies of either the Detonation Wave (DW) or the ammonia droplets, a 1-D computational domain is considered in this work, shown in Figure 3.6. The 1-D simplification allows the adoption of fine mesh and detailed chemistry with affordable computational cost, and has been widely used in the modelling of shock-laden flows with spatially

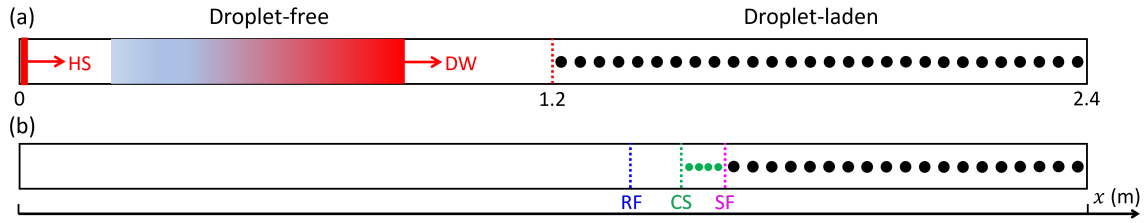


Figure 3.6: Schematics of 1-D detonation propagation in NH_3-O_2 mixtures (a) before and (b) after the detonation enters the two-phase section. Circles: ammonia droplets; HS: hot spot; DW: detonation wave; SF: shock front; RF: reaction front; CS: contact surface.

uniform droplets [48, 70, 80, 81].

The 1-D geometry is 2.4 m in length which starts at $x = 0$. It is open to the surroundings at both the left and the right ends where the zero-gradient boundary condition is applied. Note that all computational domains are treated as 3-D in OpenFOAM. For the 1-D geometry, the reduced y- and z-directions are discretized with one cell, and the "empty" boundary condition is applied. For two-phase simulations, the lengths along these directions, *i.e.*, 0.5 mm along both y- and z-directions here, affect some quantities of the droplet phase, *e.g.*, droplet number density, N_d, and volume fraction, V_{fd}, and further affect the gas phase.

Figures 3.6(a) and (b) show instantaneous scenarios before and after the detonation propagates into the two-phase section, respectively. Both the carrier gas, *i.e.*, NH_3-O_2 mixtures, and the ammonia droplets are quiescent at $t = 0$. In the gas phase, the initial temperature, T_0, is 295 K; the fuel-oxidizer equivalence ratio, ϕ, ranges from 0.55 to 1.55, and the initial pressure, p_0, ranges from 35 to 105 kPa. Demonstrated in Figure 3.6(a), a 2-mm Hot Spot (HS) with high

pressure ($50p_0$) and high temperature (2,000 K) is set at the left end to initiate the right-propagating DW in the NH_3-O_2 mixtures. Note that a DW is a complex of preceding Shock Front (SF) and auto-igniting Reaction Front (RF) with an in-between induction zone. Both lower and higher HS pressures, *i.e.*, $40p_0$-$100p_0$, are also tested beforehand. Within the gaseous compositions of NH_3-O_2 mixtures considered in this work, detonations are not successfully initiated by lower HS pressures, while highly overdriven detonations are initiated by higher HS pressures.

The droplet-laden section starts from $x = 1.2$ m to the right end, where, initially, mono-sized ammonia droplets with a diameter, d_0, of 5 μm are uniformly distributed. The performances of the aforementioned selected droplet sub-models for the ammonia droplet at this size have been validated, see Figure 3.5. The initial temperature, $T_{d,0}$, density, $\rho_{d,0}$, and heat capacity, $c_{pd,0}$, of the ammonia droplets are 232.9 K, 689.9 kg/m^3 and 4,406.6 J/(kg·K), respectively. The initial droplet number density of $N_{d,0} = 1 \times 10^{12}$ /m^3 is considered, corresponding to the initial droplet volume fraction of $V_{fd,0} = 6.54 \times 10^{-5}$. Figure 3.6(b) presents one of the two configurations of three characteristic fronts, *i.e.*, the transmitted SF, the RF, and the two-phase Contact Surface (CS), which are numerically observed after the detonation enters the two-phase section. The CS is the interface between the droplet-free and droplet-laden sections. The other configuration where the RF is located between the SF and CS is involved in Section 3.5 later.

The accuracy of AHISsprayDetFoam in predicting the detonation propagation speed within the droplet-free section is firstly verified in comparison with experimental work by Weng *et al.* [82] and analytical solutions, *i.e.*,

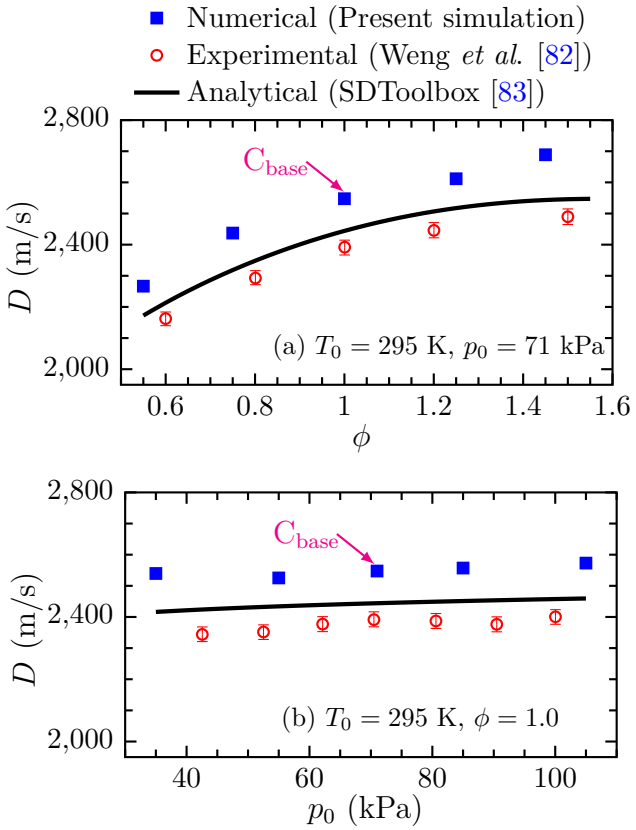


Figure 3.7: Numerical, experimental, and analytical results of detonation velocity as functions of (a) equivalence ratio, ϕ, and (b) initial pressure, p_0, in NH_3-O_2 mixtures. C_{base}: the baseline case with $T_0 = 295$ K, $\phi = 1.0$, $p_0 = 71$ kPa.

Chapman–Jouguet (CJ) detonation velocity, D_{CJ}, calculated by Shock & Detonation Toolbox (abbreviated as "SDToolbox" hereafter) [83]. Figures 3.7(a) and (b) show the detonation velocity, D, in the NH_3-O_2 mixtures as functions of ϕ and p_0, respectively. A detailed chemical mechanism for ammonia combustion including 32 species and 203 reactions [84] is applied for the numerical and analytical results. The Half Reaction Length (HRL) of the

Zel'dovich-Neumann-Döring (ZND) structure predicted by SDToolbox [83] is 830.4 μm for the baseline case with T_0 = 295 K, ϕ = 1.0, p_0 = 71 kPa, *i.e.*, C_{base} in Figure 3.7. Based on this, uniform meshes of Δx = 10 μm are used to discretize the 1-D geometry in the present simulations, corresponding to about 83 cells in the HRL. The CFL number of 0.05 approximately corresponds to Δt of 2×10^{-10} s. The safety factor, β, is 0.5. The effects of β on the performances of AHISsprayDetFoam are discussed later in Section 3.6.

Note that pulsating instabilities in detonation propagation with periodic variations of the RF and SF are numerically observed. As they have been extensively reported [85–88], the corresponding physics will not be detailed in this work. The numerical results of D in Figure 3.7 are the averaged detonation velocity covering the droplet-free section, calculated based on the movement of RF (or SF) over the corresponding time interval, *e.g.*, 0-0.47 ms for the baseline case. The locations of RF and SF are identified where the Heat Release Rate (HRR) and the pressure gradient, ∇p, peak, respectively. Other criteria, *e.g.*, the mass fraction of ammonia (Y_{NH_3}), are also tested but exhibit minor effects on the location identification. It is seen that the evolutionary tendencies of D with respect to both ϕ and p_0 predicted in the numerical studies are in line with the experimental and analytical data. Within the test ranges, D is more sensitive to ϕ rather than p_0 by all the means. The values of D are slightly overestimated in the present simulations, by about 7% and 4.5% compared to the experimental data collected by Weng *et al.* [82] and the analytical data solved by SDToolbox [83], respectively. Note that the numerical results of D exceed the corresponding CJ detonation

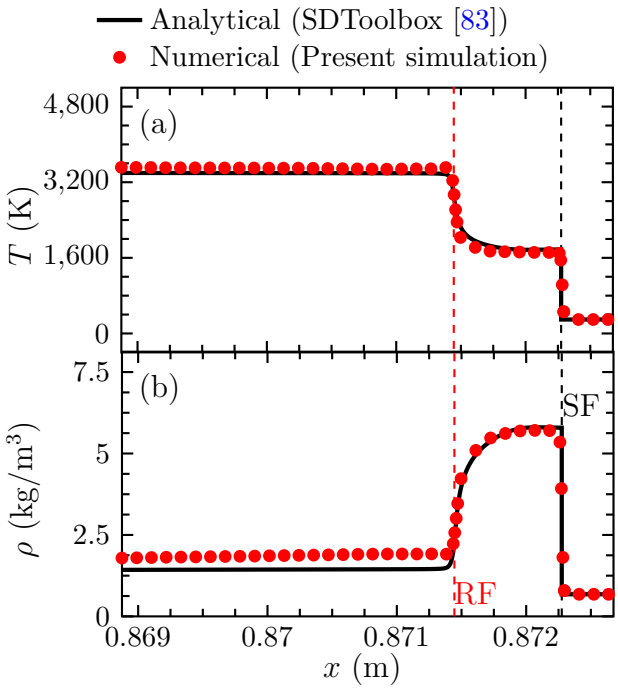


Figure 3.8: Spatial distributions of (a) temperature and (b) density at 339 μs against the ZND structure predicted by SDToolbox [83] in the NH_3-O_2 mixture when $p_0 = 71$ kPa, $\phi = 1.0$, $T_0 = 295$ K. SF: the location of shock front; RF: the location of reaction front.

velocities as slightly overdriven detonations are initiated using the ignition method in the present simulations. In general, however, the numerical results show satisfactory accuracy, which validates the capability of AHISsprayDetFoam in the calculation of detonation propagation speed within the droplet-free section.

The physico-chemical structure within the induction zone between the SF and RF and nearby is quantified through demonstrating the spatial evolutions of temperature, T, and density, ρ, in Figure 3.8. Those of some species mass fractions, *i.e.*, Y_{NH_3}, Y_{O_2}, Y_{N_2}, Y_{H_2O}, Y_{NH} and Y_{OH}, are presented in Figure 3.9.

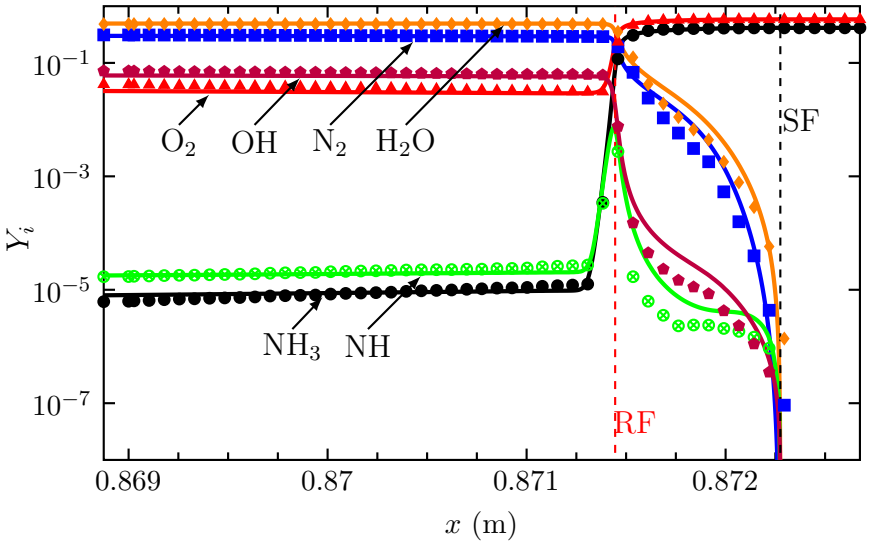


Figure 3.9: Spatial distributions of species mass fractions at 339 μs against the ZND structure predicted by SDToolbox [83] in the NH_3-O_2 mixture when $p_0 = 71$ kPa, $\phi = 1.0$, $T_0 = 295$ K. SF: the location of shock front; RF: the location of reaction front. Dotted curves show results from the present simulation; curves show results from SDToolbox [83].

The numerical results of the baseline case at 339 μs are selected, when the induction zone is as long as the HRL of the corresponding ZND structure predicted by SDToolbox [83], *i.e.*, 830.4 μm. To make comparisons and further verify the accuracy of AHISsprayDetFoam, the profiles of T, ρ, and Y_i in the ZND structure are projected onto the 1-D geometry, also shown in Figures 3.8 and 3.9. Note that the locations of RF and SF in the ZND structure are matched with their counterparts calculated numerically for the projection.

In Figures 3.8(a) and (b), the variations of both T and ρ between the SF and RF are captured well in the present simulation against the analytical solutions. Their critical values and inflection points in the computations developed with

AHISsprayDetFoam and SDToolbox [83] are in good agreement. In the post-detonation zone behind the RF, the two profiles of T continue to closely overlap; however, ρ calculated numerically is observed to be relatively high. The higher post-detonation value of ρ arises from that of p in the present simulation. It is a typical characteristic of the overdriven detonation compared to the corresponding CJ detonation [89]. Accordingly, the values of Y_i in the detonated mixture predicted by the two means are approximately at the same level, plotted in Figure 3.9. In the induction zone, AHISsprayDetFoam provides accurate predictions on the spatial evolutions of the reactants, *i.e.*, Y_{NH_3} and Y_{O_2}, compared to SDToolbox [83]; whereas, the numerical and analytical results of the products, *i.e.*, Y_{N_2} and Y_{H_2O}, and intermediates, *i.e.*, Y_{NH} and Y_{OH}, slightly differ from each other. Note that due to the pulsating instabilities in detonation propagation, the spatial distributions of physico-chemical structure in the present simulation display periodic variations. The unsteady detonation structure features the above-mentioned deviations from the steady ZND structure. Therefore, the accuracy of AHISsprayDetFoam in the depiction of detonation structure within the droplet-free section is generally confirmed.

In addition, the relevance of the aforementioned optimised droplet sub-models to the 1-D numerical simulations of detonation propagation in ammonia droplet-laden ammonia-oxygen mixtures is examined via a *posteriori* analysis of droplet Reynolds number. The spatial distribution of the droplet Reynolds number within the induction zone between the SF and RF and nearby at 517 μs for the baseline case after the detonation enters the two-phase section is presented in Figure 3.10.

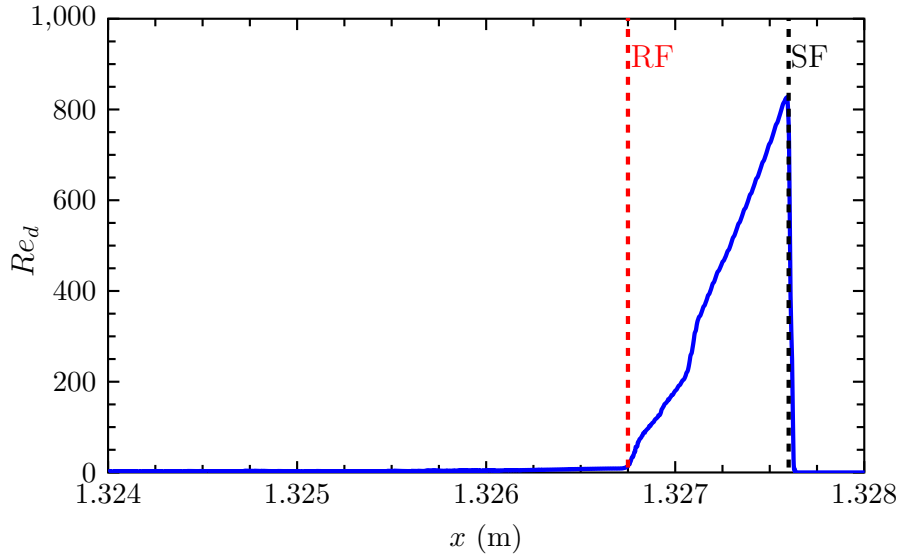


Figure 3.10: Spatial distribution of droplet Reynolds number at 517 μs in the NH_3-O_2 mixture when $p_0 = 71$ kPa, $\phi = 1.0$, $T_0 = 295$ K with perturbations from ammonia droplets when $N_{d,0} = 1 \times 10^{12}/\text{m}^3$. SF: the location of shock front; RF: the location of reaction front.

The critical time of 517 μs is selected when the induction zone is as long as the HRL of the corresponding ZND structure. It is seen from Figure 3.10 that Re_d peaks at around 825 slightly behind the SF where the inter-phase velocity difference is the highest. As C_d and Nu predicted by the built-in OpenFOAM sub-models start to deviate from those of the optimised sub-models and the corresponding experimental data with values of Re_d over 500 and 10,000, respectively, see Figures 3.1 and 3.3. The optimised drag coefficient sub-model is necessitated in the present simulation, while the optimised convective heat transfer coefficient sub-model is not a must but still valid. Note that the initial diameter, *i.e.*, d_0, of ammonia droplets considered in this work is 5 μm. Larger ammonia droplets are expected to see higher values of

Re_d which is proportional to the droplet diameter, see Equation (2.34).

3.5 Diffusion model analysis

The improvement concerning multi-component diffusion modelling is assessed by comparing numerical results solved using the AHISsprayDetFoam solver, coupled with the mixture-averaged diffusion model and the built-in OpenFOAM diffusion model, respectively. Figure 3.11 depicts the spatial and temporal distributions of temperature and pressure gradient for the baseline case before the detonation enters the two-phase section. Predicted by either diffusion model, the RF and SF experience alternate coupling and decoupling subject to the varying in-between induction zone length, *i.e.*, pulsating propagation of the overdriven detonations. The dynamic behaviours and complex interactions of the RF and SF are not further elaborated here, given that some studies have done so [87, 88]. Differently, whereas, non-monotonic evolutions of the RF and SF are captured in the present simulations using both diffusion models. The criteria for a pulsating detonation cycle set out in the literature [87, 88] are not applicable. Two bifurcation points, *i.e.*, B_1 and B_1^* marked in the pressure gradient distributions in both Figures 3.11(a) and (b), are identified as tipping points from the maxima to the minima of the induction zone length. Note that a new SF (indicated by distinctly high localised $|\nabla p|$) forms just ahead of the RF at these instants. The ensuing occurrence of a new developing Detonative Front (DF) shortens the induction zone abruptly, accompanied by the formation of a series of Compression

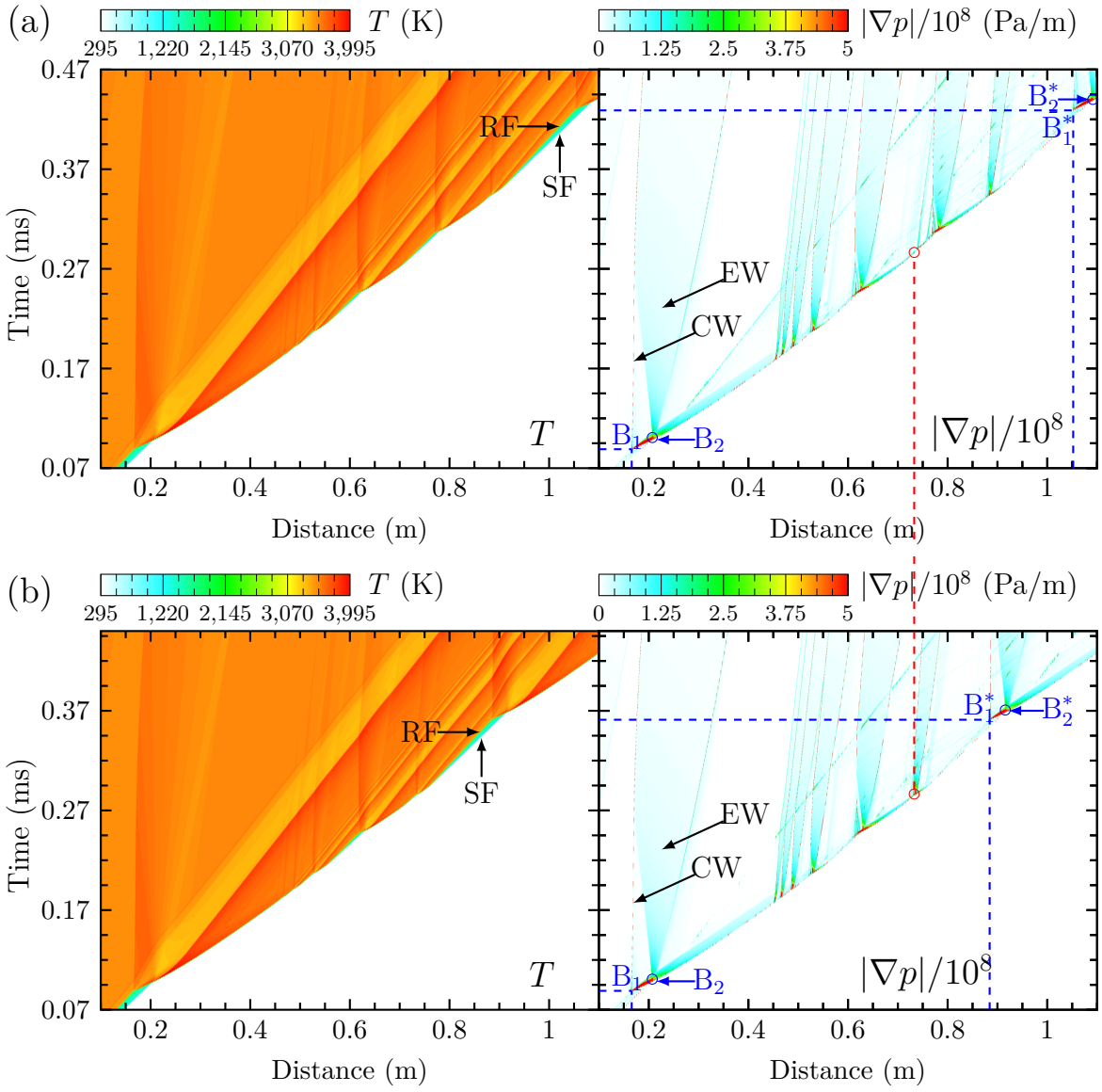


Figure 3.11: Comparisons of the spatial and temporal distributions of temperature (in K, first column) and pressure gradient (in Pa/m, second column) predicted with (a) mixture-averaged diffusion model and (b) built-in OpenFOAM diffusion model in the NH_3-O_2 mixture when $p_0 = 71$ kPa, $\phi = 1.0$, $T_0 = 295$ K. SF: shock front; RF: reaction front; CW: compression wave; EW: expansion wave; B_1, B_2, B_1^* and B_2^*: bifurcation points.

Waves (CW) behind the RF. B_1 and B_1^* are the first bifurcation points suggesting that a RF-SF recoupling starts. The new DF later overtakes the preceding SF at the second bifurcation points, *e.g.*, B_2 and B_2^*, along with the generation of an Expansion Wave (EW) [87, 88]. The periods between B_1 and B_1^* are regarded as the corresponding pulsating detonation cycles. Using either diffusion model, multiple secondary decoupling and recoupling of the RF and SF, as well as complexes of the CW and EW between B_1 and B_1^*, are also numerically observed. They are regarded as sub-processes within each pulsating cycle.

In both Figures 3.11(a) and (b), B_1 occurs at 0.089 ms. The predictions using the two diffusion models agree relatively well in the early stages after B_1, but evidently deviate after 0.284 ms. At the divergence instant, a secondary RF-SF decoupling proceeds using the mixture-averaged diffusion model; however, a secondary RF-SF recoupling starts to emerge using the built-in OpenFOAM diffusion model. Consequently, B_1^* occurs at 0.429 ms in Figure 3.11(a), but moves up to 0.361 ms in Figure 3.11(b). Numerical results within a lengthened droplet-free section show that the foregoing phenomena roughly repeat after both B_1^* within the next pulsating cycles though not demonstrated in Figure 3.11. These results indicate that the choice of diffusion model significantly influences the numerical prediction of the pulsating instabilities in detonation propagation within the droplet-free section.

The temporal evolutions of RF velocity around 0.284 ms predicted by the two diffusion models are presented in Figure 3.12(a). Critical instants are identified, when the thermal diffusion term in the energy equation, *i.e.*, $[\nabla \cdot (k\nabla T)]$ in Eq.

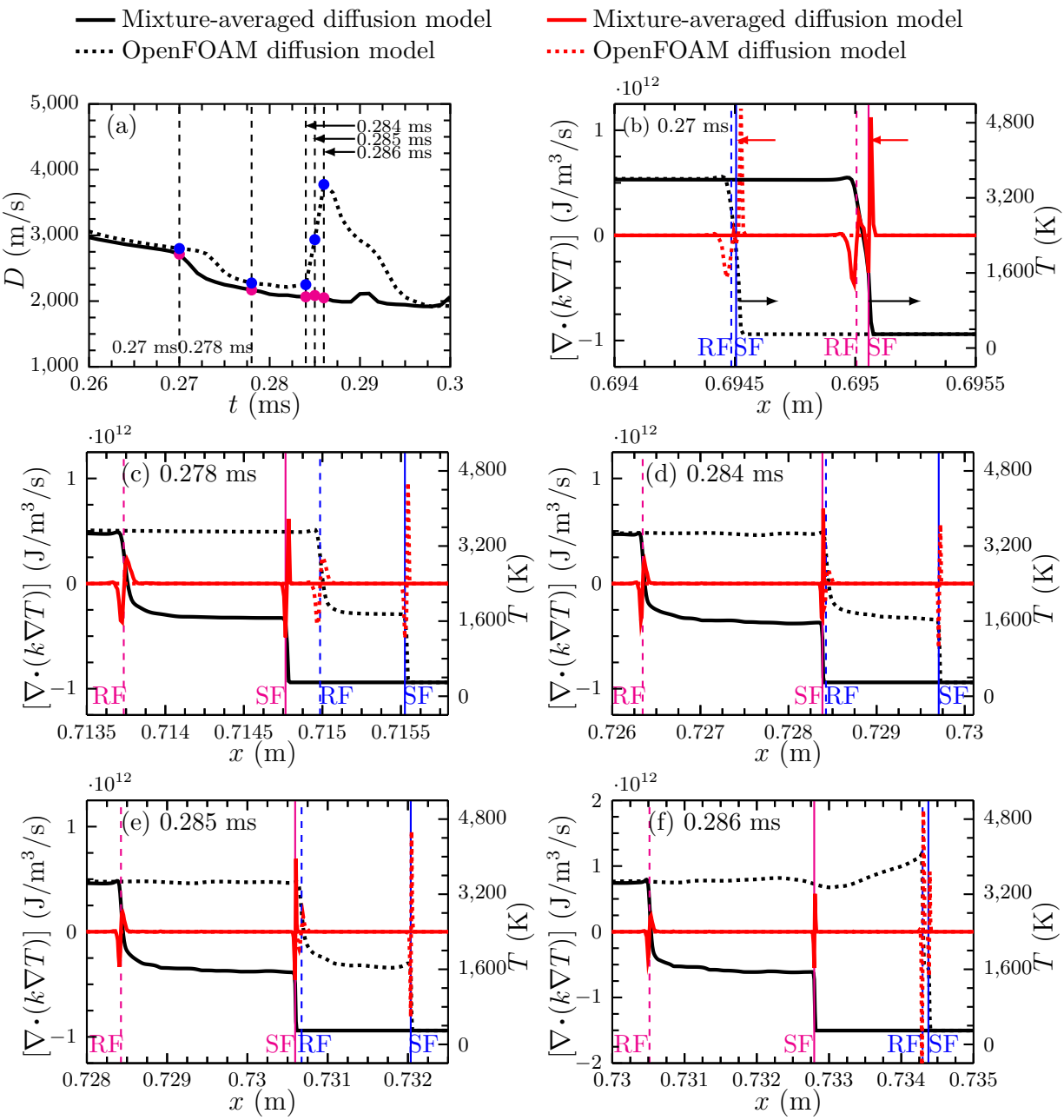


Figure 3.12: (a) Time histories of reaction front propagation speeds and comparisons of the spatial distributions of temperature and thermal diffusion term in energy equation predicted with mixture-averaged diffusion model and built-in OpenFOAM diffusion model at (b) 0.27 ms, (c) 0.278 ms, (d) 0.284 ms, (e) 0.285 ms and (f) 0.286 ms in the NH_3-O_2 mixture when $p_0 = 71$ kPa, $\phi = 1.0$, $T_0 = 295$ K. SF: the location of shock front; RF: the location of reaction front.

(2.4), is analysed to quantitatively describe the role that diffusion models play. The spatial evolutions of $[\nabla\cdot(k\nabla T)]$, as well as those of T, at these instants are presented in Figures 3.12(b)-(f). At 0.27 ms, it is seen from Figure 3.11 that, simulated using either diffusion model, the RF and SF are coupled but towards a secondary decoupling. The two profiles of T and the corresponding narrow induction zones in Figure 3.12(b) support this. The thermal diffusion acts as sink terms around the RF with the negative parts of $[\nabla\cdot(k\nabla T)]$ dominating the positive parts, but to the contrary around the SF. Compared to the mixture-averaged diffusion model, the built-in OpenFOAM diffusion model underestimates the absolute value of $[\nabla\cdot(k\nabla T)]$ around the RF but overestimates that around the SF. This phenomenon continues at 0.278 ms, and thus the secondary RF-SF decoupling predicted by the mixture-averaged diffusion model is faster (indicated by the relatively longer induction zone in Figure 3.12(c)). At 0.284 and 0.285 ms shown in Figures 3.12(d) and (e), the differences between the two predictions become more distinguishable. The mixture-averaged diffusion model retains its prediction of the thermal diffusion around the RF and SF, by which the secondary RF-SF decoupling proceeds. Meanwhile, using the built-in OpenFOAM diffusion model, the values of $[\nabla\cdot(k\nabla T)]$ around the RF dramatically decline; while its positive and negative parts around the SF almost counterbalance each other. Accordingly, a secondary RF-SF recoupling occurs as Figure 3.11(b) depicts. The secondary RF-SF recoupling completes at 0.286 ms with considerably increased thermal diffusion around the RF inducing a subsequent secondary RF-SF decoupling. Instead, the variations of $[\nabla\cdot(k\nabla T)]$ around both the RF and SF predicted by the mixture-averaged diffusion model advance. After these

instants, the two diffusion models predict different modes of pulsating detonation propagation in the present simulations.

The numerical results of species diffusion term in the species mass fraction equation, *i.e.*, $[\nabla \cdot (\rho Y_i \mathbf{V}_i)]$ in Eq. (2.3), are likewise analysed and compared between the two diffusion models. The spatial evolutions of $[\nabla \cdot (\rho Y_i \mathbf{V}_i)]$ for some species around the RF at 0.27 and 0.284 ms are presented in Figures 3.13(a) and (b), respectively. Predicted by either diffusion model, the negative parts of $[\nabla \cdot (\rho Y_i \mathbf{V}_i)]$ dominate for the reactants, *i.e.*, NH_3 and O_2, but are subordinate to the positive parts for the products, *i.e.*, N_2 and H_2O, contributing to the decreased and increased concentrations of the reactants and products, respectively. For the intermediates, *i.e.*, NH, OH, H_2 and H, the almost zero-sum species diffusion is numerically observed. The built-in OpenFOAM diffusion model predicts the species diffusion with the unity Lewis number assumption. Consequently, compared to the mixture-averaged diffusion model, it overestimates the values of $[\nabla \cdot (\rho Y_i \mathbf{V}_i)]$ for relatively heavy species, including O_2 and N_2, while underestimates those for relatively light species, including NH_3, H_2O, NH,OH, H_2 and H at both 0.27 and 0.284 ms. The differences between the two predictions of the lightest species, *i.e.*, H_2 and H, are especially significant. Similar to the thermal diffusion, the differences of species diffusion predicted by the two diffusion models are more distinguishable at 0.284 ms. These different predictions co-contribute to the different numerical results demonstrated in Figures 3.11(a) and (b).

Figure 3.14 compares the spatial evolutions of the lightest species' mass

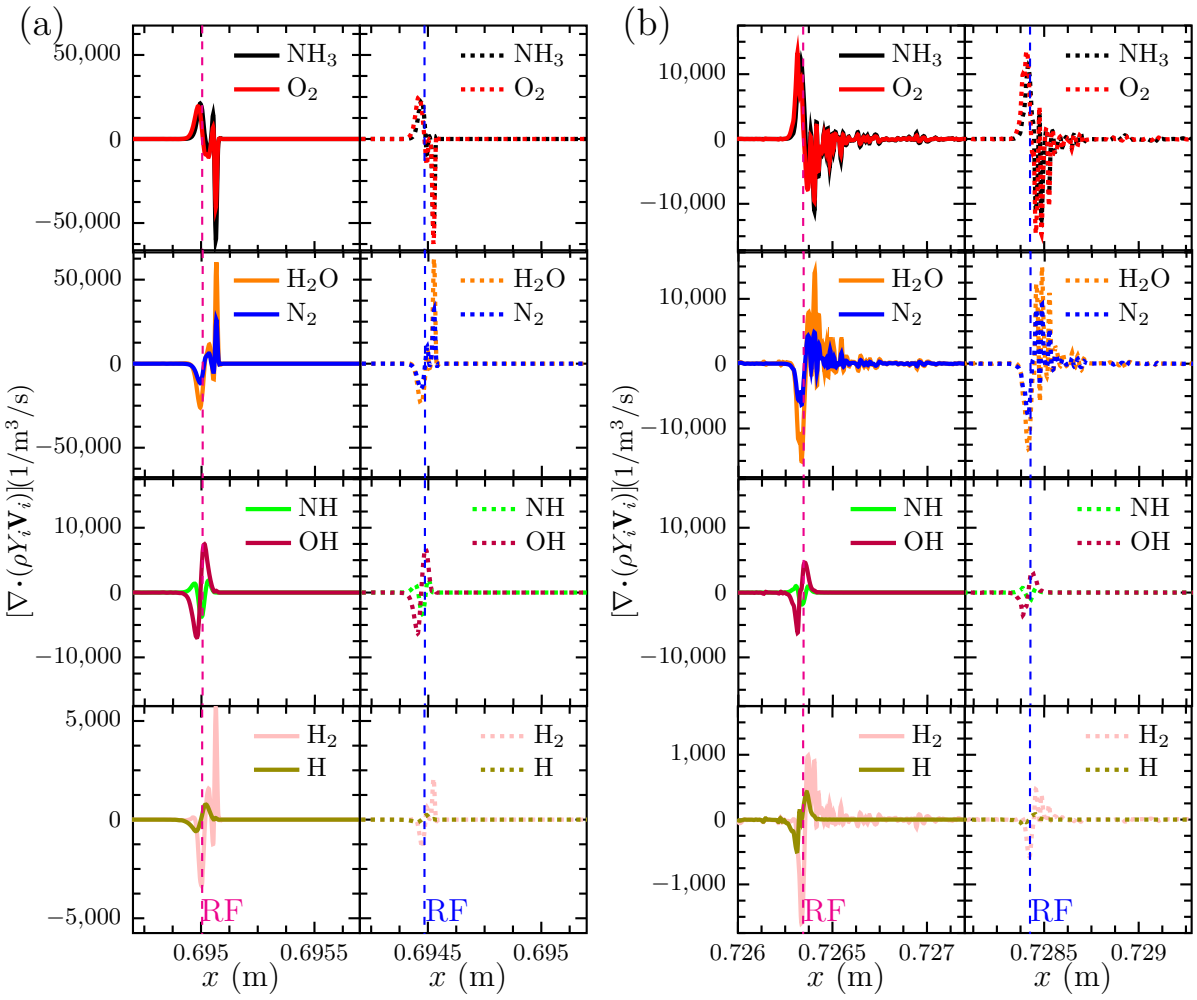


Figure 3.13: Comparisons of the spatial distributions of species diffusion term in species mass fraction equation predicted with mixture-averaged diffusion model and built-in OpenFOAM diffusion model at (a) 0.27 ms and (b) 0.284 ms in the NH_3-O_2 mixture when $p_0 = 71$ kPa, $\phi = 1.0$, $T_0 = 295$ K. RF: the location of reaction front. Curves show results with mixture-averaged diffusion model; dotted curves show results with built-in OpenFOAM diffusion model.

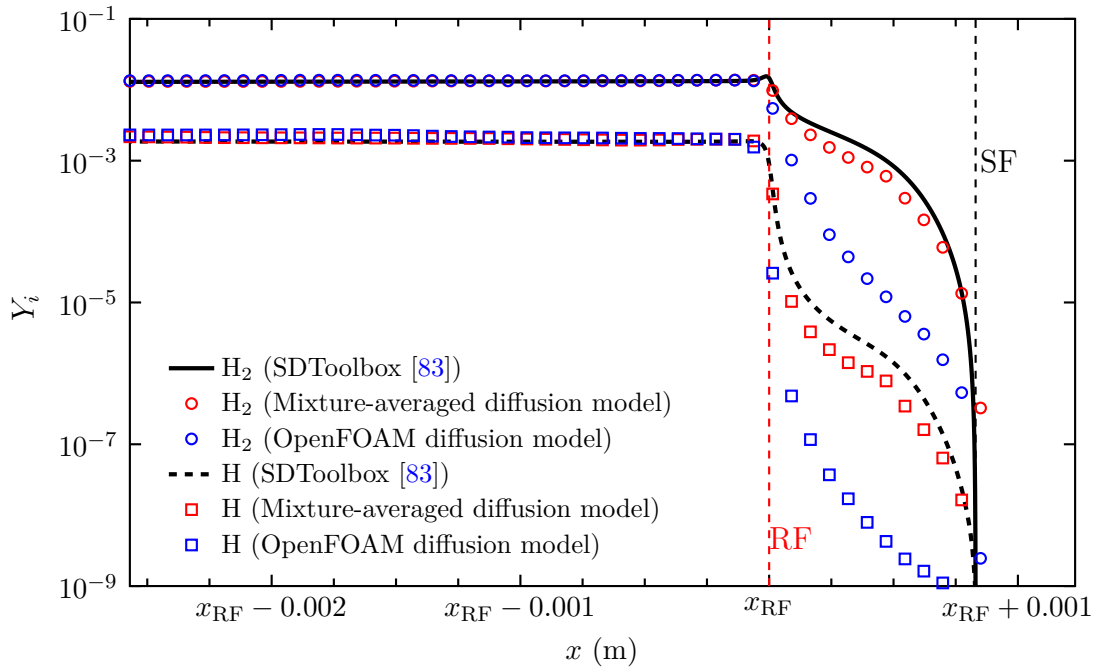


Figure 3.14: Comparisons of the spatial distributions of H_2 and H mass fractions predicted with mixture-averaged diffusion model and built-in OpenFOAM diffusion model against the ZND structure predicted by SDToolbox [83] in the NH_3-O_2 mixture when $p_0 = 71$ kPa, $\phi = 1.0$, $T_0 = 295$ K. SF: the location of shock front; RF: the location of reaction front.

fractions, *i.e.*, Y_{H_2} and Y_H, within the induction zone between the SF and RF and nearby predicted by the two diffusion models against those in the corresponding ZND structure predicted by SDToolbox [83]. The selected numerical results of Y_{H_2} and Y_H using the mixture-averaged diffusion model and the built-in OpenFOAM diffusion model are at 339 and 297 μs, respectively, to equate the induction zone lengths to the HRL of the ZND structure. They are projected onto the 1-D simulated domain along with their counterparts in the ZND structure with matched locations of RF and SF for the projection. It is seen from Figure 3.14

that the present simulations using both diffusion models predict the values of Y_{H_2} and Y_H in the post-detonation zone behind the RF perfectly following SDToolbox [83]. In the induction zone between the SF and RF, Y_{H_2} and Y_H are numerically underestimated compared to those in the ZND structure. The mixture-averaged diffusion model captures more accurate variations of both Y_{H_2} and Y_H between the SF and RF than the built-in OpenFOAM diffusion model. This phenomenon is triggered by the different predictions of H_2 and H mass diffusions, see Figure 3.13. Therefore, the mixture-averaged diffusion model shows better accuracy in depicting the detonation structure within the droplet-free section attributed to improved multi-component diffusion modelling than the built-in OpenFOAM diffusion model.

Figure 3.15 depicts the spatial and temporal distributions of gaseous temperature, pressure gradient, and droplet diameter for the baseline case after the detonation enters the two-phase section. Note that the seed values at $x = 1.2$ m, $t = 0.47$ ms in both Figures 3.15(a) and (b) are numerical results at the right end of the droplet-free section solved using the AHISsprayDetFoam coupled with the mixture-averaged diffusion model. The same initialiser assures that divergent predictions using the two diffusion models within the droplet-laden section are not continuations from those within the droplet-free section. Predicted by either diffusion model, the transients of RF-SF decoupling and recoupling, bifurcation points, *i.e.*, B_1 and B_2, compression and expansion waves, *i.e.*, CW and EW, are observed with as without the perturbations from ammonia droplets shown in Figure 3.11. Differently, whereas, B_1^* and B_2^* suggesting the start and end of

RF-SF recoupling for the next pulsating cycle have not occurred yet in the present simulations, so do secondary decoupling and recoupling of the RF and SF. Still, both diffusion models numerically capture the pulsating instabilities in detonation propagation in the certain ammonia droplet-laden NH_3-O_2 mixture. Similar phenomena of pulsating detonation propagation in hydrogen/oxygen/argon gas with water sprays were reported by Xu and Zhang [70].

The evident deviation between the two predictions starts at 0.636 ms, when a RF-SF recoupling kicks off using the mixture-averaged diffusion model, while the counterpart using the built-in OpenFOAM diffusion model lags 0.028 ms behind. Note that the underpinning mechanism of the RF-SF recoupling within the droplet-laden section predicted by both diffusion models is consistent with that within the droplet-free section. Herewith, at B_1 a newly-formed SF and the closely upstream RF make up a newly-formed DF that merges into the preceding SF at B_2. The corresponding analysis is provided below.

Figures 3.16(a) and (b) show the spatial distributions of pressure, temperature, and HRR at 0.638 and 0.64 ms, respectively. After B_1 in Figure 3.15(a), the localised pressure rise of new SF is observed just ahead of the peak HRR of RF at 0.638 ms. The new DF with coupled RF and new SF, where the values of ρ, T, and HRR pronouncedly and co-locatedly jump, subsequently arises at 0.64 ms. The preceding SF downstream of the CS decays concurrently as the pressure leap across it declines. The new DF reaches and combines with the preceding SF and the RF-SF recoupling completes later at B_2 in Figure 3.15(a).

It is seen from both Figures 3.15(a) and (b) that the zone ahead of the SF is

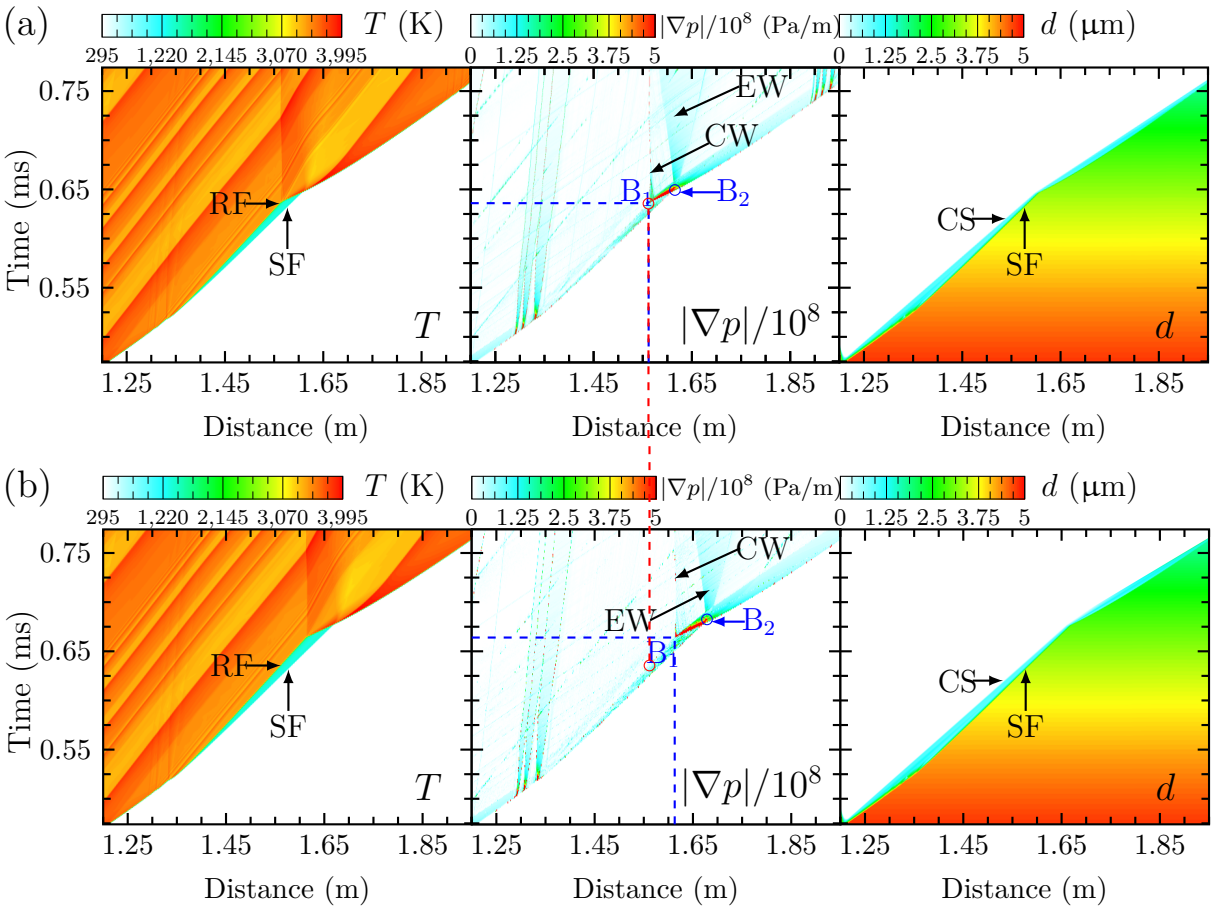


Figure 3.15: Comparisons of the spatial and temporal distributions of gaseous temperature (in K, first column), pressure gradient (in Pa/m, second column) and droplet diameter (in μm, last column) predicted with (a) mixture-averaged diffusion model and (b) built-in OpenFOAM diffusion model in the NH_3-O_2 mixture when $p_0 = 71$ kPa, $\phi = 1.0$, $T_0 = 295$ K with perturbations from ammonia droplets when $N_{d,0} = 1 \times 10^{12}/\mathrm{m}^3$. SF: shock front; RF: reaction front; CW: compression wave; EW: expansion wave; B_1 and B_2: bifurcation points; CS: contact surface.

slightly perturbed for the droplet phase because of slow evaporation in the intact gas. Gas-droplet interactions mainly proceed between the CS and transmitted SF across which d plunges. Simulated using either diffusion model, the distance between

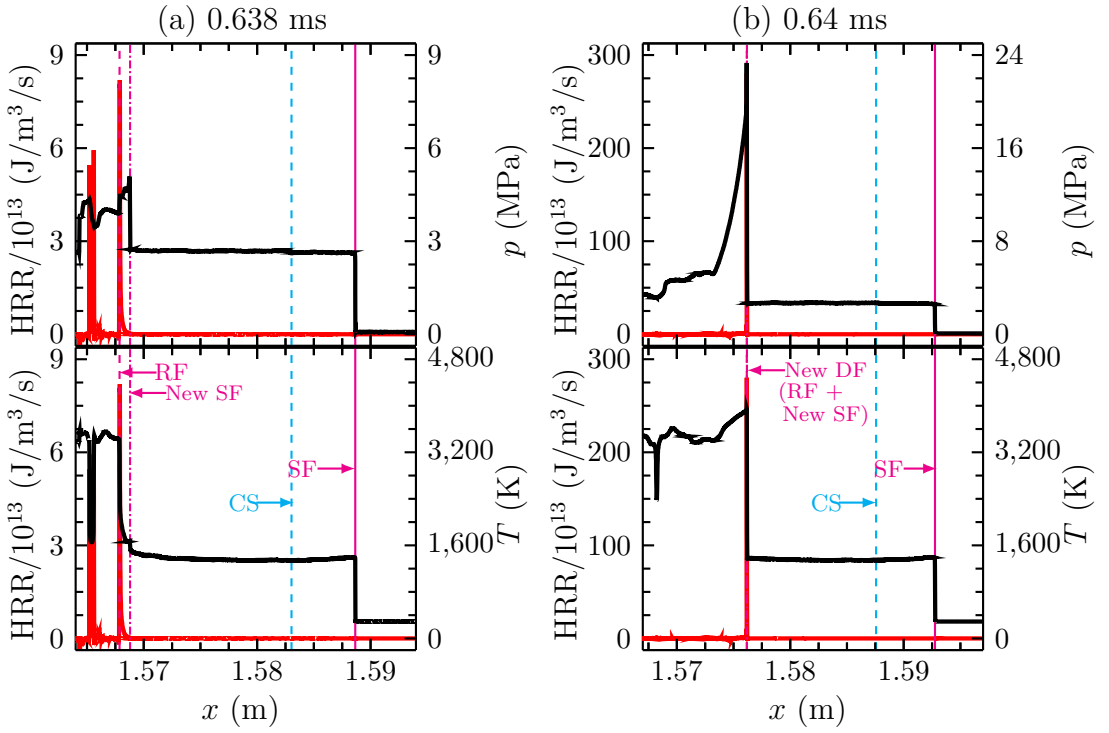


Figure 3.16: Spatial distributions of heat release rate, pressure and temperature at (a) 0.638 ms and (b) 0.64 ms in the NH_3-O_2 mixture when $p_0 = 71$ kPa, $\phi = 1.0$, $T_0 = 295$ K with perturbations from ammonia droplets when $N_{d,0} = 1 \times 10^{12}/\mathrm{m}^3$. SF: the location of shock front; RF: the location of reaction front; DF: the location of detonative front; CS: the location of contact surface.

the CS and SF is predicted to change in response to the coupling and decoupling of the RF and SF. The RF penetrates the droplets when it couples with the SF, corroborated by the wider distance between the CS and SF than the induction zone. Around B_1 when the RF and SF decouple, instead, the induction zone is segmented into the droplet-free/laden parts. The occurrence of this configuration, followed by the RF-SF recoupling, is likewise numerically captured relatively late by the built-in OpenFOAM diffusion model compared to the mixture-averaged diffusion model.

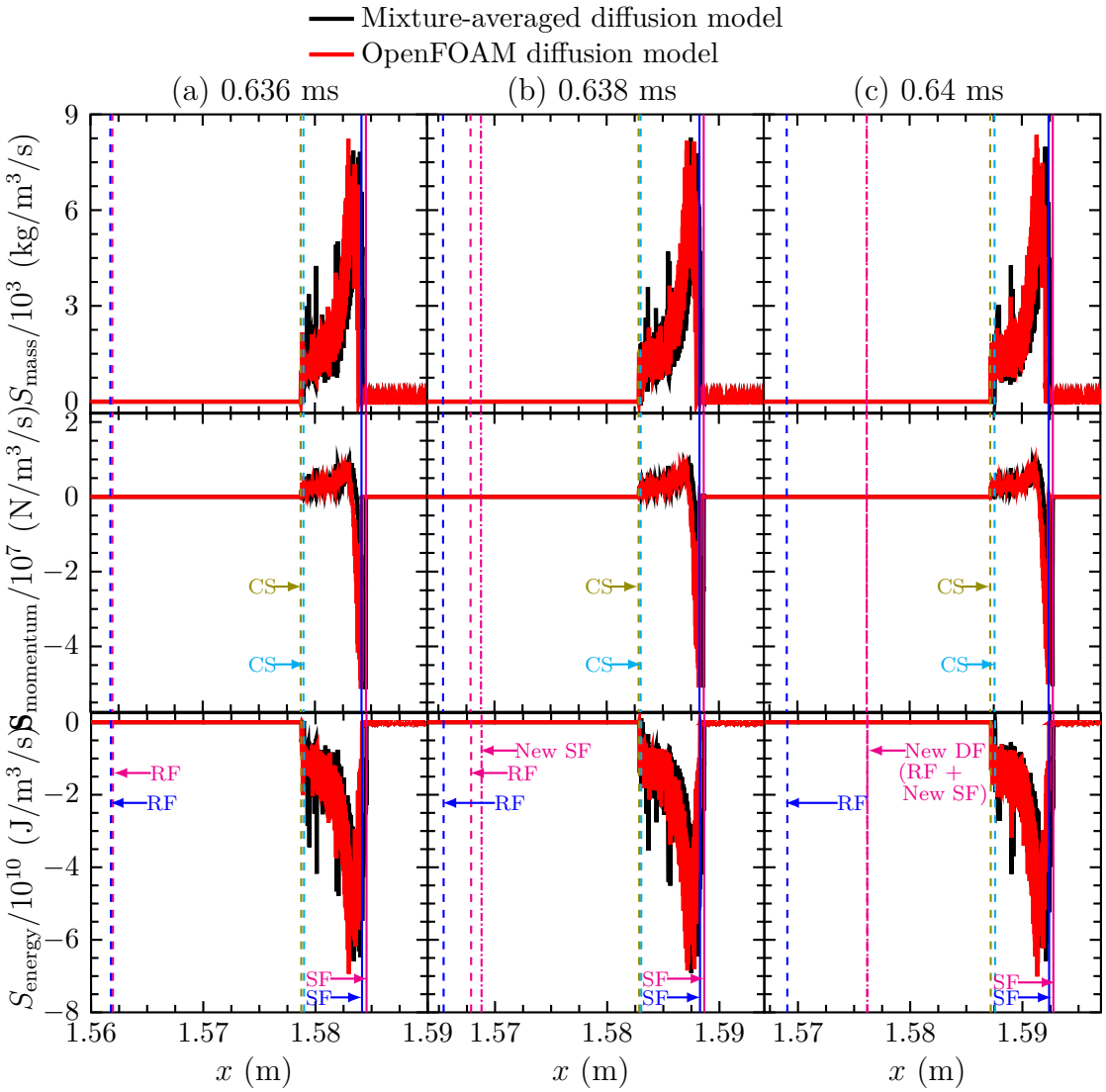


Figure 3.17: Comparisons of the spatial distributions of mass, momentum, and energy exchange rates predicted with mixture-averaged diffusion model and built-in OpenFOAM diffusion model at (a) 0.636 ms, (b) 0.638 ms, (c) 0.64 ms in the NH_3-O_2 mixture when $p_0 = 71$ kPa, $\phi = 1.0$, $T_0 = 295$ K with perturbations from ammonia droplets when $N_{d,0} = 1 \times 10^{12}/\text{m}^3$. SF: the location of shock front; RF: the location of reaction front; DF: the location of detonative front; CS: the location of contact surface.

According to these findings, the choice of diffusion models also affects the numerical prediction of pulsating detonation propagation within the droplet-laden section.

The two diffusion models predict the gaseous thermal and species diffusions divergently within the droplet-laden section in like manner as within the droplet-free section, which is not further elaborated here. Additionally, the differences in the predictions of gas-droplet interactions are quantitatively described by analysing the two-phase exchange terms, *i.e.*, S_{mass}, $\mathbf{S}_{\text{momentum}}$, and S_{energy} in Eqs. (2.1), (2.2), and (2.4). The spatial evolutions of S_{mass}, $\mathbf{S}_{\text{momentum}}$, and S_{energy} at critical instants of 0.636, 0.638, and 0.64 ms are presented in Figures 3.17(a)-(c), respectively. The locations of RF, preceding SF, new SF and DF in the gas phase and CS are labelled for references. The positive values of S_{mass} and negative values of $\mathbf{S}_{\text{momentum}}$ and S_{energy} match with droplet evaporation, acceleration and heating as the detonation propagates within the two-phase section. Using either diffusion model, local fluctuations of all the three two-phase exchange rates, caused by the non-uniformity of droplet number per cell due to droplet motions, are numerically observed. Compared to the mixture-averaged diffusion model, the built-in OpenFOAM diffusion model underestimates these local fluctuations and corresponding droplet motions. This would result in different estimations of wave interactions in the carrier gas behind the preceding SF that trigger pulsating instabilities in detonation propagation based on the square wave model proposed by McVey and Toong [90]. The different predictions of gas-droplet interactions, plus those of gaseous thermal and species diffusion, co-contribute to the different numerical results using the two diffusion models

demonstrated in Figures 3.15(a) and (b). In general, the accuracy gain of AHISsprayDetFoam with the application of the mixture-averaged diffusion model is confirmed in predicting the detonation propagation within the droplet-free section. It is ambiguous within the droplet-laden section due to lack of experimental and analytical data for reference.

3.6 Computational cost reduction

The improvement concerning computational efficiency is assessed by comparing computational costs using the AHISsprayDetFoam solver, coupled with the AHI-S chemistry solver and the built-in OpenFOAM EulerImplicit solver, respectively. Figure 3.18 shows the execution time per simulation step for the baseline case before and after the detonation enters the two-phase section. Using the built-in OpenFOAM EulerImplicit solver, the simulations covering 100 steps cost 35.1 and 38.1 s per step on average within the droplet-free and droplet-laden sections, respectively. The corresponding averaged values using the AHI-S chemistry solver are 18.4 and 21.8 s with a safety factor, β, of 0.5. These results indicate that the AHI-S chemistry solver is significantly less time-consuming (45-50% faster) than the built-in OpenFOAM EulerImplicit solver. Larger chemical mechanisms are expected to see more pronounced reductions in computational cost [35, 41].

The dependence of averaged execution time per simulation step on β using the AHI-S chemistry solver is presented in Figure 3.19. Specifically, with increased

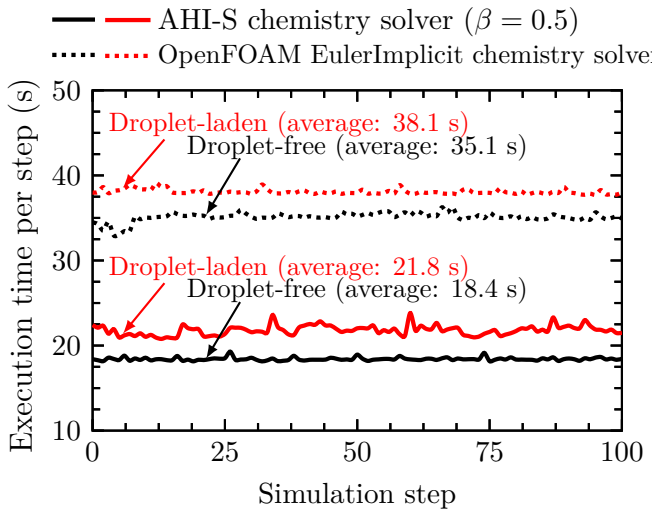


Figure 3.18: Comparisons of execution time per simulation step using AHI-S chemistry solver and built-in OpenFOAM EulerImplicit chemistry solver.

β from 0.0001 to 0.5, the computational cost decreases from 23.99 to 18.41 s and from 27.25 to 21.80 s per step within the droplet-free and droplet-laden sections, respectively. This finding is anticipated as larger values of β group smaller portions of finite-rate chemistry into the fast subset to be solved implicitly, thereby resulting in higher computational efficiency.

The dependences of the numbers of fast species and reactions, *i.e.*, n_f and M_f, in the fast chemistry subset on β are also examined. Figures 3.20 and 3.21 show the spatial distributions of n_f and M_f within the induction zones between the SF and RF and nearby under different values of β at 339 and 517 μs, respectively, before and after the detonation enters the two-phase section. Note that for Figures 3.20 and 3.21, the simulations were performed in AHISsprayDetFoam for just one time step using the solution obtained from $\beta = 0.5$. In this manner, some other influential

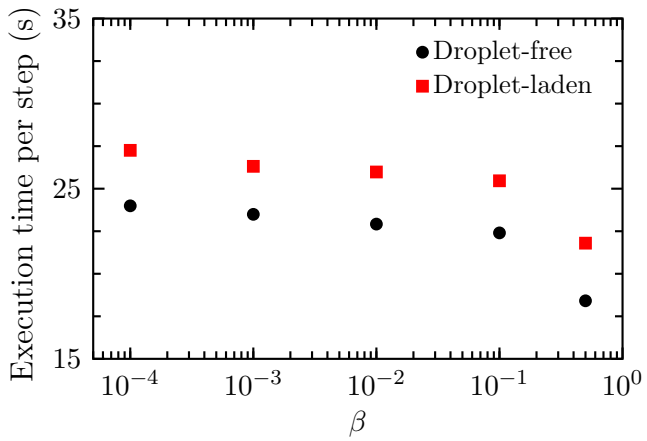


Figure 3.19: Dependence of averaged execution time per simulation step on the safety factor.

factors, *e.g.*, instantaneous gaseous and droplet thermo-chemical states, in addition to β on n_f and M_f, maintain unchanged, and the lengths of the induction zones equal the HRL of the corresponding ZND structure.

The profiles of n_f and M_f with the same β in Figures 3.20(a)/(b) and 3.21(a)/(b) are quite alike in critical values and inflection points. They are thus only slightly affected by the addition of the ammonia droplets in the carrier gas under the specific operating conditions. Overall, n_f and M_f throughout the simulated domain decrease with the increase of β from 0.0001 to 0.5. At $\beta = 0.0001$, n_f and M_f are 30 and 153, respectively, slightly behind the RF within both droplet-free and droplet-laden sections. n_f and M_f decreases to 5/6 and 9/10, respectively, within the droplet-free/laden sections when $\beta = 0.5$. The differences in both n_f and M_f under different values of β explain the variations of the averaged execution time per simulation step with respect to β demonstrated in

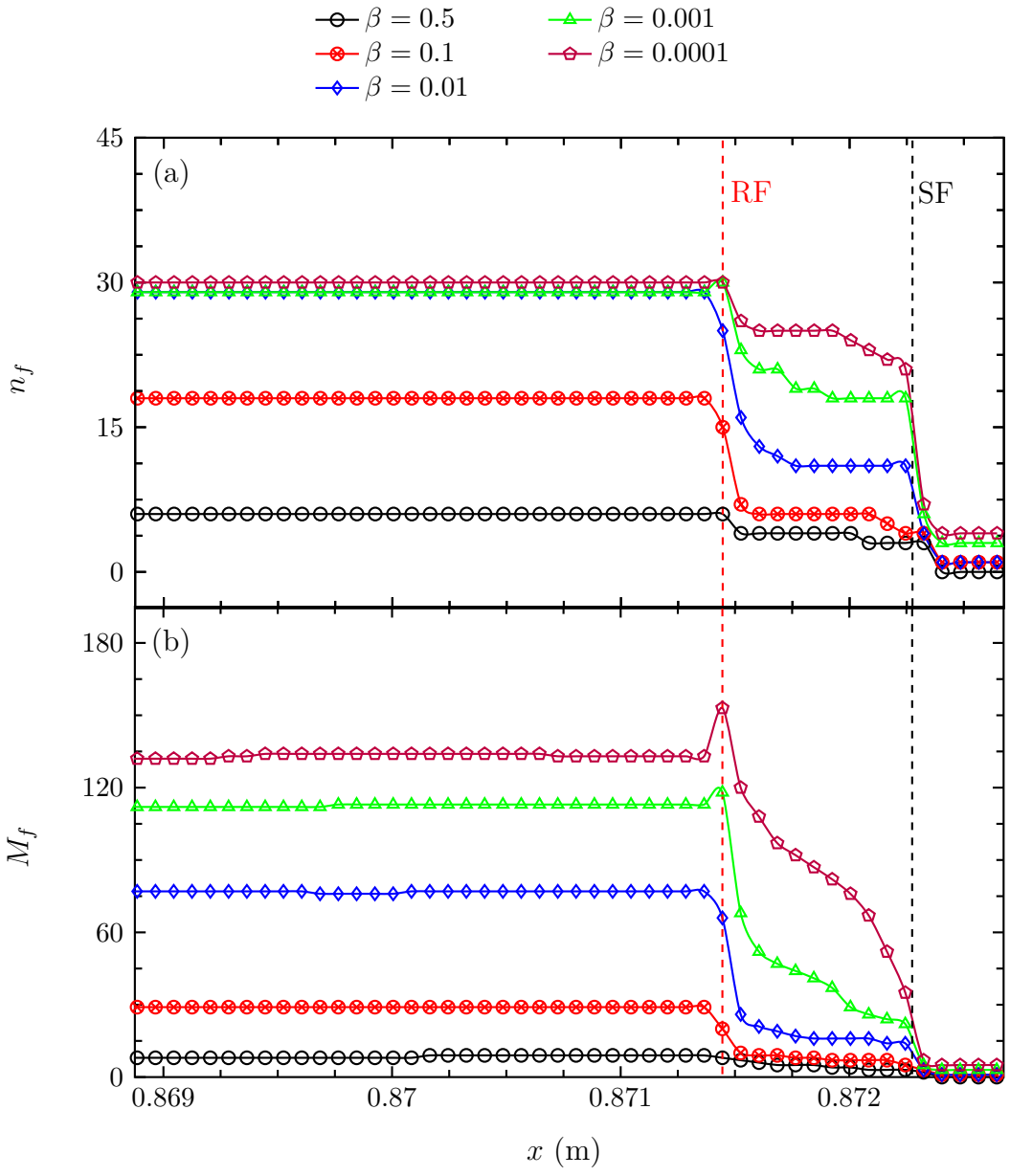


Figure 3.20: Spatial distributions of fast (a) species and (b) reaction numbers at 339 μs in the NH_3-O_2 mixture when $p_0 = 71$ kPa, $\phi = 1.0$, $T_0 = 295$ K under different safety factors. SF: the location of shock front; RF: the location of reaction front.

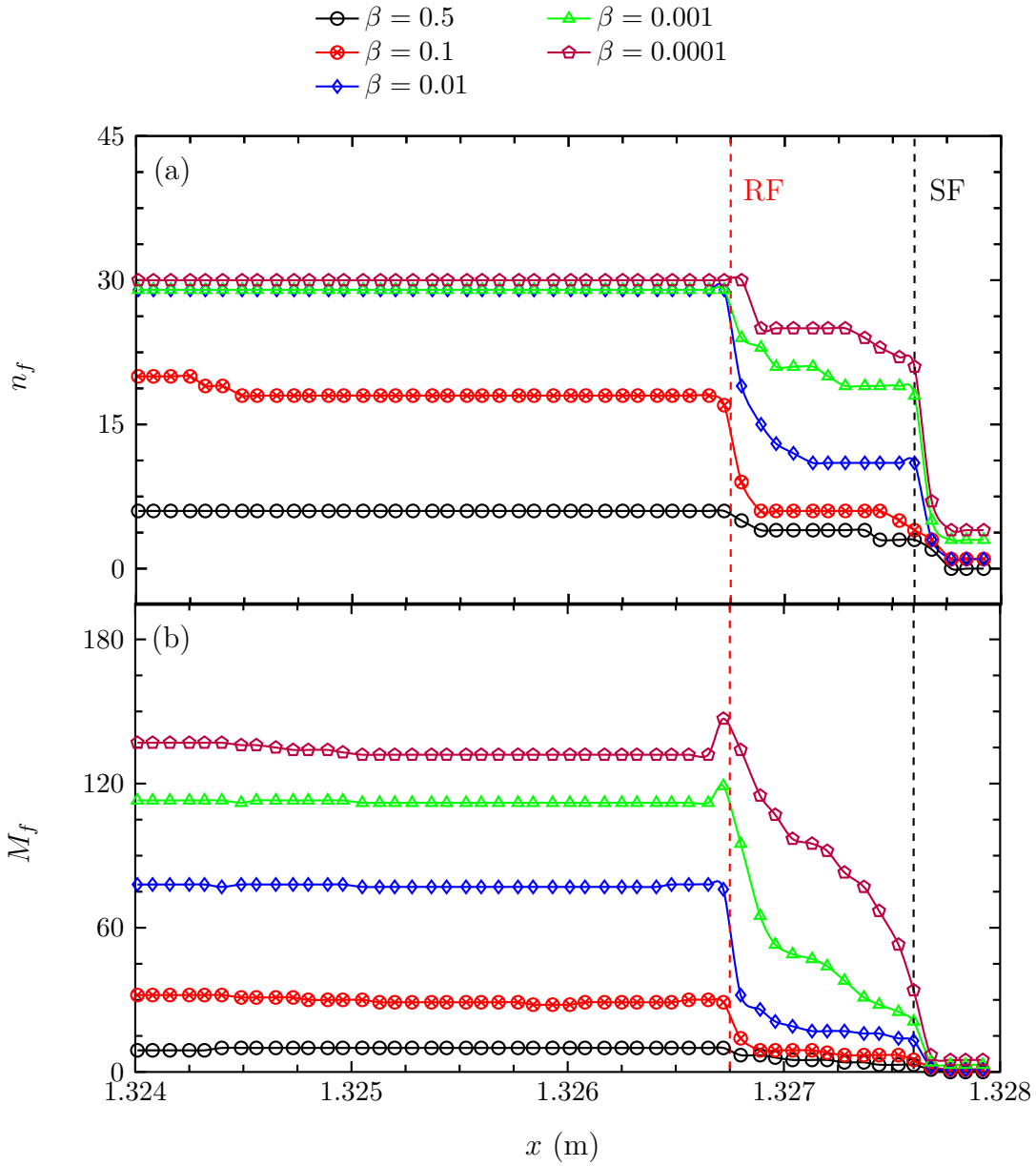


Figure 3.21: Spatial distributions of fast (a) species and (b) reaction numbers at 517 μs in the NH_3-O_2 mixture when $p_0 = 71$ kPa, $\phi = 1.0$, $T_0 = 295$ K with perturbations from ammonia droplets when $N_{d,0} = 1 \times 10^{12}/\mathrm{m}^3$ under different safety factors. SF: the location of shock front; RF: the location of reaction front.

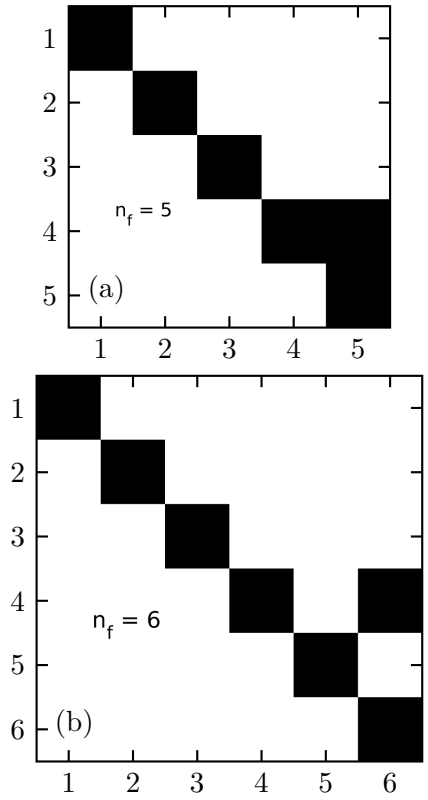


Figure 3.22: Patterns of nontrivial entries (black pixels) in Jacobians of fast chemistry subsets in (a) droplet-free and (b) droplet-laden NH_3-O_2 mixtures when $p_0 = 71$ kPa, $\phi = 1.0$, $T_0 = 295$ K when $\beta = 0.5$.

Figure 3.19.

It is seen from Figures 3.20 and 3.21 that, when $\beta = 0.5$, the fast species and reactions slightly behind the RF at 339/517 μs within the droplet-free/laden sections account for 16%/19% and 4%/5% of the total species and reactions, respectively. They are remarkably small-sized. The patterns of nontrivial entries in the Jacobians of corresponding fast chemistry subsets are further shown in Figure 3.22. Both Jacobians before and after the detonation enters the two-phase section in Figures

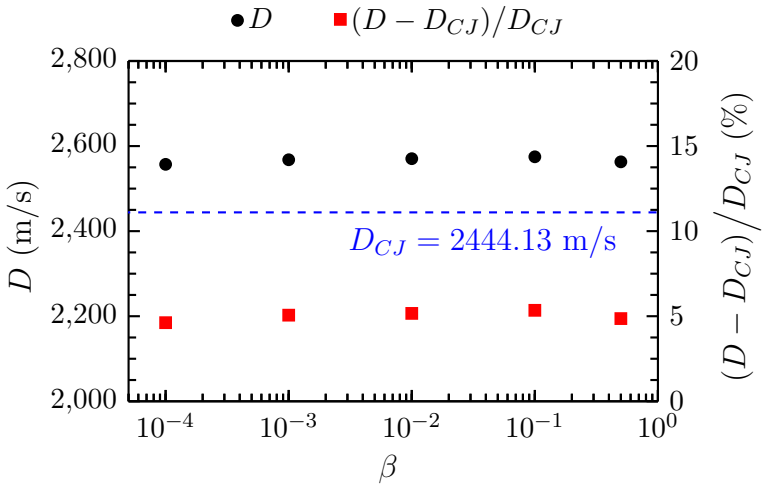


Figure 3.23: Dependences of detonation velocity and its relative error against CJ detonation velocity in percentage in the NH_3-O_2 mixture when $p_0 = 71$ kPa, $\phi = 1.0$, $T_0 = 295$ K on the safety factor. D_{CJ}: CJ detonation velocity predicted by SDToolbox [83].

3.22(a) and (b), respectively, are extremely sparse. Therefore, the AHI-S chemistry solver with $\beta = 0.5$ achieves significant computational time savings compared to the built-in OpenFOAM EulerImplicit solver, see Figure 3.18.

The dependences of detonation velocity, *i.e.*, D, and its relative error against the corresponding CJ detonation velocity, *i.e.*, $(D - D_{CJ})/D_{CJ}$, on the safety factor, β, for the baseline case before the detonation enters the two-phase section are presented in Figure 3.23. The maxima and minima of D are 2574.8 and 2557.1 m/s at $\beta = 0.1$ and 0.0001, respectively, with $(D - D_{CJ})/D_{CJ} = 5.4\%$ and 4.6%, demonstrating that results are not sensitive to the choice of β. In particular, with the optimal efficiency and the least fast species and reaction numbers using $\beta = 0.5$ among all the tests (see Figures 3.19 and 3.20), the present simulation

achieves good accuracy in calculating detonation propagation speed with $D = 2562.9$ m/s and $(D - D_{CJ})\big/D_{CJ} = 4.9\%$ within the droplet-free section. Figure 3.7 supports this. The corresponding detonation structure is also depicted in satisfactory agreement with the ZND structure when $\beta = 0.5$, see Figures 3.8 and 3.9. In general, the efficiency gain of AHISsprayDetFoam with the implementation of the AHI-S chemistry solver is confirmed in predicting the detonation propagation within both the droplet-free/laden sections.

3.7 Summary

The optimised droplet sub-models, the mixture-averaged diffusion model, and the AHI-S chemistry solver applied towards the accuracy and efficiency of the AHISsprayDetFoam solver are validated. The correct implementations of the optimised droplet sub-models are pre-tested for the subsequent simulations through reproducing the velocity and temperature evolutions of an ammonia droplet in the flowing and/or low-temperature air. The numerical results show good accuracy against the corresponding experimental and analytical data.

The accuracy and efficiency gains related to the mixture-averaged diffusion model and the AHI-S chemistry solver are examined by simulating detonation propagation in NH_3-O_2 mixtures with/without perturbations from dispersed evaporating ammonia droplets in a 1-D geometry. The accuracy of AHISsprayDetFoam in predicting the detonation propagation speed and depicting the detonation structure within the droplet-free section is verified in comparison

with the corresponding experimental and analytical data.

The mixture-averaged diffusion model and the built-in OpenFOAM diffusion model predict different pulsating instabilities in detonation propagation within both the droplet-free/laden sections. Compared to the mixture-averaged diffusion model, the built-in OpenFOAM diffusion model underestimates the absolute value of thermal diffusion around the RF but overestimates that around the SF. It also overestimates the values of species diffusion for relatively heavy species but underestimates those for relatively light species. Therefore, the mixture-averaged diffusion model shows better accuracy in depicting the detonation structure within the droplet-free section than the built-in OpenFOAM diffusion model. For gas-droplet interactions within the droplet-laden section, the built-in OpenFOAM diffusion model underestimates the local fluctuations of two-phase exchange rates. These different predictions co-contribute to the different numerical results using the two diffusion models.

Through comparing the averaged execution time per simulation step, the AHI-S chemistry solver is demonstrated to be significantly less time-consuming (45-50% faster) compared to the built-in OpenFOAM EulerImplicit solver both before and after the detonation enters the two-phase section. The numbers of fast species and reactions in the fast chemistry subset to be solved implicitly and thereby the computational cost decline with increased β from 0.0001 to 0.5. The optimal efficiency is achieved under the premise of accurate computation in the present simulations when $\beta = 0.5$.

Chapter 4

2-D Ammonia-Oxygen Detonation Study

4.1 Overview

This chapter reports the numerical results of 2-D numerical simulations of detonation propagation and extinction in two-phase gas-droplet ammonia fuel using the AHISsprayDetFoam solver developed in Chapter 2, on the premise that the 1-D application validates the capability of the solver in predicting this physical problem in Chapter 3. The research background is provided in Section 4.2. The target computational configuration of a 2-D planar channel filled with ammonia droplet-free/laden premixed ammonia-oxygen gas is introduced in Section 4.3. The detonation propagation/extinction scenarios, affected by the initial ammonia droplet number density and diameter, are discussed in Section 4.4. The two-phase

gas-droplet interactions and the droplet-laden detonation physico-chemical structure are presented in Section 4.5, followed by the analysis of the detonation extinction process in Section 4.6. The summary of this chapter is provided in Section 4.7.

4.2 Background

Zero-carbon energy carriers, as alternatives to fossil fuels, are expected to play a pivotal role towards reaching net zero by 2050. Among the energy carriers, ammonia features advantages of high energy density (22.5 MJ/kg), low storage cost (0.54 \$/kg-H_2 compared to 14.95 \$/kg-H_2 of pure hydrogen storage), considerable production and transportation volumes (∼180 million tons annually) with existing reliable infrastructure [91]. Technologies for unitising ammonia fuel, *e.g.*, in internal combustion engines [92, 93] and gas turbines [94, 95], have attracted worldwide research interest in recent years. In these research studies, other fuels are commonly added as combustion promoters. This technique tackles the slow chemical kinetics, the consequent slow burning velocity, high ignition energy, narrow flammability range, and poor flame stabilisation of pure ammonia. Other analogous techniques, *e.g.*, pre-chamber turbulent jet ignition [96] and multiple spark plugs [97], have been applied to run conventional engines with pure ammonia. However, the engine operating range typically remains narrow due to the unfavorable characteristics of ammonia for combustion [98]. Detonation offers an inherently higher heat release rate and thermodynamic efficiency than

traditional isobaric combustion, which may compensate for poor ammonia combustion properties [99, 100]. Therefore, this efficient combustion mode shows huge potential in applying ammonia to propulsion and power generation.

Some fundamental experimental studies on ammonia detonation act as premises for its practical applications. Akbar *et al.* [101] experimentally measured the detonation cell width in ammonia-oxygen (NH_3-O_2) and ammonia-nitrous oxide (NH_3-N_2O) mixtures with and without the dilution effects of nitrogen (N_2) or argon (Ar). The operating conditions cover the Equivalence Ratio (ER) of ϕ = 0.56-1, the initial pressure of p_0 = 55-91 kPa, and the "inert species" mole fraction of $X_{N_2/Ar}$ = 0-0.533. The initial temperature, T_0, is 293 K. Weng *et al.* [82] later supplemented the detonation velocity and cell width in NH_3-O_2 and NH_3-N_2O mixtures with ϕ = 0.5-1.5, p_0 = 43-100 kPa and ϕ = 0.3-1.25, p_0 = 41-80 kPa, respectively. They also compared the experimental data to analytical solutions, *i.e.*, the Chapman-Jouguet (CJ) detonation velocity and the Ng's semi-empirical detonation cell width [102], calculated by Shock & Detonation Toolbox (abbreviated as "SDToolbox" hereafter) [83] and analysed the real gas effect on ammonia detonation. Experiments on flame acceleration and Deflagration-to-Detonation Transition (DDT) in methane-ammonia-oxygen (CH_4-NH_3-O_2) mixtures were conducted by Thomas [103] in a tube. The CH_4-NH_3 mole ratio is 1:1.176; p_0 and T_0 range within 50-500 kPa and 278-473 K, respectively. The mixture fraction of O_2, *i.e.*, X_{O_2}, is 0.33-0.45. Four combustion regimes were identified, namely no ignition, ignition followed by quenching, flame propagation, and transition to detonation. DDT events were only observed for

X_{O_2} in excess of 0.39. Thomas *et al.* [104] ignited a hydrogen-ammonia-air (H_2-NH_3-air) mixture whose mass concentrations of H_2, NH_3, and air are 0.12, 0.13, and 0.75, respectively. This specific mixture composition sees little flame acceleration and no DDT in a relatively long unobstructed piping system. The explosion hazard of H_2-NH_3-air mixtures was further evaluated by Li *et al.* [76]. Three influential factors of p_0 = 50-250 kPa, ϕ = 0.6-2.0, and NH_3 addition in the fuel with its mole fraction of X_{NH_3} = 0.1-0.9, were considered, listed from the most to the least important. Jing *et al.* [105] carried out a series of DDT experiments in NH_3-O_2 mixtures with focus on impacts of ϕ. DDT did not occur under ultra-lean/rich conditions, *i.e.*, ϕ = 0.3/2.2. The peak overpressure and propagation speed of self-sustained detonation after DDT fall in ranges of 2310-2480 m/s and 25.6-28.7 bar, respectively, with ϕ = 0.6-1.6.

Numerical work on ammonia detonation, *e.g.*, 2-D flame acceleration and DDT in H_2-NH_3-O_2 mixtures [78], 1-D pulsating detonation [88] and end-gas autoignition and detonation [77] in H_2-NH_3-air mixtures, plays a significant complementary role. The detonative combustion of ammonia blends in these studies is characterised by much higher pressure and temperature than deflagration. Therefore, lower pollutant emissions of nitrogen oxides (NO_x) which considerably decrease from medium pressure to high pressure but slightly increase as temperature rises according to Xiao *et al.* [106] are expected. Detonation propulsion systems, *e.g.*, Pulse Detonation Engines (PDEs) [107] and Rotating Detonation Engines (RDEs) [108], fueled by ammonia may then provide a cleaner way of ammonia utilisation.

The study of ammonia RDE has been recently reported but is still in its infancy. Huang *et al.* [99, 100] first experimentally realised NH_3-(O_2 enriched) air and NH_3-O_2 Continuous Rotating Detonation (CRD) in a hollow chamber with Laval nozzle. The NH_3-(O_2 enriched) air CRD only maintains stable propagation when the oxygen mass fraction is over 43%. In a selected test, it propagates at 1753 m/s which represents 77.16% of the corresponding CJ velocity. The operating range of the NH_3-O_2 CRD is large – the lean limit is $\phi = 0.24$ with a nozzle contraction ratio of 2, 4, and 6. NH_3-O_2 CRD propagation velocities account for 70%-100% of the corresponding CJ velocities for all the tests. Sun *et al.* [109] performed 3-D simulations of a RDE in NH_3-H_2-(O_2 enriched) air mixtures. The detonations propagate stably under a wide range of ϕ only with the minimum hydrogen mole concentration of 0.2 in the fuel. The NO_x emissions show a logarithmic decreasing trend in the range of $\phi = 0.7$-1.4. The effects of injection total temperature, *i.e.*, T_i, and NH_3/H_2 ER, *i.e.*, ϕ_{NH_3}/ϕ_{H_2}, under a fixed global ER of $\phi_{NH_3} + \phi_{H_2} = 1$ on the feasibility and performance of NH_3-H_2-air RDE were analysed by Wang *et al.* [110]. The successful detonation propagation was found to benefit from higher T_i but lower ϕ_{NH_3}. The maximum ϕ_{NH_3} reaches 0.6, achieved at $T_i = 1000$ K.

The foregoing efforts in developing detonation-based ammonia utilisation have so far focused on ammonia as fuel in the gas phase. As ammonia is normally stored in liquid, practical combustion applications of gaseous ammonia require prior vaporisation of liquid ammonia from storage tanks. For example, a 50 kW class micro gas turbine firing ammonia [111, 112] was equipped with a vaporiser.

Its fuel supply line from the vaporiser to the combustor was heated to avoid fuel vapour condensation. Thus, the need for supply line heating necessarily prolongs the start-up time in ammonia gas turbines. A 2 MW class ammonia-natural gas co-fired gas turbine [113, 114] further used an accumulator for the ammonia gas after vaporisation. The maximum ammonia heat fraction in the fuel by Lower Heating Value (LHV) was only 20%, limited by the capacity and performance of the vaporiser and the accumulator. Large-size vaporisers and accumulators to ensure a stable supply of ammonia with higher fractions may amount to huge costs and space requirements. These drawbacks of gaseous ammonia as fuel can be mitigated by supplying ammonia in the liquid phase and direct burning of the ammonia spray. Some early attempts on stabilising liquid ammonia spray flames, *e.g.*, in gas turbine combustors [115, 116] and under engine-relevant ambient conditions [117], were unsuccessful – likely as a result of flash boiling effects and the high latent heat of ammonia vaporisation, the endothermic nature of ammonia deposition, and the slow chemical kinetics of ammonia oxidation. Recently, however, Okafor *et al.* [118, 119] reported successful liquid ammonia spray flames in swirl combustors. They achieved the stable combustion of the liquid ammonia spray with the application of preheated swirling air. They found that the co-combustion of the liquid ammonia spray with methane could further improve the flame stability, mitigate the emission of nitrous oxide (N_2O) but encourage the emission of nitric oxide (NO). Zhang *et al.* [120] experimentally visualised the ignition and diffusion combustion process of the liquid phase ammonia spray ignited by diesel jet in a constant volume vessel. Some simulations, *e.g.*, Refs.

[121–123], also shed light on the characteristics of liquid ammonia spray flames but these studies in the literature are still scarce.

The aforementioned studies enlighten the possibility of detonation propulsion systems running on the liquid ammonia spray as fuel. One of the challenges is to achieve stable detonative combustion of the liquid ammonia spray while avoiding detonation extinction. This work provides an understanding of this issue. Detonation propagation and extinction in two-phase gas-droplet ammonia fuel, affected by the initial ammonia droplet number density and diameter, are numerically investigated using the AHISsprayDetFoam solver.

4.3 Computational configuration and validation

The target computational configuration in this work is a 2-D planar channel, shown in Figure 4.1. Its dimensions are selected following those used by Xu *et al.* [124, 125] in simulations of H_2-air detonation with perturbations from fine water sprays and dilute inert particles. The coordinate origin lies at the centre of the left end. The length and width along x- and y-directions, *i.e.*, the streamwise and spanwise directions, respectively, are 0.3 and 0.025 m. Following Refs. [124, 125], the simulated domain is open to the surroundings at the left and right ends where the "zeroGradient" boundary condition is specified for all variables. The top and bottom ends are assumed to be periodic with the boundary conditions of all variables set as "cyclic". Note that 1-D and 2-D scenarios are still treated as 3-D in OpenFOAM by discretising the reduced directions (z-direction here) with one

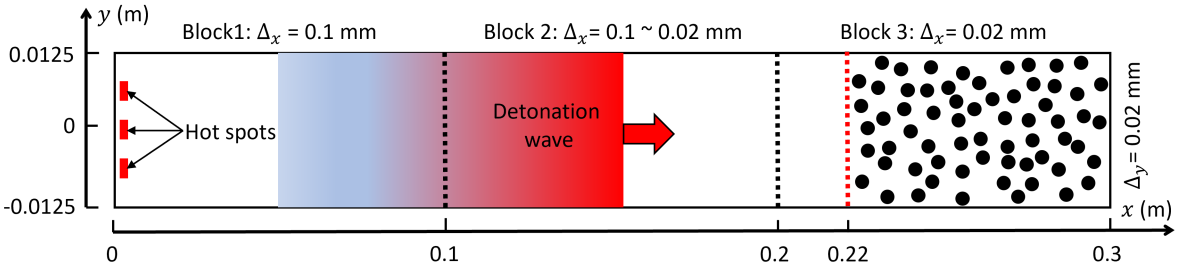


Figure 4.1: Schematic of 2-D computational domain filled with premixed NH_3-O_2 gas. Circles: ammonia droplets.

mesh and enforcing the "empty" boundary condition for all variables. The height of the simulated domain along z-direction, *i.e.*, 0.2 mm, affects some quantities of the liquid phase, *e.g.*, droplet number density, N_d, and volume fraction, V_{fd}, and further affects the gas phase solutions.

The 2-D geometry includes detonation driver (x = 0-0.1 m), development (x = 0.1-0.22 m), and two-phase (x = 0.22-0.3 m) sections. They are filled with premixed NH_3-O_2 gas at $t = 0$. In the gas phase, the initial velocity is zero; the initial temperature, T_0, and pressure, p_0, are 295 K and 71 kPa, respectively; the fuel-oxidizer equivalence ratio, ϕ, ranges from 0.55 to 1.55. The detonation propagation and extinction in the droplet-laden carrier gas are only simulated for the baseline case with $\phi = 1.0$. The Detonation Wave (DW) is initiated by three 2 mm-thick Hot Spots (HS) with high pressure ($100p_0$) and high temperature ($10T_0$) vertically placed at the left end of the detonation driver section. This ignition method has been widely used, *e.g.*, in Refs. [9, 124, 125], as the interactions between the DW from each individual HS quickly trigger detonation frontal instabilities. The DW is a complex of preceding Shock Front (SF) and auto-igniting Reaction Front (RF)

with an in-between induction zone. Its frontal instabilities are observed in the form of a series of transient detonation cells whose apexes represent the locations where triple points on the detonation front collide [89], seen later in Section 4.4. Note that preliminary tests with a lower HS pressure ($50p_0$) cannot successfully initiate a DW but with a higher HS pressure ($200p_0$) initiate a highly overdriven DW. The x/y-direction mesh size within the detonation driver section is $\Delta_x = \Delta_y = 0.1$ mm (Block 1).

The DW upon initiation propagates downstream and later enters the detonation development section which is discretised using non-uniform meshes along x-direction transiting from $\Delta_x = 0.1$ mm at $x = 0.1$ m to $\Delta_x = 0.02$ mm at $x = 0.2$ m (Block 2). The y-direction mesh size is $\Delta_y = 0.05$ mm in Block 2. Block 3 starting at $x = 0.2$ m as the main focus sees the minimum and uniform x/y-direction mesh size of $\Delta_x = \Delta_y = 0.02$ mm. The total mesh grid number in Blocks 1, 2, and 3 is 12,500,000. The Half Reaction Length (HRL) of the Zel'dovich-Neumann-Döring (ZND) structure predicted by SDToolbox [83] is $l_{1/2} = 0.83$ mm for the baseline case. The x-direction mesh size of $\Delta_x = 0.02$ mm in Block 3 corresponds to about 42 grids in the HRL and over 42 grids in the thickened induction zone of the DW within the two-phase section due to droplet breakup, heating, and vaporisation [126]. The magnitude of the physical time step, Δt, corresponds to 10^{-10} s for the detonation propagation and extinction in Block 3, with the Courant-Friedrich-Lewy (CFL) number of the gas phase set as 0.05.

Inside the two-phase section, initially, quiescent and mono-sized ammonia droplets are randomly distributed. Their initial temperature, $T_{d,0}$, density, $\rho_{d,0}$,

and heat capacity, $c_{pd,0}$, are 232.9 K, 689.9 kg/m^3, and 4,406.6 J/(kg·K), respectively. Different combinations of the initial droplet number density, $N_{d,0} = 1.0 \times 10^{12}$, 1.5×10^{12}, or 2.0×10^{12} /m^3, and diameter, $d_0 = 5$, 10, or 15 μm, are considered.

The numerical accuracy of present simulations in predicting the critical quantities of the two-phase gas-droplet ammonia detonation is premised upon those of the corresponding gaseous ammonia detonation. Therefore, it is conducive to first validate the detonation velocity, D, and cell width, λ, in the droplet-free carrier gas against the experimental measurements by Weng *et al.* [82] and analytical solutions, *i.e.*, the CJ detonation velocity and the Ng's semi-empirical detonation cell width [102], calculated by SDToolbox [83]. Figure 4.2 shows the numerical, experimental, and analytical results of D and λ with respect to ϕ. A detailed chemical mechanism for ammonia combustion including 32 species and 203 reactions [84] is applied for the numerical and analytical results. In Figure 4.2(a), the values of D from the present simulations are the averaged propagation speed of the DW from $x = 0.2$ to 0.3 m in Block 3. They are calculated based on the movement of the RF (or the SF) over the corresponding time interval, *e.g.*, 80-119 μs for the baseline case, *i.e.*, $\mathrm{C_{base}}$ marked in Figures 4.2(a) and (b). The locations of RF and SF are identified where the Heat Release Rate (HRR) and the magnitude of the pressure gradient, $|\nabla p|$, peak, respectively. Other criteria, *e.g.*, the mass fraction of ammonia ($Y_{\mathrm{NH_3}}$), are also tested but yield nearly identical results on the location identification. The numerical results of D see an evolutionary tendency regarding ϕ in agreement with the experimental and

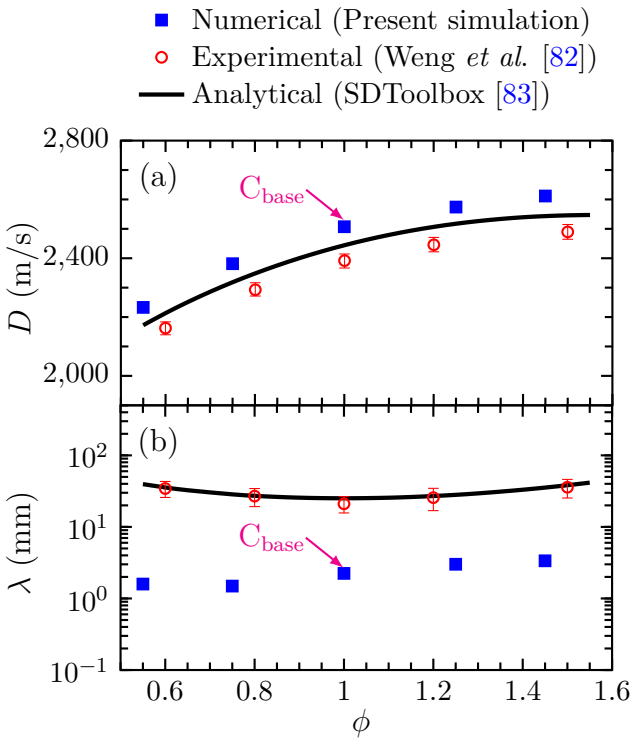


Figure 4.2: Numerical, experimental, and analytical results of detonation (a) velocity, D, and (b) cell width, λ, with respect to equivalence ratio, ϕ, in droplet-free premixed NH_3-O_2 gas. C_{base}: the baseline case with $\phi = 1.0$.

analytical data. Their magnitudes show good accuracy and are slightly overestimated by about 5% and 2.5% against the experimental and analytical data, respectively. Note that the numerical overpredictions of D in comparison with the corresponding CJ detonation velocities suggest slightly overdriven detonations initiated using the ignition method in the present simulations, according to Ref. [89].

In Figure 4.2(b), the values of λ from the present simulations are the averages of maximum and minimum cell widths of the DW near $x = 0.3$ m in Block 3. The

detonation cells are recorded by the trajectory of peak pressure, p, in each mesh as the DW propagates downstream. The numerical results of λ are less dependent on ϕ than the experimental and analytical data. Their magnitudes are highly underestimated and represent only about 10% of the experimental and analytical data. The noticeable numerical underpredictions of λ are likely associated with the overdriven detonations initiated in the present simulations. For example, the DW reaches the stage of $x/l_{1/2} \approx 360$ at $x = 0.3$ m for the baseline case with $l_{1/2} = 0.83$ mm. The relatively small values of λ are anticipated as a characteristic of the overdriven detonation at this stage, compared to those formed later at the detonation self-sustained propagation stage [127]. Besides, some other influential factors, *e.g.*, unmimicked geometrical configuration and unavoidable nonidealities [128] in the experimental work, and the chemical mechanism, may also play a part in the mismatched experimental/analytical and numerical results of λ. In general, the present simulations respectively fairly overestimate D and underestimate λ of the DW in the premixed NH_3-O_2 gas.

4.4 Detonation propagation/extinction diagram

The present simulations in the ammonia droplet-laden NH_3-O_2 gas with $\phi = 1.0$ in the gas phase (the baseline case) are parametrised by the initial droplet number density, $N_{d,0}$, and diameter, d_0. The detonation propagation/extinction scenarios with perturbations from the ammonia droplets with $N_{d,0} = 1.0 \times 10^{12}$, 1.5×10^{12}, or 2.0×10^{12} /m^3 and $d_0 = 5$, 10, or 15 μm are summarised in a diagram in Figure

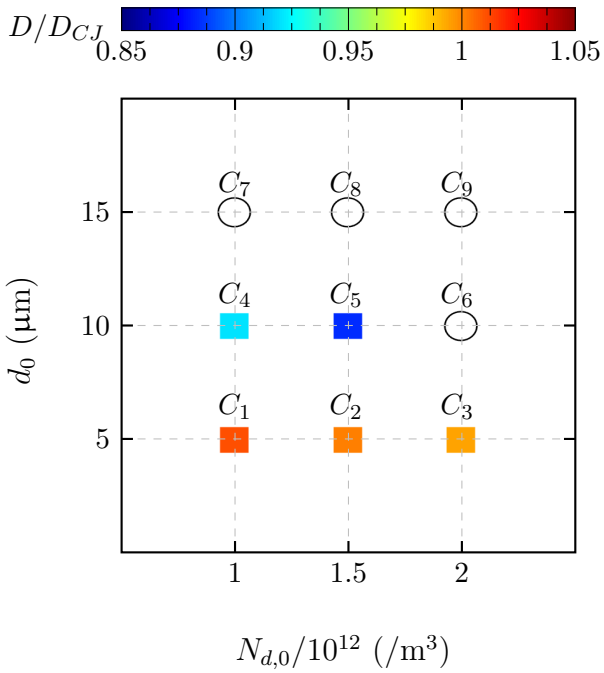


Figure 4.3: Diagram of detonation propagation and extinction in droplet-laden premixed NH_3-O_2 gas with different initial droplet number density, $N_{d,0}$, and diameter, d_0. Squares: propagation scenarios; Circles: extinction scenarios.

4.3. They are labelled as Cases C_1-C_9. The square symbols for Cases C_1-C_5 in the diagram denote the sustained propagation of the DW with the coupled RF and SF until the right end of the two-phase section. They are coloured by the ratio between the averaged propagation speed of the DW over the entire two-phase section and the CJ detonation velocity for the droplet-free baseline case, D/D_{CJ}. The maxima and minima of D/D_{CJ} are 1.01 for Case C_1 with $N_{d,0} = 1.0 \times 10^{12}$ /m^3, $d_0 = 5$ μm and 0.88 for Case C_5 with $N_{d,0} = 1.5 \times 10^{12}$ /m^3, $d_0 = 10$ μm, respectively. The unquenched DWs are attenuated in strength when crossing the ammonia droplets in contrast to their droplet-free counterpart with $D/D_{CJ} = 1.03$.

They are less perturbed under lower values of $N_{d,0}$ and d_0, characterised by lower velocity deficits relative to the corresponding droplet-free detonation velocity. The open circle symbols for Cases C_6-C_9 in the diagram denote the ultimate quenching of the DW which is characterised by the decoupling of the RF and SF after the DW travels a finite distance within the two-phase section. This situation always occurs under the relatively large initial droplet diameter of $d_0 = 15$ μm for Cases C_7-C_9. Note that the droplet-laden distances that the DWs travel before quenching are shortened as $N_{d,0}$ increases with fixed $d_0 = 15$ μm, though not demonstrated in Figure 4.3.

Cases C_4-C_6 with $N_{d,0} = 1.0 \times 10^{12}$, 1.5×10^{12}, and 2.0×10^{12} /m^3, respectively, are selected to further examine the impacts of $N_{d,0}$ on the detonation propagation and extinction under fixed $d_0 = 10$ μm. Figure 4.4 depicts the contours of detonation peak pressure trajectories within their two-phase sections and the droplet-free baseline case for comparison. It is seen that the addition of the ammonia droplets in the carrier gas considerably changes the detonation cell structure by different degrees affected by $N_{d,0}$. The propagation/extinction behaviour of the DW is changed accordingly. For the relatively low and intermediate values of $N_{d,0} = 1.0 \times 10^{12}$ and 1.5×10^{12} /m^3 in Figures 4.4(b) and (c), the detonation cells partially fade subject to reduced pressure maxima within roughly $x = 0.27$-0.28 m and $x = 0.245$-0.26 m, respectively. It is associated with weakened chemical reactivity at the triple points of the partially decoupled DW. The partial decoupling of the DW with localised thickened induction zones is triggered by the two-phase gas-droplet interactions, elaborated later in Section 4.5.

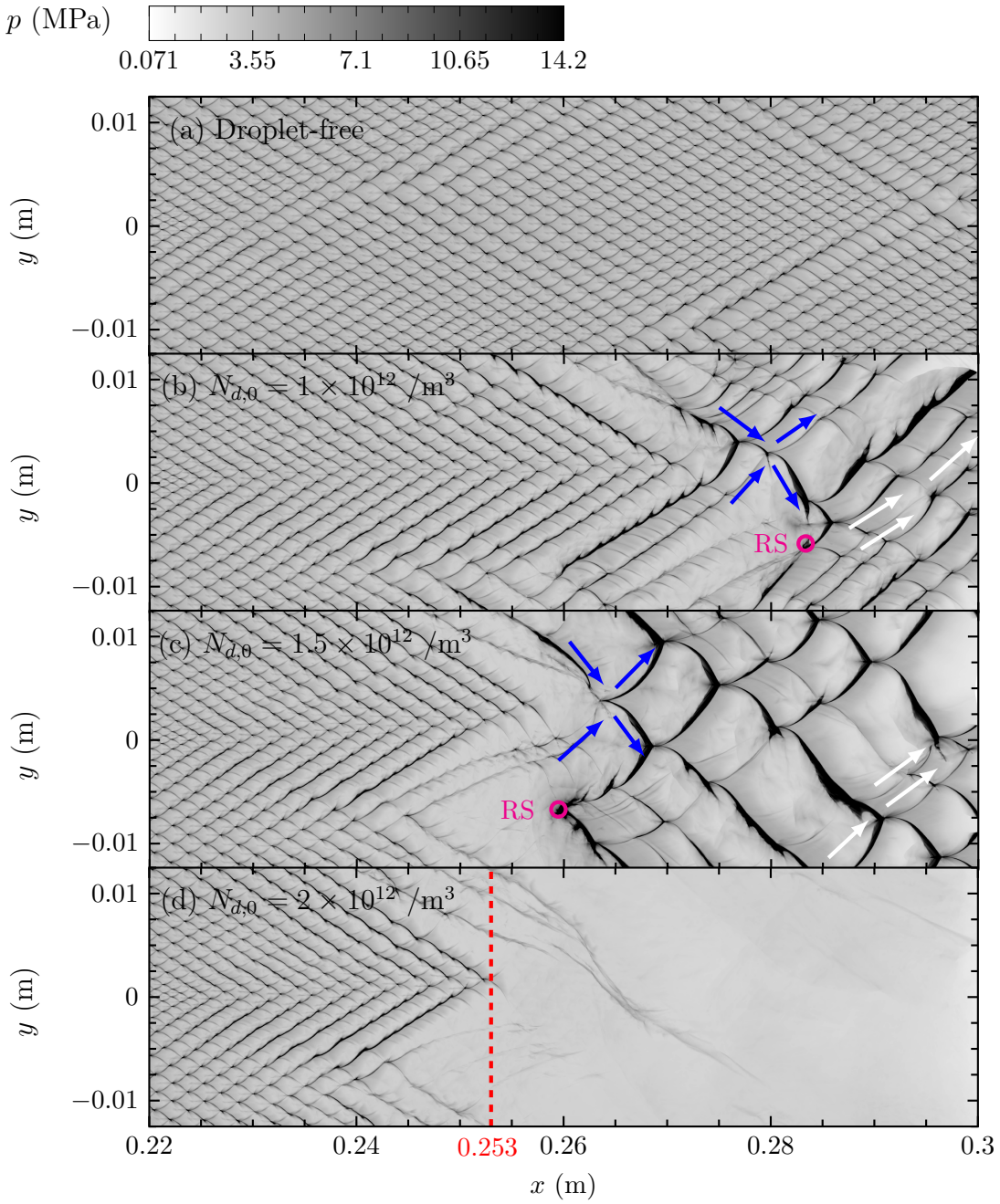


Figure 4.4: Trajectories of detonation peak pressure in (a) droplet-free and (b)-(d) droplet-laden premixed NH_3-O_2 gas with initial droplet diameter of $d_0 = 10$ μm. RS: reignition spot. Blue arrows mark triple point collision and thus re-amplification on detonation front; White arrows mark detonation cell merging and splitting.

The detonation cells subsequently restore following the temporary fading because of two primary incentives. One is the triple point collision and thus re-amplification on the detonation front; the other is the detonation reignition at a tip of the RF where the shock focusing/collision enhances the localised chemical reactivity [129, 130]. The former and the latter are marked by blue arrows and the Reignition Spot (RS), respectively, in Figures 4.4(b) and (c). The restored detonation cell widths are noticeably increased and positively correlated to $N_{d,0}$. Similar spatial variations of the detonation cells in hydrogen/air gas with fine water sprays were reported by Xu *et al.* [124]. The detonation frontal instabilities in the post-restoration areas are also enhanced with detonation cell merging and splitting, marked by white arrows in Figures 4.4(b) and (c), respectively, observed. For the relatively high value of $N_{d,0} = 2.0 \times 10^{12}$ /m^3 in Figure 4.4(d), the detonation cells completely fade at around $x = 0.253$ m, *i.e.*, the red dashed line, indicating the quenching of the DW.

Cases C_2, C_5, and C_8 with $d_0 = 5$, 10, and 15 μm, respectively, are selected to further examine the impacts of d_0 on the detonation propagation and extinction under fixed $N_{d,0} = 1.5 \times 10^{12}$ /m^3. Figure 4.5 depicts the contours of detonation peak pressure trajectories within their two-phase sections. Note that Figure 4.5(b) with $d_0 = 10$ μm is the same as Figure 4.4(c), where the initial droplet diameter is $d_0 = 10$ μm. For the relatively low value of $d_0 = 5$ μm in Figure 4.5(a), the DW is almost unperturbed by the ammonia droplets. The detonation cell widths and regularity are mostly sustained. For the relatively high value of $d_0 = 15$ μm in Figure 4.5(c), the DW quenches early at around $x = 0.242$ m, *i.e.*, the red dashed

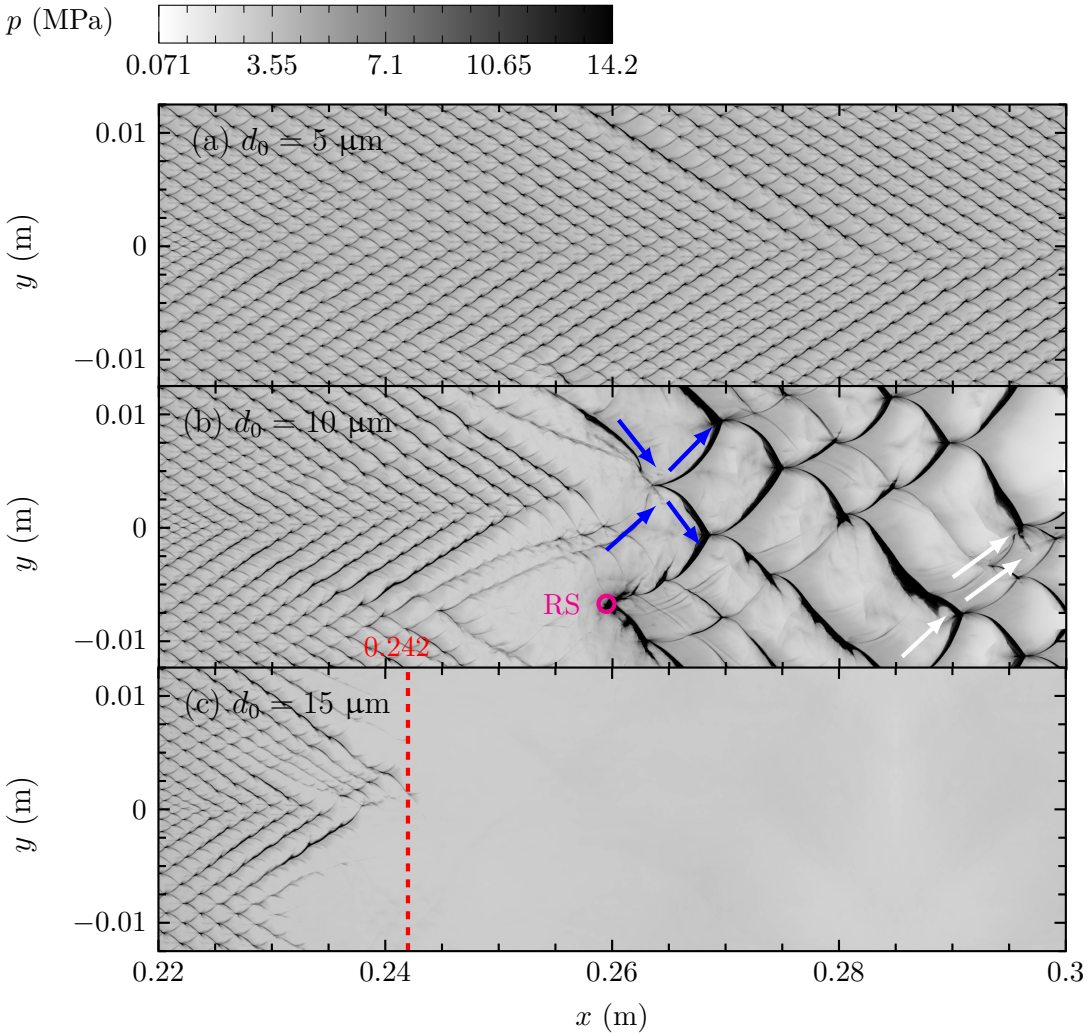


Figure 4.5: Trajectories of detonation peak pressure in droplet-laden premixed NH_3-O_2 gas with initial droplet number density of $N_{d,0} = 1.5 \times 10^{12}$ /m^3. RS: reignition spot. Blue arrows mark triple point collision and thus re-amplification on detonation front; White arrows mark detonation cell merging and splitting.

line, with the complete fading of the detonation cells.

4.5 Two-phase gas-droplet interaction

The numerical results of droplet volume fraction, V_{fd}, two-phase gas-droplet mass, x-direction momentum, and energy exchange rates, *i.e.*, S_{mass}, $S_{\text{momentum},x}$, and S_{energy}, respectively, are firstly analysed in this section. They are compared among the afore-selected representative simulations before the DWs arrive at $x = 0.24$ m. The critical location of $x = 0.24$ m is identified slightly ahead where the earliest detonation extinction takes place, *i.e.*, at $x = 0.242$ m for Case C_8.

The quantitative dependences of V_{fd}, S_{mass}, $S_{\text{momentum},x}$, and S_{energy} on $N_{d,0}$ and d_0 are presented in Figure 4.6. The inter-phase exchange quantities are time and volume averaged during the period when the DWs propagate within the two-phase section until $x = 0.24$ m. The positive values of S_{mass} suggest the mass transfer from the liquid phase to the gas phase, while the negative values of $S_{\text{momentum},x}$ and S_{energy} suggest the momentum and energy transfers from the gas phase to the liquid phase. They match with the evaporation, acceleration, and heating of the ammonia droplets, respectively. When d_0 is fixed at 10 μm, *i.e.*, the black circle scatters, the magnitudes of V_{fd}, S_{mass}, $S_{\text{momentum},x}$, and S_{energy} are found to be positively and approximately linearly correlative to $N_{d,0}$ which varies from 1.0×10^{12}, 1.5×10^{12}, to 2.0×10^{12} /m^3. When $N_{d,0}$ is fixed at 1.5×10^{12} /m^3, *i.e.*, the blue square scatters, whereas, they grow nonlinearly with the increase of d_0 from 5, 10, to 15 μm. The phenomenon is especially significant for V_{fd} as the droplet volume is proportional to the cubic of the droplet diameter. S_{mass}, $S_{\text{momentum},x}$, and S_{energy} occur at the droplet surface which is proportional to the square of the droplet diameter.

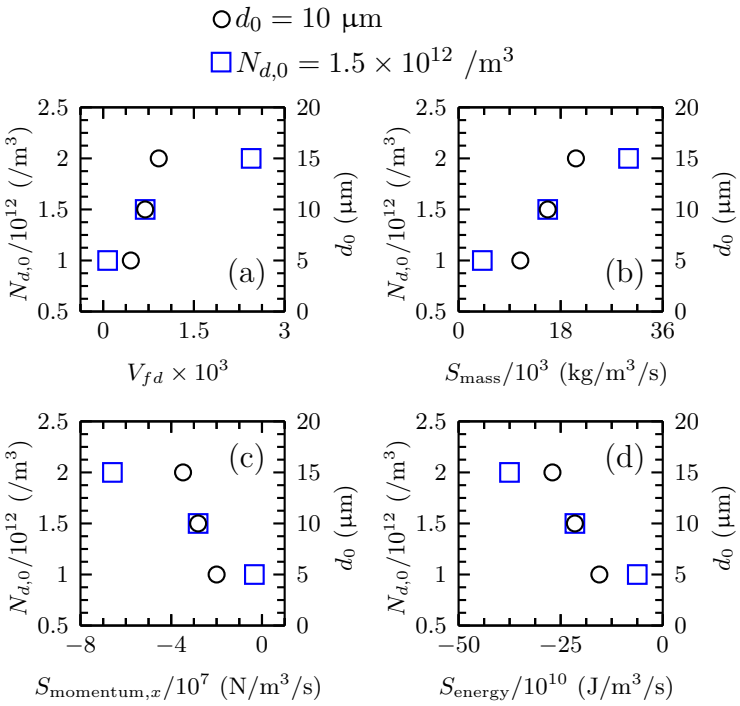


Figure 4.6: Time and volume averaged (a) droplet volume fraction, V_{fd}, and interphase (b) mass, S_{mass}, (c) momentum along x-direction, $S_{\mathrm{momentum},x}$, and (d) energy exchange rates, $S_{\mathrm{energy},x}$, in droplet-laden NH_3-O_2 gas as functions of initial droplet number density, $N_{d,0}$, (black circle scatters) and diameter, d_0, (blue square scatters) when detonation propagates from $x = 0.22$ to 0.24 m.

Figures 4.7 and 4.8 show the spatial profiles of y-direction averages of V_{fd}, S_{mass}, $S_{\mathrm{momentum},x}$, and S_{energy} along x-direction at 95 μs when the DWs are close to $x = 0.24$ m. The former includes Cases C_4-C_6 with $N_{d,0} = 1.0 \times 10^{12}$, 1.5×10^{12}, and 2.0×10^{12} /m^3, respectively, under fixed $d_0 = 10$ μm. The latter includes Cases C_2, C_5, and C_8 with $d_0 = 5$, 10, and 15 μm, respectively, under fixed $N_{d,0} = 1.5 \times 10^{12}$ /m^3. In addition to the DW, the two-phase Contact Surface (CS) is the other characteristic front as the interface between the droplet-free and droplet-

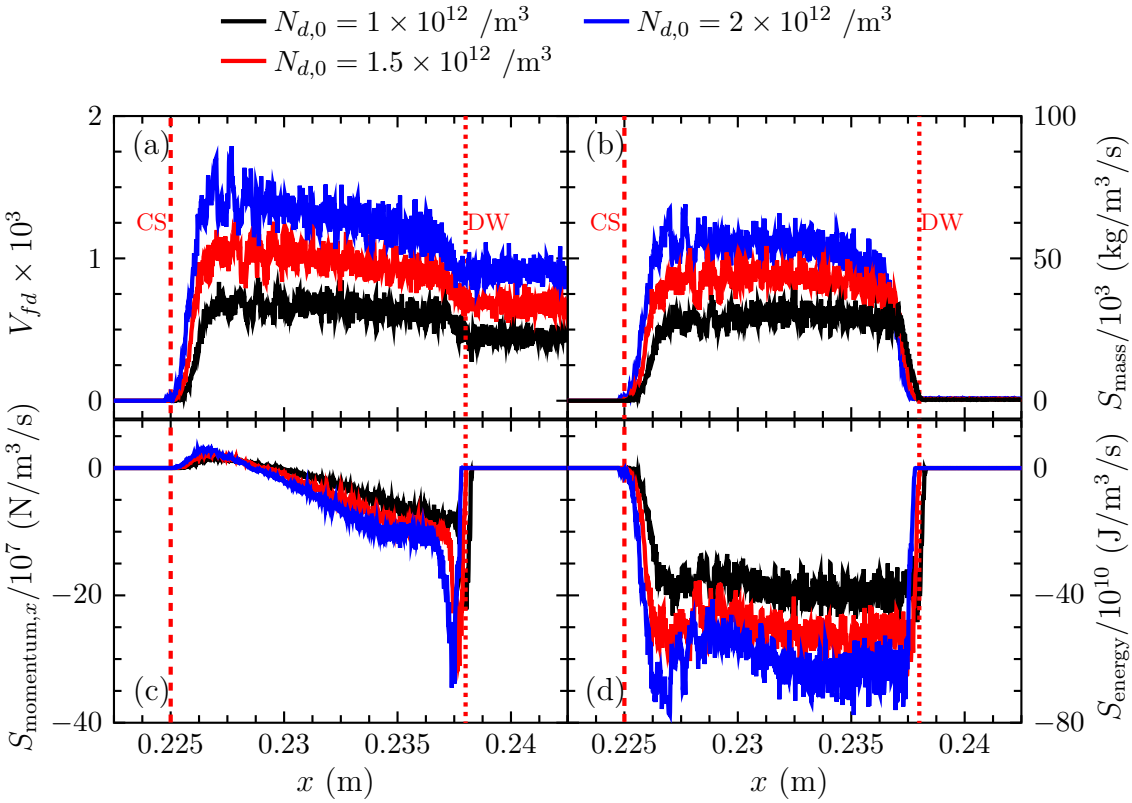


Figure 4.7: Spatial profiles of y-direction averages of (a) droplet volume fraction, V_{fd}, and inter-phase (b) mass, (c) x-direction momentum, and (d) energy exchange rates (denoted as S_{mass}, $S_{\text{momentum},x}$, and S_{energy}, respectively) along x-direction in droplet-laden NH_3-O_2 gas with initial droplet diameter of $d_0 = 10$ μm at 95 μs. DW and CS: the locations of detonation wave and contact surface, respectively, for Case C_5 with $N_{d,0} = 1.5 \times 10^{12}$ /m^3.

laden carrier gas. The two-phase gas-droplet interactions mainly proceed between the DW and the CS. Consequently, the locations of DW and CS are identified where the magnitudes of S_{mass}, $S_{\text{momentum},x}$, and S_{energy} jump from near-zero and plunge to near-zero, respectively.

In Figure 4.7, the locations of the DW and the CS under all the values of $N_{d,0}$

fairly overlap at 95 μs. For example, the DW and the CS lie at around $x = 0.238$ and 0.225 m, respectively, *i.e.*, the red dotted and dashed lines, for Case C_5 with $N_{d,0} = 1.5{\times}10^{12}$ /m^3. The influences of $N_{d,0}$ on the droplet-laden detonation velocity are not noticeable yet but accumulate onto the detonation propagation/extinction behaviour at later stages, see Figures 4.4(b)-(d). The localised fluctuations of V_{fd} in the intact carrier gas ahead of the DW in Figure 4.7(a) are attributed to the non-uniformity of droplet number per mesh, as the ammonia droplets are initially randomly distributed. Behind the DW, the droplet motion driven by the flowing carrier gas further strengthens the localised fluctuations of V_{fd}. The values of S_{mass}, $S_{\text{momentum},x}$, and S_{energy} in Figures 4.7(b)-(d) also intensely oscillate following V_{fd}. They see climbing magnitudes with the increase of $N_{d,0}$ from 1.0×10^{12}, 1.5×10^{12}, to 2.0×10^{12} /m^3, so does V_{fd}. S_{mass} and S_{energy} are almost constants between the DW and the CS, indicating almost unchanged intensities of the droplet evaporation and heat absorption in the detonated carrier gas. The magnitude of $S_{\text{momentum},x}$ is extremely large closely behind the DW and declines towards the CS. The ammonia droplets which freshly enter the post-DW region respond quickly to the local gaseous velocity. They well follow the local carrier gas and travel ahead rather than pile up ahead of the CS, leading to the nearly uniform V_{fd} between the DW and the CS [48].

In Figure 4.8 at 95 μs, the DW and the CS lie at around $x = 0.239$ and 0.227 m, respectively, *i.e.*, the black dotted and dashed lines, for Case C_2 with $d_0 = 5$ μm. They lie at around $x = 0.237$ and 0.224 m, respectively, *i.e.*, the blue dotted and dashed lines, for Case C_8 with $d_0 = 15$ μm. The locations of the DW and the CS

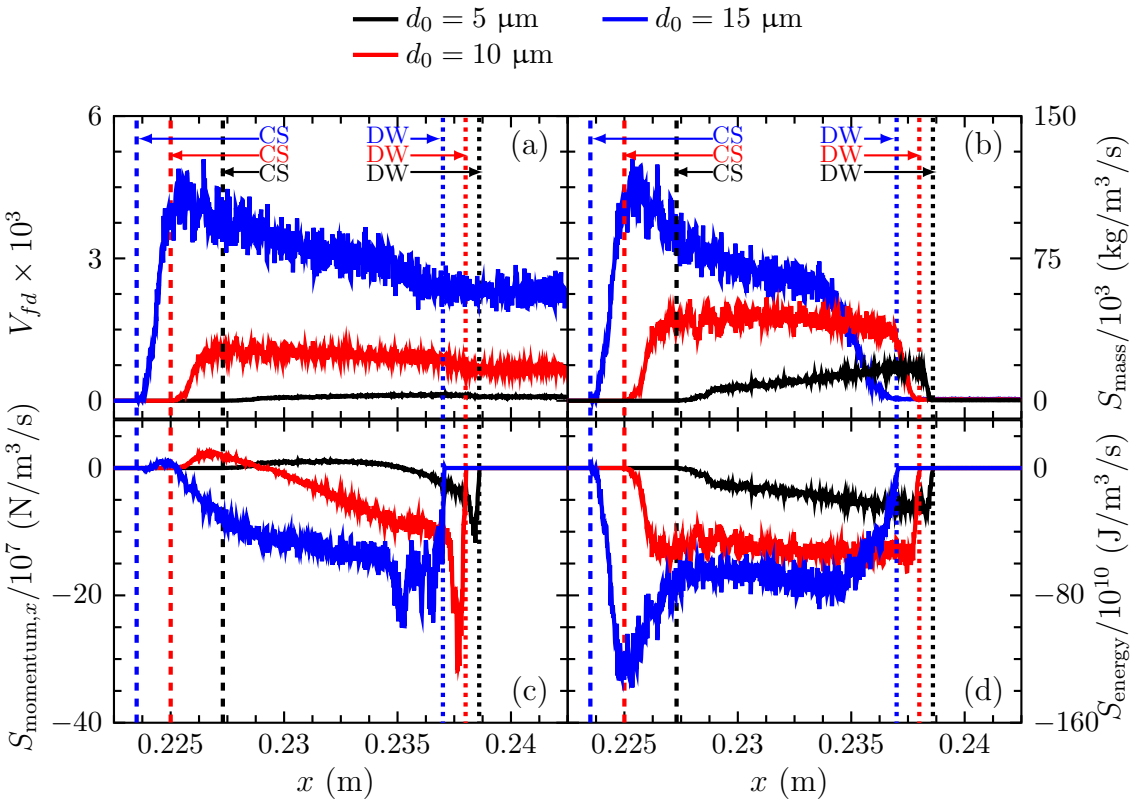


Figure 4.8: Spatial profiles of y-direction averages of (a) droplet volume fraction, V_{fd}, and inter-phase (b) mass, (c) x-direction momentum, and (d) energy exchange rates (denoted as S_{mass}, $S_{\mathrm{momentum},x}$, and S_{energy}, respectively) along x-direction in droplet-laden NH_3-O_2 gas with initial droplet number density of $N_{d,0} = 1.5 \times 10^{12}$ /m^3 at 95 μs. DW and CS: the locations of detonation wave and contact surface, respectively.

are different among Cases C_2, Case C_5 with $d_0 = 10$ μm, and C_8. The droplet-laden detonation velocity has been influenced more by the different values of d_0 than $N_{d,0}$ at the particular moment, which supports Figure 4.6. The magnitudes of V_{fd}, S_{mass}, $S_{\mathrm{momentum},x}$, and S_{energy} rise on the whole as d_0 grows from 5, 10, to 15 μm. V_{fd}, S_{mass}, and S_{energy} see decreased and increased tendencies in magnitude from the DW

to the CS when $d_0 = 5$ and 15 μm, respectively, in comparison with their almost unchanged values when $d_0 = 10$ μm. The magnitude of $S_{\text{momentum},x}$ immediately peaks and drops to zero behind the DW when $d_0 = 5$ μm. It remains non-zero until quite close to the CS with the maxima lasting much longer near the DW when $d_0 = 15$ μm. These phenomena result from the fact that droplet momentum and thermal response times are positively correlated to the droplet diameter [48]. The ammonia droplets with $d_0 = 5$ μm are completely evaporated, accelerated, and heated most quickly upon access into the post-DW region. However, those with $d_0 = 15$ μm are still partially evaporated, comparatively low-speed and thus accumulated ahead of the CS.

The critical quantities of the gas and liquid phases, *i.e.*, gaseous ammonia volume fraction, X_{NH_3}, x-direction velocity, u_x, temperature, T, and droplet diameter, d, x-direction velocity, $u_{d,x}$, temperature, T_d, directly respond to the inter-phase mass, momentum, and energy transfers. Their spatial distributions for Case C_5 with $N_{d,0} = 1.5 \times 10^{12}$ /m^3 and $d_0 = 10$ μm at 95, 105, and 115 μs are presented in Figures 4.9 and 4.10. The three instants correspond to when the detonation cells sustain, fade, and restore, respectively, see Figure 4.4(c) or Figure 4.5(b). At 95 μs in Figures 4.9(a) and 4.10(a), the DW and the CS are marked in the gaseous and droplet contours, respectively. The detonation frontal instabilities are reflected in the wrinkling of the DW with multiple bumps and depressions. The ammonia droplets right behind the DW and ahead of the CS enter the post-DW region at the earliest and the latest, respectively. The latter whose evaporation, acceleration, and heat absorption are prolonged own relatively small

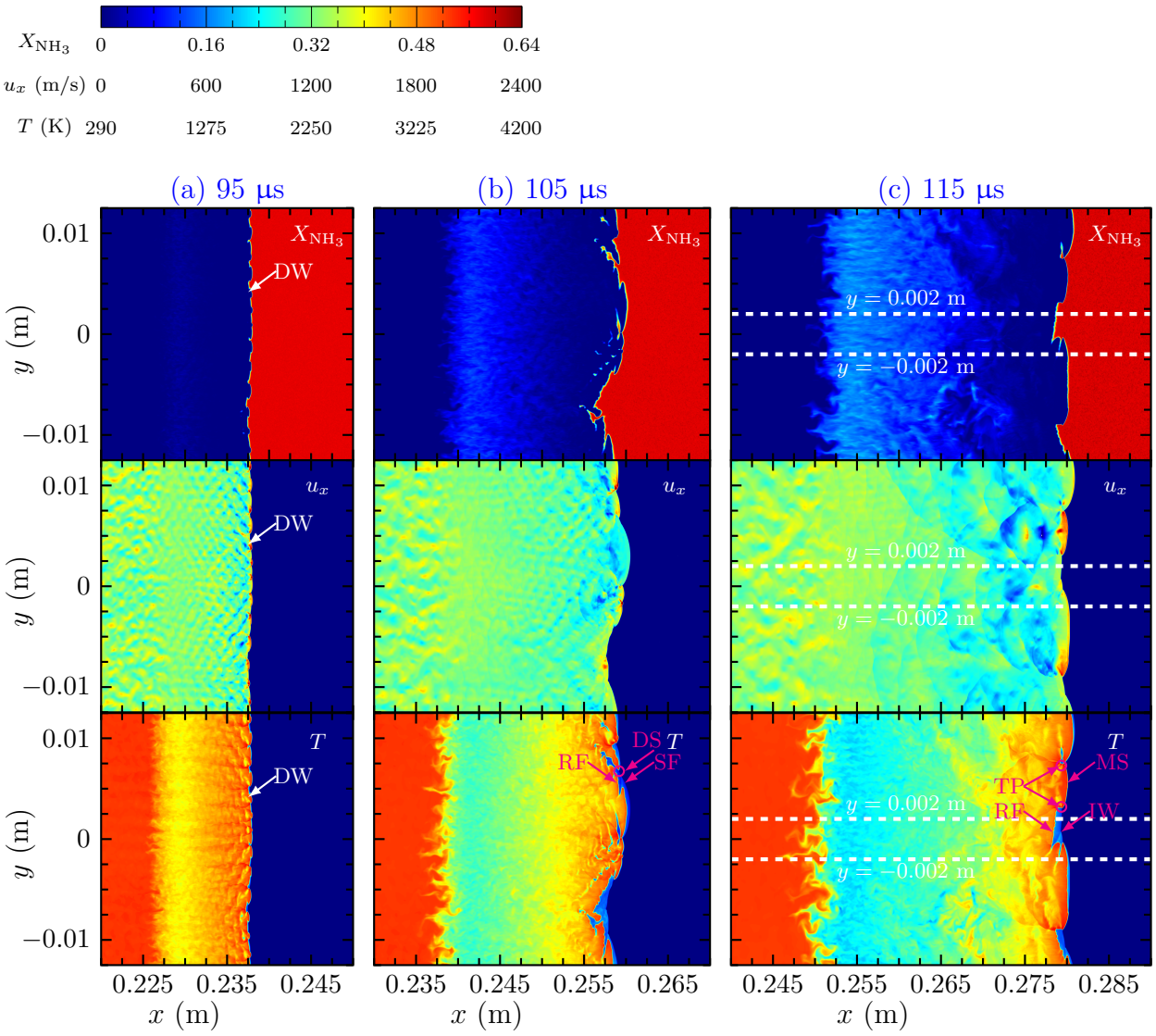


Figure 4.9: Spatial distributions of gaseous ammonia volume fraction, X_{NH_3}, x-direction velocity, u_x, and temperature, T, in droplet-laden NH_3-O_2 gas with initial droplet density number and diameter of $N_{d,0} = 1.5 \times 10^{12}$ /m^3 and $d_0 = 10$ μm at (a) 95, (b) 105, and (c) 115 μs. DW: detonation wave; RF: reaction front; SF: shock front; DS: detonative spot; MS: Mach stem; IW: incident wave; TP: triple point.

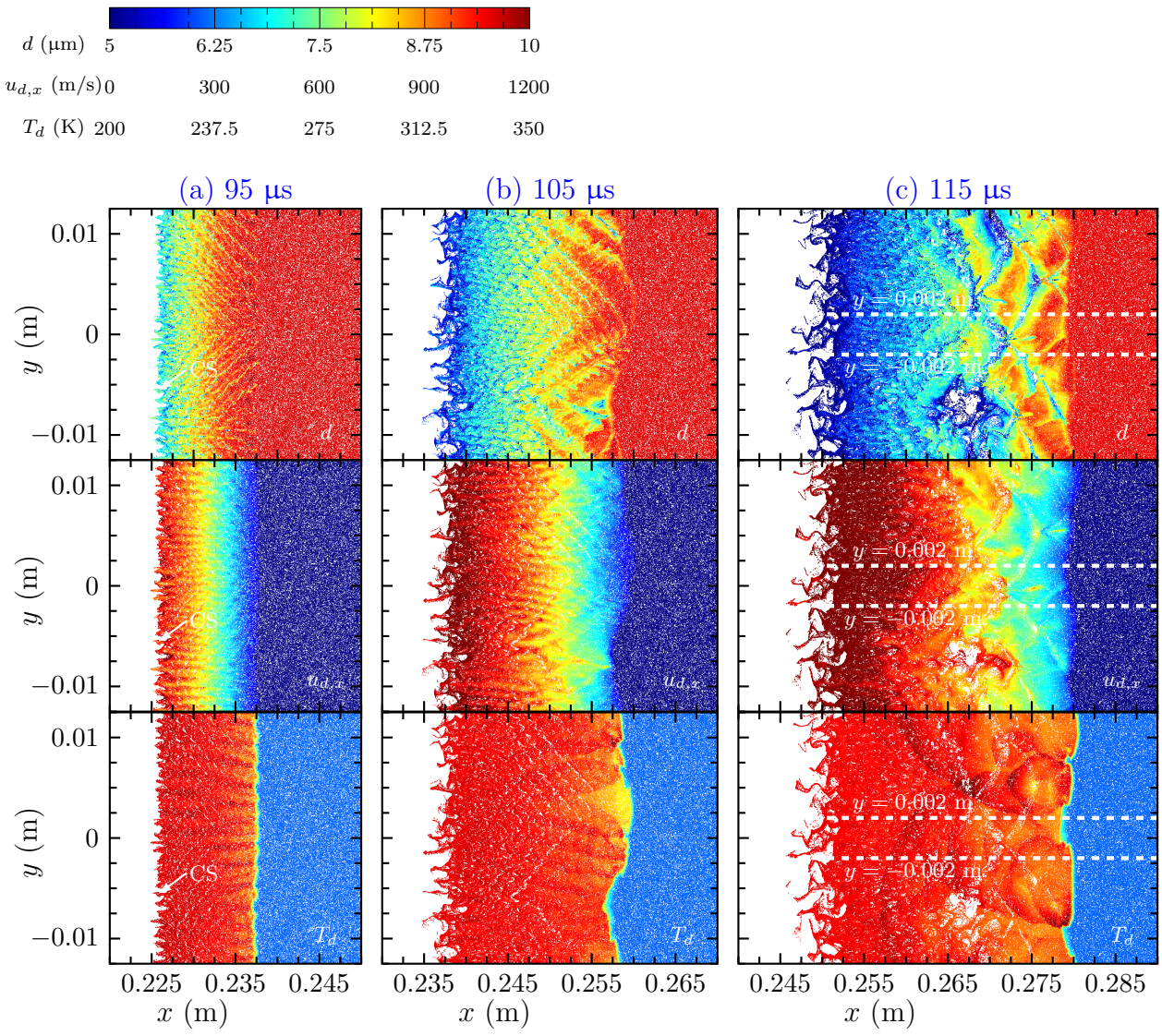


Figure 4.10: Spatial distributions of droplet diameter, d, x-direction velocity, $u_{d,x}$, and temperature, T_d, in droplet-laden NH_3-O_2 gas with initial droplet density number and diameter of $N_{d,0} = 1.5 \times 10^{12}$ /m^3 and $d_0 = 10$ μm at (a) 95, (b) 105, and (c) 115 μs. CS: contact surface.

d, high $u_{d,x}$ and T_d compared to the former. The variations of X_{NH_3}, u_x, and T see opposite trends against those of d, $u_{d,x}$, and T_d, respectively, from the DW to the CS. At 105 μs in Figures 4.9(b) and 4.10(b), the DW is partially decoupled and degenerates into the Detonative Spot (DS) at the tip of the RF due to prior perturbations from the ammonia droplets, see the contour of T. Its induction zone is locally thickened subject to RF-SF partial decoupling. At 115 μs in Figures 4.9(c) and 4.10(c), the DW is in a stable propagating state after reinitiation. The droplet-laden detonation front structure consists of the RF and the SF with alternate Mach Stems and Incident Waves connected by the Triple Points, denoted as MS, IW, and TP in the contour of T, respectively, as referred to by Xu *et al.* [124]. The differences of the gaseous and droplet thermo-chemical states behind the MS and the IW when $y = -0.002$ and 0.002 m, respectively, are quantitatively described later in Figure 4.11.

The distance between the DW and the CS gradually widens from 95, 105, to 115 μs. Meanwhile the differences between the pairs of gaseous and droplet quantities, *i.e.*, X_{NH_3}-d, u_x-$u_{d,x}$, and T-T_d, close to the CS where the inter-phase mass, momentum, and energy transfers are temporally accumulated gradually reduce. Specifically, within the time interval of 95-115 μs, the values of X_{NH_3} and T ahead of the CS increase from 0.013, 0.104, to 0.165 and decline from 2750, 2020, to 1680 K, respectively. The droplet x-direction velocity ahead of the CS is approximately relaxed to the carrier gas x-direction velocity of around 1250 m/s at 115 μs.

Figure 4.11 shows the spatial profiles of X_{NH_3}, d, u_x, $u_{d,x}$, T, and T_d along

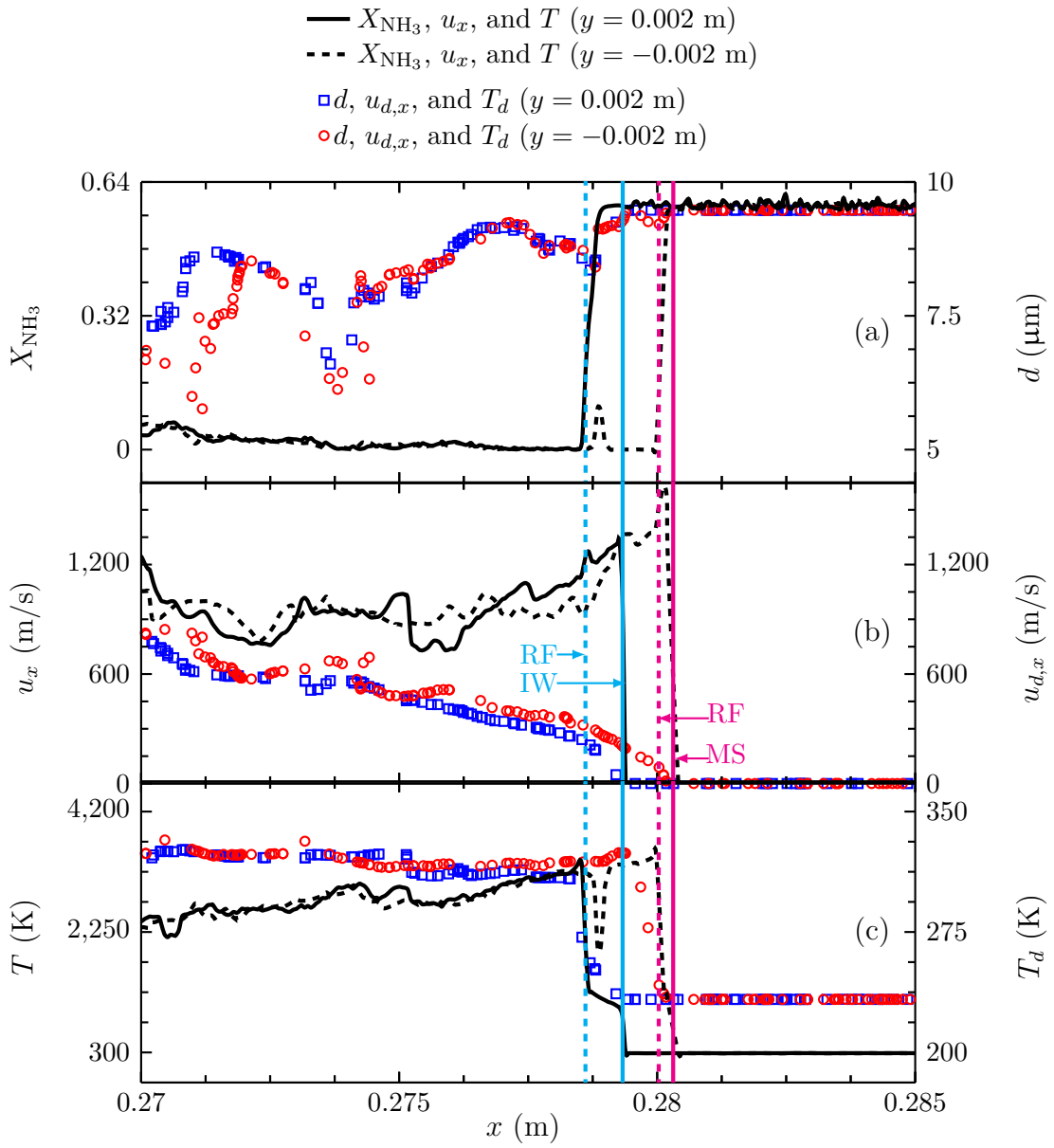


Figure 4.11: Spatial profiles of (a) gaseous ammonia volume fraction, X_{NH_3}, and droplet diameter, d, (b) gaseous x-direction velocity, u_x, and droplet x-direction velocity, $u_{d,x}$, and (c) gaseous temperature, T, and droplet temperature, T_d, along x-direction in droplet-laden NH_3-O_2 gas with initial droplet density number and diameter of $N_{d,0} = 1.5 \times 10^{12}$ /m^3 and $d_0 = 10$ μm at 115 μs. MS: the location of Mach stem; IW: the location of incident wave; RF: the location of reaction front.

x-direction for Case C_5 with $N_{d,0} = 1.5 \times 10^{12}$ /m^3 and $d_0 = 10$ μm at 115 μs. The y-direction locations at -0.002 and 0.002 m corresponding to the MS and the IW, respectively, see Figures 4.9(c) and 4.10(c), are selected. In Figure 4.11(a), the values of X_{NH_3} slightly fluctuate ahead of the SF as the ammonia droplets slowly evaporate, supported by $d \approx 9.5$ μm, in the intact carrier gas. The gaseous and droplet velocity and temperature fields ahead of the SF are nearly unperturbed. X_{NH_3} plunges to 0.003 across the RF behind both the MS and the IW. The maximum values of u_x occur right behind the MS and the IW with about 1630 and 1330 m/s, respectively. T sharply rises to about 1320 and 1280 K across the MS and the IW, respectively, and then to about 3580 and 3410 K across the corresponding RF. Therefore, the post-MS region experiences higher-intensity detonative combustion and thus droplet evaporative, accelerative, and heating effects than the post-IW region. The values of d are moderately smaller on the whole in the detonated carrier gas behind the MS than the IW. Those of T_d and $u_{d,x}$ are to the contrary.

4.6 Detonation extinction transient

Case C_6 with $N_{d,0} = 2.0 \times 10^{12}$ /m^3 and $d_0 = 10$ μm is selected to analyse the detonation extinction process. Its time sequences of schlieren (density gradient, *i.e.*, $|\nabla\rho|$) fields from 103 to 125 μs are depicted in Figure 4.12. Each frame shows a 0.025-m-long section along x-direction of the simulated domain which visualises instantaneous locations of the Detonative Front (DF). At 103 μs, the DW is locally quenched and highly wrinkled with two bumps, *i.e.*, DW_1 and DW_2, and

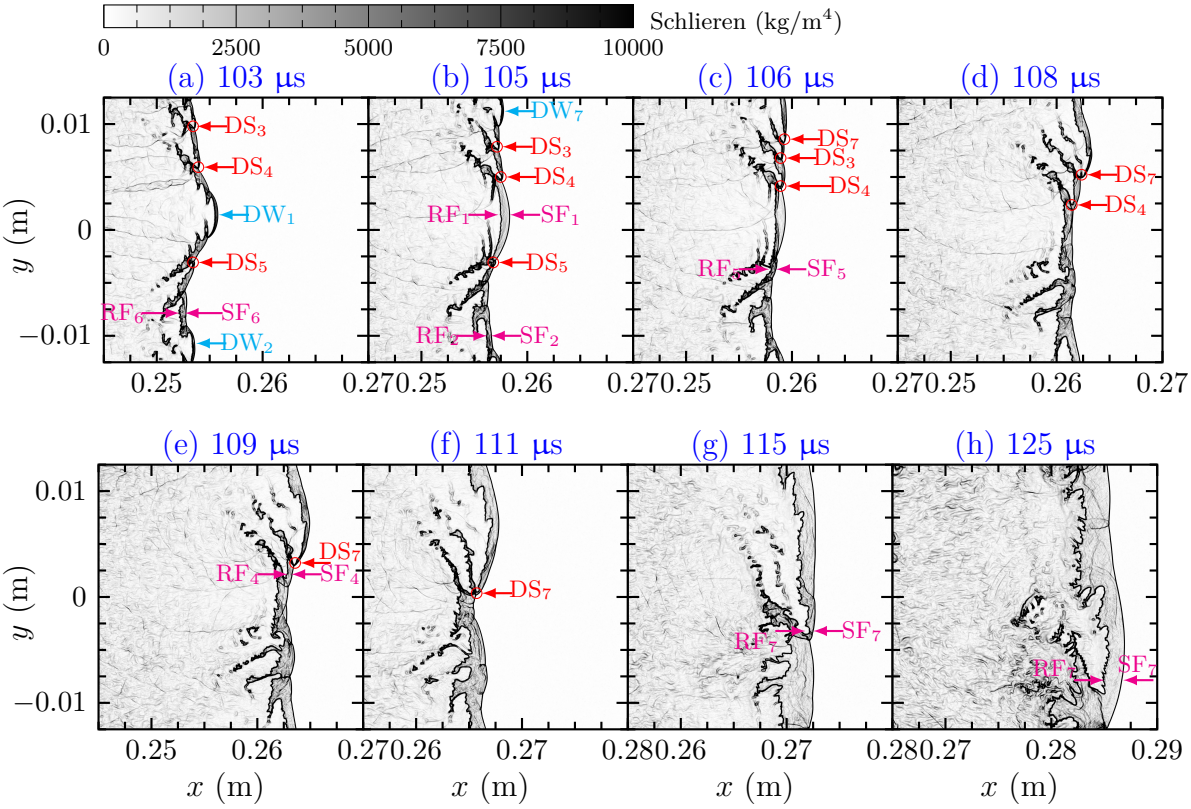


Figure 4.12: Evolution of schlieren fields during detonation extinction in droplet-laden premixed NH_3-O_2 gas with initial droplet density number and diameter of $N_{d,0} = 2.0 \times 10^{12}$ /m^3 and $d_0 = 10$ µm. DW: detonation wave; DS: detonative spot; SF: shock front; RF: reaction front.

four depressions, *i.e.*, DS_3-DS_5 and decoupled SF_6-RF_6. DW_1 and DW_2 correspond to Mach stems with coupled SF_1-RF_1 and SF_2-RF_2, respectively. As the ammonia droplets continue to strongly evaporate, accelerate, and absorb heat in the post-DW region, RF_1 and RF_2 see weakened chemical reactivity and reduced propagation speed. They gradually lag behind and decouple with SF_1 and SF_2, respectively, at 105 µs. Simultaneously, DW_7 occurs as DS_3 and DS_4 move

downwards. Note that DW_7 is the not-yet decoupled part of DW_2 that leaves and reenters the simulated domain respectively at the bottom and top ends. It experiences partial decoupling and degenerates into DS_7 at the tip of the RF due to the non-uniformity of inter-phase mass, momentum, and energy transfers along y-direction at 106 μs when the SF_5-RF_5 decoupling denotes the quenching of the DW's lower half. DS_7 overtakes DS_3 at 108 μs and decoupled SF_4-RF_4 from DS_4 at 111 μs in succession. It later collides with the SF from the decoupled lower half of the DW and decouples into SF_7 and RF_7 at 115 μs. At 125 μs, the DW ultimately quenches subject to the widened distance between SF_7 and RF_7. In general, the DW degenerates into the DS and then decouples into the SF and RF during the detonation extinction process. Note that Cases C_7-C_9 with the ultimate quenching of DW demonstrate similar extinction transients as Case C_6.

Figure 4.13 shows the spatial profiles of y-direction averages of gaseous HRR, $\dot{\omega}_T$, pressure, p, and nitric oxide volume fraction, X_{NO} along x-direction for Case C_6 with $N_{d,0} = 2.0 \times 10^{12}$ /m^3 and $d_0 = 10$ μm. The time interval of 95-130 μs covering the detonation extinction process is addressed. The location of the DF is roughly identified where p jumps from the initial pressure of $p_0 = 71$ kPa. The maximum values of $\dot{\omega}_T$, p, and X_{NO} behind the DF gradually level off. They roughly decline from 1.4×10^{13} J/m^3/s, 1.9 MPa, and 0.07 at 95 μs to 1×10^{12} J/m^3/s, 1.3 MPa, and 0.02 at 115 μs, respectively, accompanied by the increased exothermic region width with non-zero $\dot{\omega}_T$ due to the elevated wrinkling of the RF, see Figures 4.12(a)-(g). The comparatively low $\dot{\omega}_T$, p, and X_{NO} at 115 μs corresponding to the quenched DW, see Figures 4.12(g) and (h), are maintained onwards until 130 μs.

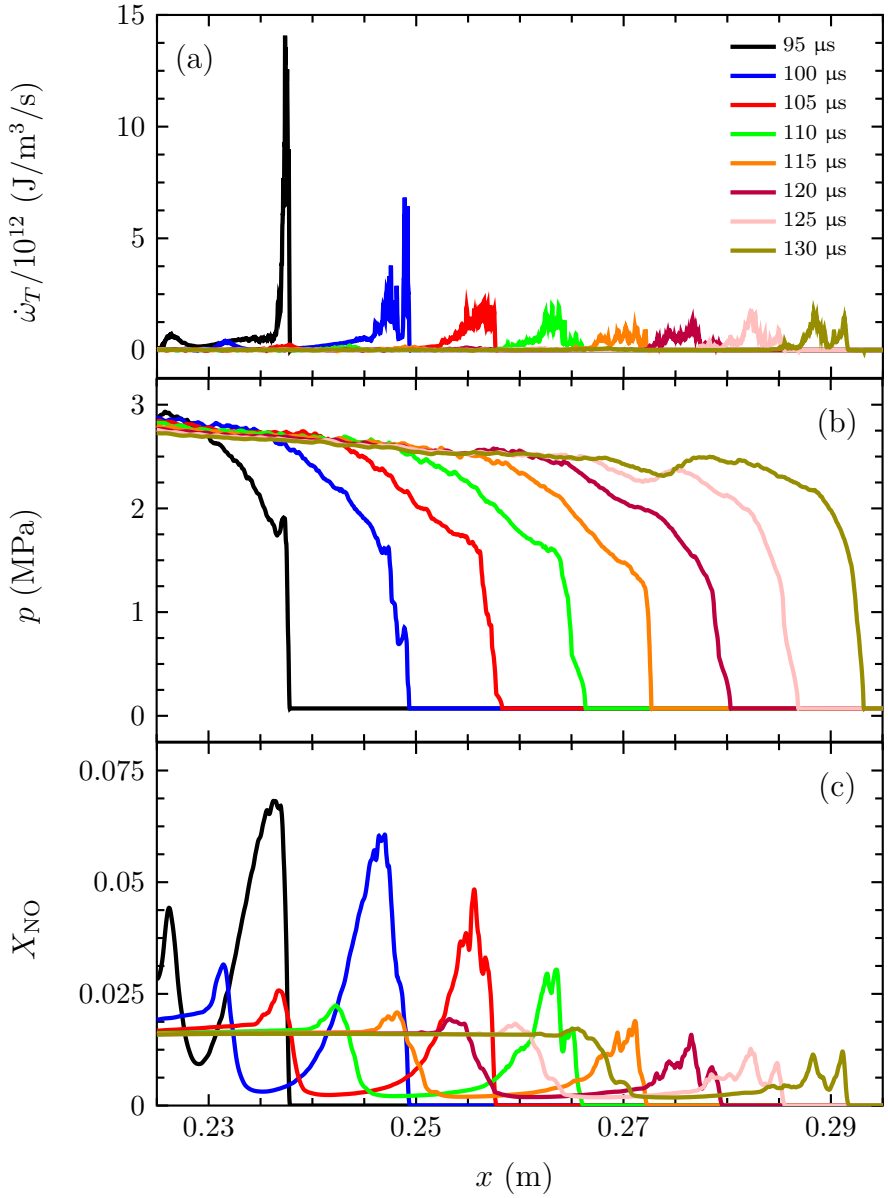


Figure 4.13: Spatial profiles of y-direction averaged (a) gaseous heat release rate, $\dot{\omega}_T$, (b) gaseous pressure, p, and (c) gaseous nitric oxide volume fraction, X_{NO}, in droplet-laden NH_3-O_2 gas with initial droplet density number and diameter of $N_{d,0} = 2.0 \times 10^{12}$ /m^3 and $d_0 = 10$ µm.

4.7 Summary

This work provides an understanding of detonative combustion in two-phase gas-droplet ammonia fuel. The characteristics of detonation propagation and extinction in ammonia droplet-laden premixed NH_3-O_2 gas are numerically investigated in a 2-D planar channel. The present simulations initiate slightly overdriven detonations in the droplet-free carrier gas of which the velocity and cell width demonstrate generally fair accuracy against the corresponding experimental measurements and analytical solutions. The detonation propagation/extinction scenarios with perturbations from the ammonia droplets, parameterised by the initial droplet number density of $N_{d,0} = 1.0 \times 10^{12}$, 1.5×10^{12}, or 2.0×10^{12} /m^3 and diameter of $d_0 = 5$, 10, or 15 μm, are predicted. The major findings are summarised on these points:

- The sustained propagation and ultimate quenching of detonation occur under lower and higher values of $N_{d,0}$ and d_0, respectively, and the detonation always quenches under $d_0 = 15$ μm.

- The detonation cell structure is considerably changed by the addition of ammonia droplets in the carrier gas and dependent on both d_0 and $N_{d,0}$ along with the detonation propagation/extinction behaviour.

- The droplet volume fraction, and the two-phase gas-droplet exchange rates of mass, momentum, and energy exhibit more nonlinear positive correlations with respect to d_0 than $N_{d,0}$.

- The ammonia droplets with $d_0 = 5$ and 15 μm under fixed $N_{d,0}$ are completely evaporated, accelerated, and heated most and least quickly, respectively, upon access into the post-detonation wave region.
- The droplet-laden detonative combustion and thus droplet evaporative, accelerative, and heating effects in the post-Mach stem region are higher-intensity than the post-incident wave region.
- The detonation wave degenerates into detonative spots which then decouple into shock and reaction fronts as quenches, and the gaseous pressure, heat release rate, and nitric oxide volume fraction peaks decline.

Chapter 5

3-D Supersonic Lifted Hydrogen Flame Study

5.1 Overview

This chapter reports the numerical results of 3-D large eddy simulations of a supersonic lifted hydrogen flame using the AHISsprayDetFoam solver developed in Chapter 2. The research background is provided in Section 5.2. The LES governing equations are detailed in Section 5.3. The experimental and computational configurations of the target supersonic lifted hydrogen flame are introduced in Section 5.4. The quality and reliability of the present simulations are evaluated via a posteriori analysis of mesh resolution in Section 5.5. The numerical results including flame and flow structures and statistics of scalars and velocity, from present simulations, affected by Lewis number/turbulent Schmidt

and Prandtl numbers, are discussed against corresponding experimental data in Sections 5.6 and 5.7, respectively. The summary of this chapter is provided in Section 5.8.

5.2 Background

In recent years, the rapid, ongoing development of hypersonic propulsion systems, such as scramjet engines, has sparked research interests in supersonic turbulent flames. Supersonic turbulent flames typically encounter strong shock-wave compression resulting in high-enthalpy gas environments. Experimental studies under such high-enthalpy conditions are challenging using ground-based combustion facilities [131]. Huge capital investments are required to tackle numerous practical difficulties in facility setup [73]. To reduce the cost, Computational Fluid Dynamics (CFD) can play a significantly important role during the design stage by providing fundamental understandings of supersonic turbulent flames, particularly, with the rapid advances in high-performance computing, Large Eddy Simulation (LES) is able to provide detailed spatiotemporal information of the structure and dynamics of the flow and flame in a computationally affordable way [74]. Improving the numerical accuracy of LES, *e.g.*, in the modelling of supersonic turbulent flames, is one of the current interests of industry and government organizations [19].

The experiment of a supersonic lifted hydrogen flame by Cheng *et al.* [140], termed as Cheng supersonic flame hereafter, provides a reliable set of data for flow

Table 5.1: Summary of LES studies on Cheng supersonic flame. QLC: Quasi-Laminar Chemistry; PDF: Probability Density Function; PaSR: Partially Stirred Reactor; PSR: Perfectly Stirred Reactor; MMC: Multiple Mapping Conditioning.

Reference	Computational domain	Mesh resolution	Chemistry	Combustion model	Main focus
Dauptain *et al.* (2005) [132]	Hemisphere, $70D_f$ in radius	0.81 million cells, 25 to 30 nodes in the diameter of both fuel an oxidizer jets	4 species, 2 reactions	QLC	Application of LES
Wang *et al.* (2011) [133]	Cylindrical, $43D_f$ in length and $30D_f$ in radius	Main mesh divided into 13 blocks, each of $31 \times 31 \times 161$ nodes	9 species, 19 reactions	PDF	Development of a hybrid LES/assumed sub-grid PDF model
Boivin *et al.* (2012) [134]	Hemisphere, $10{,}000D_f$ in radius	6.6 million cells, minimum volume of 8×10^{-13} m^3	6 species, 3 reactions	QLC	Validation of a reduced chemistry and analysis of flame stabilisation
Moule *et al.* (2014) [135]	Cylindrical, $60D_f$ in length and $20D_f$ in radius	31 million cells, minimum size of 0.1-0.2 mm	9 species, 19 reactions	Unsteady PaSR	Capability of unsteady PaSR closure and analysis of flame structure and associated stabilisation zone
Ribert *et al.* (2014) [136]	Cylindrical, $70D_f$ in length	Three meshes of 2, 30 and 113 million cells	6 species, 3 reactions	QLC	Effect of shear layer prediction on flame stabilisation position
Bouheraoua *et al.* (2017) [137]	Cylindrical, $70D_f$ in length and $30D_f$ in radius	Three meshes of 4, 32 and 268 million cells, minimum sizes of 0.24, 0.12 and 0.06 mm	6 species, 3 reactions	QLC	Mechanism driving flame stabilisation
Paixão de Almeida *et al.* (2019) [138]	Cylindrical, $70D_f$ in length and $30D_f$ in radius	Two meshes of 0.2 and 2 million cells	9 species, 19 reactions	PDF	Performance of a joint scalar-enthalpy PDF model and a joint velocity-scalar-energy PDF model
Chen *et al.* (2019) [139]	Cylindrical, 240 mm in length and 50 mm in radius	Three meshes of 10, 20, 30 million cells	11 species, 23 reactions	PaSR	Influence of compressibility on reaction rates and sub-grid stress
Zhang *et al.* (2020) [11]	Cylindrical, $100D_f$ in length and $30D_f$ in radius	26 million cells, minimum size of 0.16 mm	9 species, 19 reactions	QLC	Accuracy of LES with a high-fidelity numerical solver
Zhao *et al.* (2021) [73]	Cylindrical, $100D_f$ in length and $30D_f$ in radius	26 million cells, minimum size of 0.16 mm	9 species, 19 reactions	PSR	Assessment of LES-PSR model including viscous heating and compressibility effects
Huang *et al.* (2022) [74]	Cylindrical, $70D_f$ in length and $30D_f$ in radius	12.2 million cells, minimum size of 0.05/0.12 mm in x-/r-directions	9 species, 19 reactions	MMC	Examination of LES-MMC model including pressure work and viscous heating

*The inside diameter of fuel jet, D_f, is 2.36 mm.

dynamics, mixing, temperature, and species concentrations. This data set has been widely used as a reference in exploring the accuracy of LES studies on supersonic turbulent flames. Table 5.1 summarises past LES studies on Cheng supersonic flame. Among these investigations, Dauptain *et al.* [132] took the lead in applying LES in the modelling of Cheng supersonic flame. Ribert *et al.* [136] and Bouheraoua *et al.* [137] studied the mechanism driving the flame stabilisation. Chen *et al.* [139] explored the influence of compressibility on reaction rates and sub-grid stress. In terms of improving the LES accuracy, Boivin *et al.* [134] and Zhang *et al.* [11] validated a reduced chemical mechanism and a high-fidelity numerical solver, respectively. Other investigations in Refs. [73, 74, 133, 135, 138] have been focused on improving the Sub-Grid Scale (SGS) turbulent combustion model for capturing unresolved turbulence-chemistry interactions, instead of other unclosed terms in the filtered transport equations of LES, including mass and thermal diffusion fluxes, $\bar{\mathbf{J}}_i$ and $\bar{\mathbf{J}}_h$. These two terms are typically modelled as

$$\bar{\mathbf{J}}_i = -\bar{\rho}(D_i + D_{sgs})\nabla\widetilde{Y}_i, \tag{5.1}$$

$$\bar{\mathbf{J}}_h = -\bar{\rho}(\alpha + \alpha_{sgs})\nabla\tilde{h}_s, \tag{5.2}$$

where $\bar{\rho}$ is the filtered density, $[\tilde{}]$ indicates Favre-filtered quantities, D_i and $\widetilde{Y}_i$ refer to the mass diffusivity and fraction of the i-th species, α is the thermal diffusivity, and $\tilde{h}_s$ is the sensible enthalpy. D_{sgs} and α_{sgs} are the SGS mass and thermal diffusivities which read

$$D_{sgs} = \frac{\mu_{sgs}}{\bar{\rho}Sc_t}, \tag{5.3}$$

$$\alpha_{sgs} = \frac{\mu_{sgs}}{\bar{\rho} Pr_t}. \tag{5.4}$$

where μ_{sgs} is the SGS dynamic viscosity, and Sc_t and Pr_t are turbulent Schmidt and Prandtl numbers, respectively.

Various approaches have been used for calculating the mass and thermal diffusivities on both filtered scale (D_i and α) and SGS (D_{sgs} and α_{sgs}) in the LES studies on Cheng supersonic flame (Table 5.1). For example, Chen *et al.* [139] used the mixture-averaged diffusion model to calculate D_i and α, together with the molecular dynamic viscosity, μ. The mixture-averaged diffusion model assumes that D_i is computed from binary diffusivities between the i-th species and the rest of species in the mixture, and that α and μ of a mixture are evaluated using an averaging formula combining the corresponding values from all individual pure species. In Refs. [11, 73, 74], μ is predicted using Sutherland's law [13], α is renewed from the thermal conductivity, λ is calculated using the Eucken approximation [14] with μ involved, D_i is computed via a computationally more efficient assumption of unity Lewis number. The Lewis number of the i-th species, Le_i, is defined as the ratio of α and D_i. The mass diffusivities of all species are equal to α in the unity-Lewis number assumption. For the computations of D_{sgs} and α_{sgs}, a wide span of Sc_t and Pr_t values has been used in the literature, *e.g.*, unity in Refs. [11, 137, 138] and sub-unity in Refs. [73, 74]. The optimal choice of Lewis, turbulent Schmidt and Prandtl numbers that balances numerical accuracy and computational efficiency hence has not been well understood for the LES of the Cheng supersonic flame, and more broadly, any supersonic turbulent flame.

A particular modeling challenge for the Cheng supersonic flame is associated with the light species H_2 and H. The mass diffusivities of H_2 and H are much higher than those of relatively heavy species, *e.g.*, O_2 and H_2O_2, referring to the differential diffusion effect. The mass diffusivities of H_2 and H are also higher than the thermal diffusivity, resulting in the preferential diffusion effect [141]. The Lewis numbers of individual species in a mixture quantitatively characterise differential and preferential diffusion effects. As turbulent hydrogen flames involve profound differential and preferential diffusion effects, extensive numerical studies have been focused on the impacts of Lewis number. For example, Lee *et al.* [142] performed Direct Numerical Simulation (DNS) in highly turbulent lean hydrogen-air flames. The turbulent burning velocity, U_T, was observed to significantly increase with the incorporation of species-specific Lewis numbers but be minorly influenced by the preferential diffusion effect. In the LES, the mass diffusivities on the filtered scale can become comparable to the SGS turbulent viscosity, *i.e.*, $\mu_{sgs}/\bar{\rho}$, especially in regions close to the flame front when the LES computational grid is fine [143]. The use of non-equal Lewis numbers for different species has also been found critical in the modelling of localised scalar mixing, autoignition, extinction, and reignition [144–147]. Previous LES studies have unveiled the necessity of accounting for the differential diffusion effect in the modelling of a H_2/N_2 lifted turbulent flame [143] and a jet-in-hot-coflow CH_4/H_2 flame [148]. The LES study of a lean-premixed H_2/air low-swirl lifted flame showed improved predictions on velocities and species distributions near the flame front by considering preferential diffusion effects [149]. While these LES studies

mainly focused on subsonic turbulent hydrogen flames, this work aims to assess the importance of incorporating differential and preferential effects, *i.e.*, the impacts of Lewis number, in depicting supersonic turbulent flame and flow structures with LES. The LES results of Cheng supersonic flame using the mixture-averaged diffusion model are compared to those using the unity-Lewis number assumption. The mixture-averaged diffusion model employs both differential and preferential diffusion effects via species-specific Lewis numbers. It is relatively less computationally time-consuming but has been proven to show comparable accuracy against the most precise and sophisticated multi-component diffusion model in the modelling of both turbulent and laminar flames [18, 19].

The impacts of Lewis number on the LES of Cheng supersonic flame are embodied in the calculations of mass and thermal diffusivities on the filtered scale. This work also aims to optimise the LES of Cheng supersonic flame regarding the calculations of SGS mass and thermal diffusivities, *i.e.*, D_{sgs} and α_{sgs}. Based on Eqs. (5.3) and (5.4), D_{sgs} and α_{sgs} are determined by the turbulent Schmidt and Prandtl numbers, *i.e.*, Sc_t and Pr_t, respectively, with the SGS dynamic viscosity, *i.e.*, μ_{sgs}, involved. The values of Sc_t and Pr_t characterise turbulent scalar transfers of species mass fractions and energy from turbulent momentum transfer, respectively. They can impose influences on numerical predictions of turbulence/chemistry interactions and thus flame and flow structures. The impacts of Sc_t and Pr_t have been extensively studied in Reynolds-Averaged Navier-Stokes (RANS) simulations of supersonic turbulent flames while less in LES. Eklund and Baurle [150] concluded that a low Sc_t can numerically result in

unstart phenomena in an ethylene-fueled scramjet combustor, while high Sc_t can lead to flame blowout using RANS simulations. Xiao *et al.* [151] developed a turbulence model in RANS simulations with variable Sc_t and Pr_t as part of the solution and applied it into scramjet non-reacting and H_2/air reacting flows. Numerical results with variable Sc_t and Pr_t show better agreement with corresponding experimental data. Zheng and Yan [152] performed sensitivity analysis of Sc_t and Pr_t between 0.5 and 0.9 using RANS simulations of two supersonic hydrogen flames: Burrows-Kurkov case [153] and DLR case [154], where ignition locations vary with the two parameters. In the LES context, Ingenito and Bruno [155] performed the LES of a supersonic H_2/air combustor with three different Sc_t of 0.4, 0.6 and 0.7. The flame was observed to oscillate with $Sc_t = 0.7$ but be stable with $Sc_t = 0.4$ and 0.6, and it becomes less stratified and no longer confined to the H_2/air interface as Sc_t decreases. A variable Sc_t was also implemented into a new SGS turbulence model, and this parameter turned out to vary from 0.4 to 1.0 and be particularly low where combustion occurs in the LES study. While LES studies on the impacts of Sc_t and Pr_t on supersonic turbulent flames are still scarce, those of Cheng supersonic flame with different combinations of the two parameters are performed in this work. Based on the aforementioned RANS and LES studies, the values of Sc_t and Pr_t equal to 0.5 or 1.0 are applied.

The objectives of this work are two-fold. The first is the impacts of Lewis number and the other is those of turbulent Schmidt and Prandtl numbers on the LES of supersonic turbulent flames using the AHIsprayDetFoam solver.

5.3 LES governing equations

The filtered fully compressible Navier-Stokes equations, *i.e.*, continuity, momentum, species mass fractions, and sensible enthalpy, coupled with the ideal gas equation of state, are solved in this work. They respectively read

$$\frac{\partial \bar{\rho}}{\partial t} + \nabla \cdot (\bar{\rho}\tilde{\mathbf{u}}) = 0, \tag{5.5}$$

$$\frac{\partial (\bar{\rho}\tilde{\mathbf{u}})}{\partial t} + \nabla \cdot [\tilde{\mathbf{u}}(\bar{\rho}\tilde{\mathbf{u}})] + \nabla \bar{p} - \nabla \cdot \bar{\boldsymbol{\tau}} - \nabla \cdot \boldsymbol{\tau}_{sgs} = 0, \tag{5.6}$$

$$\frac{\partial \left(\bar{\rho}\widetilde{Y}_i\right)}{\partial t} + \nabla \cdot \left[\tilde{\mathbf{u}}\left(\bar{\rho}\widetilde{Y}_i\right)\right] + \nabla \cdot \bar{\mathbf{J}}_i = \widetilde{\dot{\omega}}_i, (i = 1, 2, \cdots, N-1), \tag{5.7}$$

$$\frac{\partial (\bar{\rho}\tilde{h}_s)}{\partial t} + \nabla \cdot [\tilde{\mathbf{u}}(\bar{\rho}\tilde{h}_s)] - \frac{D\bar{p}}{Dt} + \nabla \cdot \bar{\mathbf{J}}_h = \widetilde{\dot{\omega}}_T, \tag{5.8}$$

$$\bar{\rho} = \bar{p} \Big/ \left(R_u \widetilde{T} \sum_i \frac{\widetilde{Y}_i}{W_i}\right). \tag{5.9}$$

Here, the mass and thermal diffusion fluxes, *i.e.*, $\bar{\mathbf{J}}_i$ in Eq. (5.7) and $\bar{\mathbf{J}}_h$ in Eq. (5.8), have been given in Eqs. (5.1)-(5.4). The filtered density, *i.e.*, $\bar{\rho}$, the indicator of Favre-filtered quantities, *i.e.*, $\tilde{[\,]}$, the mass fraction of the i-th species, *i.e.*, $\widetilde{Y}_i$, and the sensible enthalpy, *i.e.*, $\tilde{h}_s$, have been referred to in Eqs. (5.1) and (5.2). t is the time; $\bar{p}$ is the filtered pressure; $\tilde{\mathbf{u}}$ and $\widetilde{T}$ state for the velocity vector and temperature, respectively. $\bar{\boldsymbol{\tau}}$ and $\boldsymbol{\tau}_{sgs}$ in Eq. (5.6) denote the filtered and SGS viscous stress tensors, respectively computed by

$$\bar{\boldsymbol{\tau}} = \mu \left[\nabla\tilde{\mathbf{u}} + (\nabla\tilde{\mathbf{u}})^{\mathrm{T}} - \frac{2}{3}(\nabla \cdot \tilde{\mathbf{u}})\mathbf{I}\right], \tag{5.10}$$

$$\boldsymbol{\tau}_{sgs} = \mu_{sgs} \left[\nabla\tilde{\mathbf{u}} + (\nabla\tilde{\mathbf{u}})^{\mathrm{T}} - \frac{2}{3}(\nabla \cdot \tilde{\mathbf{u}})\mathbf{I}\right], \tag{5.11}$$

where $\mathbf{I}$ is the identity matrix and the superscript T indicates matrix transposition. The molecular dynamic viscosity, *i.e.*, μ in Eq. (5.10), is calculated together with the mass and thermal diffusivities, *i.e.*, D_i in Eq. (5.1) and α in Eq. (5.2), using either the mixture-averaged diffusion model with a mixture-averaged formula [16] or a combination of the Sutherland's law [13], Eucken approximation [14], and unity-Lewis number assumption. The SGS dynamic viscosity, *i.e.*, μ_{sgs} in Eq. (5.11), is estimated using the constant Smagorinsky turbulence model [156]. The SGS mass and thermal diffusivities, D_{sgs} in Eq. (5.3) and α_{sgs} in Eq. (5.4), are accordingly determined by the turbulent Schmidt and Prandtl numbers, *i.e.*, Sc_t and Pr_t, as constants of 0.5 or 1.0.

In Eq. (5.7), $\widetilde{\dot{\omega}}_i$ refers to the chemical net production rate of the i-th species, and N denotes the number of species. Eq. (5.7) is solved for all the species except the N-th species, an "inert species", *e.g.*, nitrogen (N_2) here, whose mass fraction is computed by subtracting the mass fractions of all other species from unity. $\widetilde{\dot{\omega}}_T$ in Eq. (5.8) is the heat release rate from chemical reactions. $\widetilde{\dot{\omega}}_i$ and $\widetilde{\dot{\omega}}_T$ are solved using the Quasi-Laminar Chemistry (QLC) closure excluding SGS fluctuations, following Refs. [11, 132, 134, 136, 137] summarised in Table 5.1. The adequacy of the QLC closure for chemistry integration in the present LES studies is justified in Section 5.5 later. Radiative heat transfer, Soret and Dufour effects play secondary roles and are thus not included in Eqs. (5.7) and (5.8). Note that the real gas effect on supersonic turbulent flames is also not referred to in this work. In Eq. (5.9), R_u is the universal gas constant, and W_i is the mole weight of the i-th species.

5.4 Experimental and computational configurations

Figure 5.1(a) shows the schematic of Cheng supersonic flame burner [140]. A sonic round jet of hydrogen (H_2) is injected as the fuel from a central pipe with a diameter, D_f, of 2.36 mm, surrounded by an annular jet of hot, vitiated air stream at Mach 2 as the coflow. The coflow is generated by an upstream lean combustor where hydrogen burns with air with excess oxygen (O_2). The inner and outer diameters of the annular coflow jet are $D_i = 3.81$ mm and $D_o = 17.78$ mm, respectively. The flow conditions of fuel and coflow jets at the Cheng supersonic flame burner exit are given in Table 5.2. The lift-off height of Cheng supersonic flame is about $25D_f$, see Figure 5.1(b) which shows an experimental photograph of flame luminosity [140]. The experimental measurements in Refs. [140, 157] reported radial profiles of mean axial velocity, u_x, temperature, T, mixture fraction, Z, and some species mole fractions, including X_{O_2}, X_{H_2O}, X_{N_2}, X_{H_2} and X_{OH}, at all or parts of seven downstream distances, *i.e.*, $x/D_f = 0.85$, 10.8, 21.5, 32.3, 43.1, 64.7 and 86.1. They are referred to in comparison with subsequent LES studies in this work. Instantaneous scatter plots of T, X_{O_2}, X_{H_2O}, X_{N_2}, X_{H_2} and X_{OH} versus Z at several locations are also available in Ref. [140] but not referred to in this work.

Figure 5.1(c) shows the schematic of the cylindrical computational domain for the LES of Cheng supersonic flame on the central plane of symmetry [74]. Above the coordinate origin, O, located at the center of the fuel jet at the burner exit, it has a length of $70D_f$ along the streamwise x-direction, with a radius of $30D_f$ along the radial r-direction. It also extends $1.5D_f$ upstream into the fuel and coflow

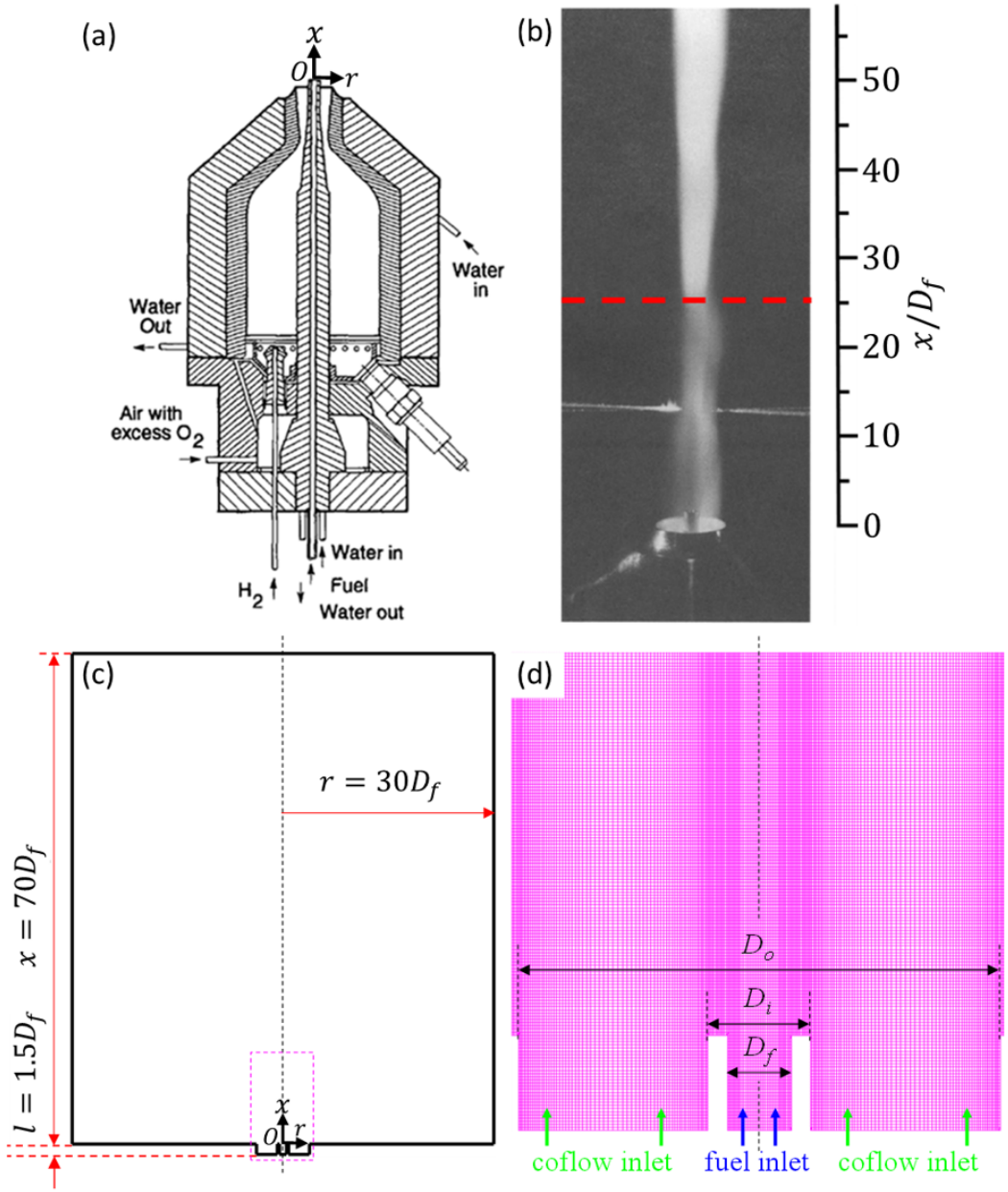


Figure 5.1: (a) Schematic of Cheng supersonic flame burner [140], (b) experimental visual long exposure photograph [140], (c) 2-D schematic of cylindrical computational domain [74], and (d) local enlarged mesh around fuel and coflow inlets [74]. Reproduced with permission from Combust. Flame. 99, 157–173 (1994) and Combust. Flame. 238, 111756 (2022). Copyright Elsevier Inc.

Table 5.2: Flow conditions of fuel and coflow jets at the exit of Cheng supersonic flame burner. p is pressure; T is temperature; Re is Reynolds number; Ma is Mach number; X_{O_2}, X_{H_2O}, X_{N_2} and X_{H_2} are species mole fractions.

	p (kPa)	T (K)	Re	Ma	X_{O_2}	X_{H_2O}	X_{N_2}	X_{H_2}
Fuel	112	545	15,600	1.0	0.0	0.0	0.0	1.0
Coflow	107	1250	101,100	2.0	0.201	0.255	0.544	0.0

Table 5.3: Boundary conditions of cylindrical computational domain. p is pressure; T is temperature; $\mathbf{u}$ is velocity; O_2, H_2O, N_2 and H_2 are species.

	p	T	$\mathbf{u}$	O_2, H_2O, N_2 and H_2
Fuel and coflow inlets	fixedValue	fixedValue	decayingTurbulenceInflowGenerator	fixedValue
Fuel and coflow pipes	zeroGradient	zeroGradient	slip	zeroGradient
Lateral and outlet boundaries	waveTransmissive	zeroGradient	zeroGradient	zeroGradient
Annular plane at $x = 0$	zeroGradient	zeroGradient	fixedValue	zeroGradient

pipes. The mesh consists of 12,175,200 hexahedral cells with radially localised refinement around the fuel and coflow inlets and their shear layers, marked with a dashed box where the distribution of cells is enlarged and demonstrated in Figure 5.1(d) [74]. The minimum cell sizes along x- and r-directions are 118 and 50 μm, respectively. Note that the Kolmogorov and integral length scales of Cheng supersonic flame estimated experimentally fall in ranges of 8-35 μm and 3,400-7,400 μm [140], respectively.

The boundary conditions of the cylindrical computational domain are listed in Table 5.3. The "decayingTurbulenceInflowGenerator" boundary condition [158,

159] which specifies a synthetic inflow turbulence is applied for velocity fields at the fuel and coflow inlets. In this manner, the representation of the velocity field reads the sum of vortons induced by a collection of randomly placed spots; the fluctuations of velocity distribution inside each spot possess prescribed statistical properties, including integral length scale and symmetric Reynolds-stress tensor. The integral length scale is approximated from hydraulic diameters of fuel and coflow pipes, *i.e.*, D_f and $[D_o - D_i]$, respectively. The symmetric Reynolds-stress tensor is expressed by considering both the fuel and coflow inlets as round jet flows [160]. The correlations between its six components of normal and shear stresses are given following the method of Masri *et al.* [161]. The normal and shear stresses are related to the axial velocity fluctuation and thus the mean velocity along x-direction and turbulent intensities at the jet centre and circumference based on Refs. [158, 159]. The mean velocities of fuel and coflow jets along x-direction, U_f and U_c, are 1,780 and 1,420 m/s, respectively. For the round fuel jet, the turbulent intensities are assumed to be $I_{f,cen} = 5\%$ and $I_{f,cir} = 18\%$ at its center and circumference; for the annular coflow jet, its central circumference with a diameter of $(D_o + D_i)/2$ has the lowest turbulent intensity, $I_{c,cen}$, of 5%, while the highest turbulent intensities, $I_{c,cir}$, are assumed to be 22% at both its inner and outer circumferences. The "fixedValue" boundary condition is applied for other variables of fuel and coflow inlets, whose magnitudes are set in consistency with the experimental flow conditions at the burner exit, given in Table 5.2. The fuel and coflow pipes are all slip and adiabatic walls with "slip" and "zeroGradient" boundary conditions specified for velocity and other variables, respectively. The computational domain is open to the

Table 5.4: Parametric LES of Cheng supersonic flame. Le_i is Lewis number of i-th species; Sc_t is turbulent Schmidt number; Pr_t is turbulent Prandtl number.

Case ID	Le_i	Sc_t	Pr_t
C_0	Species-specific	1.0	1.0
C_1	Unity	1.0	1.0
C_2	Species-specific	0.5	1.0
C_3	Species-specific	1.0	0.5
C_4	Species-specific	0.5	0.5

atmosphere (1 atm, 298 K) at lateral and outlet boundaries, which are assumed to be non-reflective with "waveTransmissive" and "zeroGradient" boundary conditions specified for pressure and other variables, respectively. It is closed at the annular plane at $x = 0$ with inner and outer diameters as D_o and $30D_f$, respectively, where velocity is set as "fixedValue" of zero and other variables with the "zeroGradient" boundary condition.

The parametric LES studies on Cheng supersonic flame, summarised in Table 5.4, are performed on the University of Oxford Advanced Research Computing (ARC) facility in this work. A detailed chemical mechanism for hydrogen combustion with 9 species and 19 reactions [162] is used. The Courant-Friedrich-Lewy (CFL) number is set as 0.3, and accordingly, the physical time step, Δt, is approximately 4×10^{-9} s. The computation on 336 processors for each LES takes about 15,961 CPU-hours per characteristic flow-through time which is the ratio of computational domain length, *i.e.*, $70D_f$, and coflow mean velocity along x-direction, *i.e.*, U_c. Each LES collects the statistics on average over 0.25 ms as in Ref. [137], longer than two characteristic flow-through times, after a

statistically transient flow period of 0.5 ms.

5.5 Mesh resolution analysis

The quality and reliability of the present LES studies are evaluated via a *posteriori* analysis of mesh resolution in this section. Two criteria, *i.e.*, μ_{sgs}/μ and τ_{sgs}/τ_c, are examined. μ_{sgs}/μ is the ratio between SGS and molecular dynamic viscosities, functioning as a turbulence resolution indicator. Its values for each cell essentially below 4 suggest a well-resolved LES. τ_{sgs}/τ_c, *i.e.*, Da_{sgs} in Refs. [11, 137, 163, 164], is the ratio between SGS and chemical timescales. Its sub-unity values for each cell justify the adequacy of the QLC closure for chemistry integration excluding SGS fluctuations. τ_{sgs} and τ_c are estimated using the method in Refs. [11, 137], respectively read

$$\tau_{sgs} = \frac{C_s^2 \bar{\rho} \Delta^2}{\mu_{sgs}}, \tag{5.12}$$

$$\tau_c = \frac{\bar{\rho}}{\widetilde{\dot{\omega}}_{\mathrm{H_2O}}}, \tag{5.13}$$

where C_s is a constant of 0.15 in the Smagorinsky turbulence model [156]. Δ is the LES filter width, related to the cell volume of mesh, V_{cell}, by $\Delta = V_{\mathrm{cell}}^{1/3}$. $\widetilde{\dot{\omega}}_{\mathrm{H_2O}}$ states for the chemical net production rate of water (H_2O); consequently, the computations of τ_c and thus τ_{sgs}/τ_c are limited to chemically reacting flow fields, *i.e.*, where the heat release rate ($\widetilde{\dot{\omega}}_T$) is over 10^9 J/m^3/s according to Refs. [11, 137].

Figures 5.2(a) and (b) show instantaneous scatter plots of μ_{sgs}/μ and τ_{sgs}/τ_c against heat release rate, *i.e.*, $\widetilde{\dot{\omega}}_T$, coloured by temperature, *i.e.*, T, on the symmetry

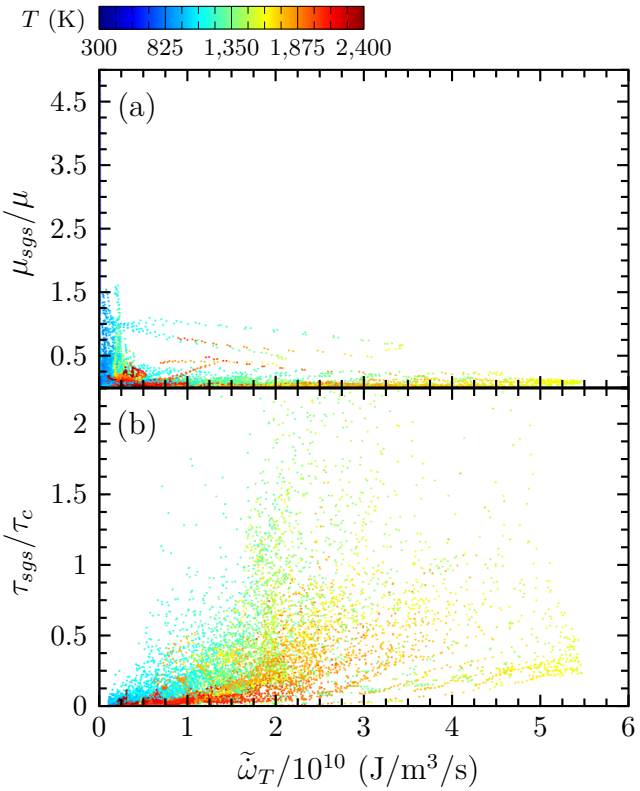


Figure 5.2: Instantaneous scatter plots of the ratios between (a) SGS and molecular dynamic viscosities and (b) SGS and chemical timescales against heat release rate coloured by temperature on the symmetry plane in the central region of $70D_f \times 5D_f \times 2\pi$. Case ID: C_0.

plane in the central region of $70D_f \times 5D_f \times 2\pi$ where most fuel-oxidiser mixing and combustion proceed for Case C_0. Most scatters see decent values of $\mu_{sgs}/\mu < 4$ and $\tau_{sgs}/\tau_c < 1$ over the whole range of $\widetilde{\omega}_T$, especially at pronounced rises of T. Only a few scatters with $\mu_{sgs}/\mu > 1.5$ correspond to cold locations with almost zero $\widetilde{\omega}_T$. Fairly good values of μ_{sgs}/μ between 1 and 1.5 are observed at low $\widetilde{\omega}_T$ and T. For values of $\widetilde{\omega}_T$ over 2.5×10^9 J/m^3/s and T over 1,350 K, μ_{sgs}/μ is predominantly

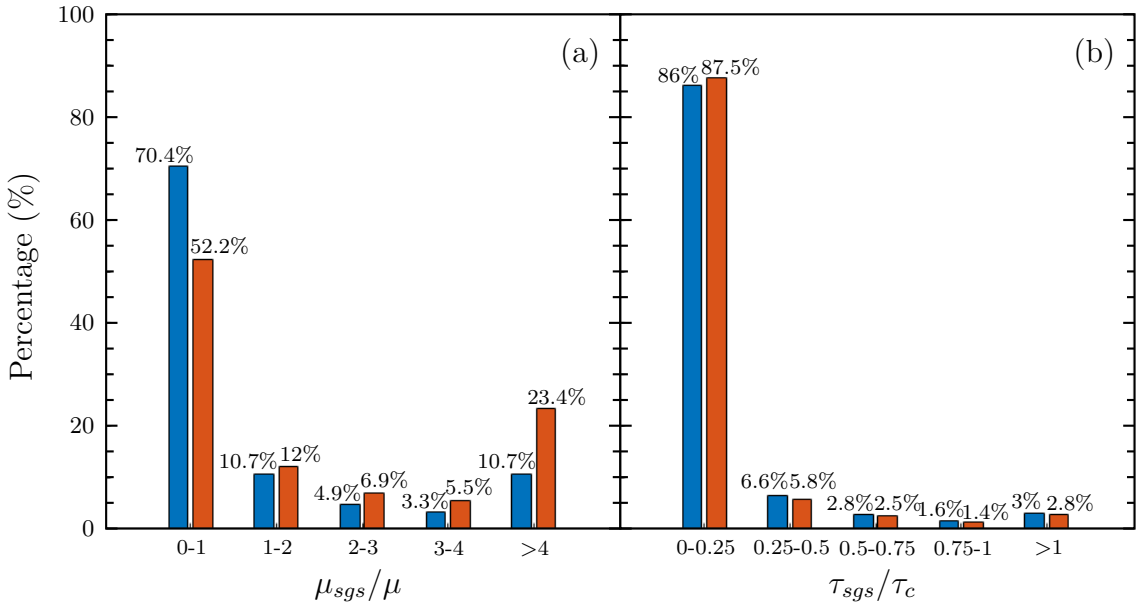


Figure 5.3: Instantaneous percentages of the ratios between (a) SGS and molecular dynamic viscosities and (b) SGS and chemical timescales in several ranges in the central region of $70D_f \times 5D_f \times 2\pi$ (blue bars) and over the whole computational domain (orange bars). Case ID: C_0.

lower than 1. For τ_{sgs}/τ_c, minor scatters with τ_{sgs}/τ_c over 1 are located in regions with middle values of $\widetilde{\dot{\omega}}_T$ between 1.5×10^9 and 4.5×10^9 J/m^3/s. These results indicate the well-resolved reacting part of the central region and the fair application of the QLC closure in the present LES studies.

Instantaneous percentages of the two criteria in the central region of $70D_f \times 5D_f \times 2\pi$ and over the whole computational domain located in several ranges are presented in Figures 5.3(a) and (b) to quantitatively describe the LES mesh resolution sufficiency. Cells with imperfectly resolved turbulence where values of μ_{sgs}/μ are over 4 account for 10.7% and 23.4%, respectively. The

percentages of cells with inappropriate use of QLC closure where values of τ_{sgs}/τ_c are over 1 are only 3% and 2.8%, respectively. In general, the part of the central region with good mesh quality in the present LES studies dominates. Its 70.4% is extremely well resolved, and the QLC closure is highly applicable to its 86%, characterised by $\mu_{sgs}/\mu < 1$ and $\tau_{sgs}/\tau_c < 0.25$, respectively. The corresponding percentages for the whole computational domain are 52.2% and 87.5%. The mesh outside the central region is less refined, which may cause some deviations in the outer shear layers of coflow and ambient air, as seen later in Figure 5.16.

5.6 Impacts of Lewis number

The impacts of Lewis number on the LES of Cheng supersonic flame are assessed by comparing numerical results solved using the mixture-averaged diffusion model, *i.e.*, Case C_0, and the unity-Lewis number assumption, *i.e.*, Case C_1. Figures 5.4(a)-(e) and (f) depict mean and instantaneous distributions of some species mole fractions and mixture fraction, respectively. Each frame shows a 2-D cut on the symmetry plane in the central region of $70D_f \times 10D_f \times 2\pi$. The time-averaged and instantaneous filtered quantities, on the left and right sides of each frame, respectively, are represented by angle brackets, *i.e.*, $\langle X_{H_2} \rangle$, $\langle X_{O_2} \rangle$, $\langle X_{H_2O} \rangle$, $\langle X_{N_2} \rangle$, $\langle X_{OH} \rangle$, and $\langle Z \rangle$, and tilde, *i.e.*, $\widetilde{X}_{H_2}$, $\widetilde{X}_{O_2}$, $\widetilde{X}_{H_2O}$, $\widetilde{X}_{N_2}$, $\widetilde{X}_{OH}$, and $\widetilde{Z}$. Both diffusion models numerically capture turbulent eddies on a range of scales which are intrinsic characteristics of fuel and coflow jets and their mixing layers in the instantaneous contours. Localised differences between the two instantaneous

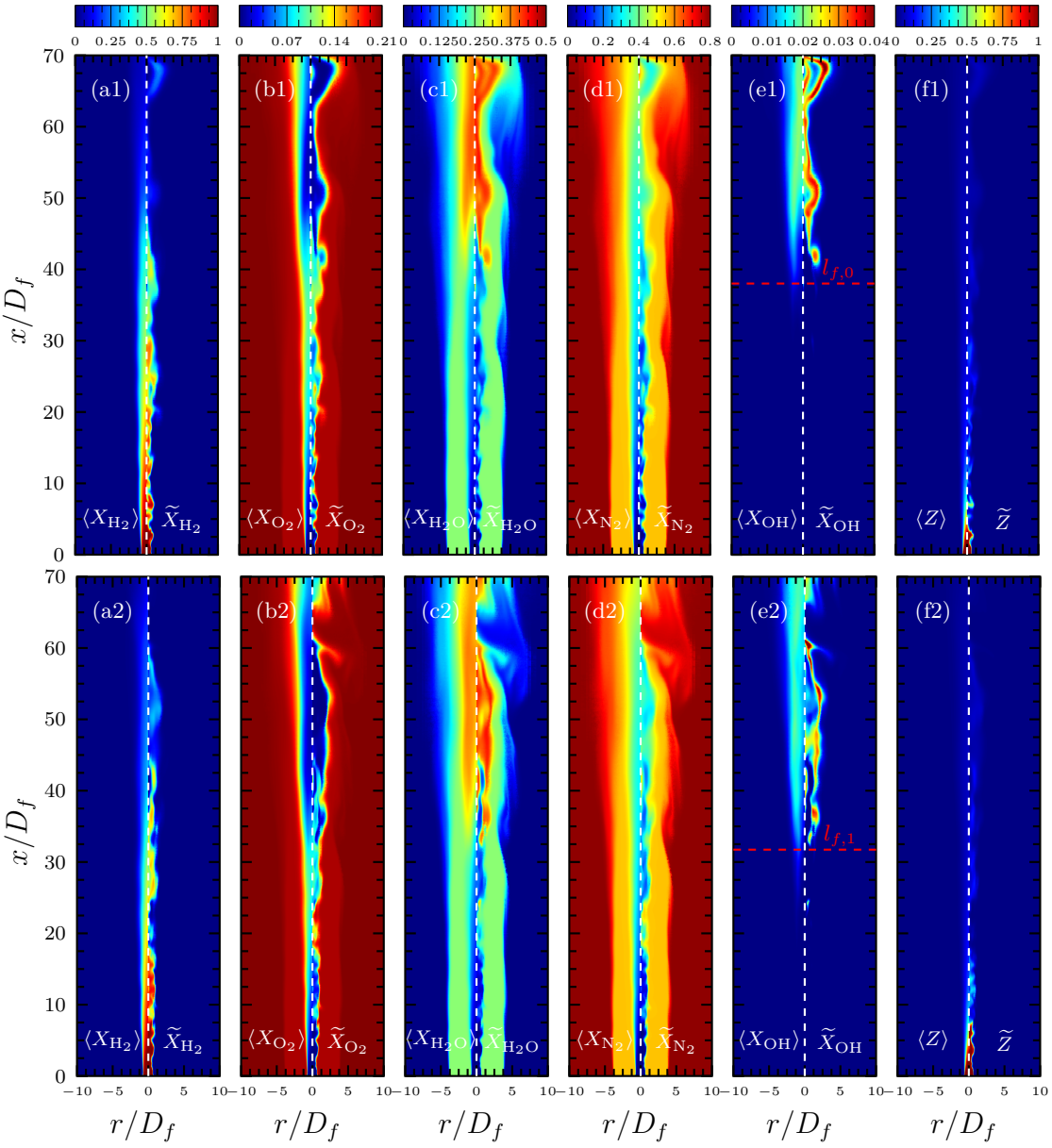


Figure 5.4: Mean (left) and instantaneous (right) distributions of species mole fraction for (a1)-(a2) H_2, (b1)-(b2) O_2, (c1)-(c2) H_2O, (d1)-(d2) N_2, (e1)-(e2) OH, and (f1)-(f2) mixture fraction on the symmetry plane in the central region of $70D_f \times 10D_f \times 2\pi$. Case ID: C_0 (top) and C_1 (bottom).

predictions are observed though with identical initial conditions. They are amplified by the turbulence [165]. The contours of mean species mole fractions predicted by the two diffusion models demonstrate differences mostly in the flame regions with significantly reduced reactants of H_2 and O_2 but increased product of H_2O. Mean flame lift-off heights, *i.e.*, $l_{f,0}$ at $38D_f$ and $l_{f,1}$ at $33.7D_f$ marked in Figures 5.4(e1) and (e2), respectively, are identified by $\langle X_{OH}\rangle = 0.008$ using the method in Refs. [74, 138]. Note that other criteria, *e.g.*, mean temperature ($\langle T\rangle = 1600$ K) from Ref. [73], yield nearly identical results. Those between $24.4D_f$ and $32.4D_f$ have been reported in the literature [11, 73, 74, 137, 138] whilst the experimentally measured value is $25D_f$ [140]. Both $l_{f,0}$ and $l_{f,1}$ are overestimated as such, while $l_{f,0}$ is closer to the experimental value. The different mean flame lift-off heights obtained experimentally and numerically are likely associated with the absence of combustion models in the present simulations referring to Refs. [73, 74, 133, 135, 138], which is not the main focus of this work. Note that unexpected turbulence from unaligned fuel/coflow axes and early ignition from radicals, *e.g.*, OH, in the coflow in the experiments are not mimicked. The two factors may also play a part in the mismatched experimental and numerical results, as referred to by Huang *et al.* [74]. The predictions of $\langle Z\rangle$ using the two diffusion models show qualitative agreement.

The time-averaged statistics, *i.e.*, $\langle X_{H_2}\rangle$, $\langle X_{O_2}\rangle$, $\langle X_{H_2O}\rangle$, $\langle X_{N_2}\rangle$, $\langle X_{OH}\rangle$, and $\langle Z\rangle$, for Cases C_0 and C_1 are presented in Figures 5.5-5.7 in a quantitative way. Their radial profiles at selected streamwise distances are compared to the experimental data from Ref. [140]. At $x/D_f = 32.3$ in Figure 5.5, the two

numerical predictions are in line. $\langle X_{OH} \rangle$ is nearly unchanged at zero along the radial direction. Its experimental profile, whereas, sees local maxima near the jet symmetry. Accordingly, the little consumption of H_2 and generation of H_2O lead to the overestimation of $\langle X_{H_2} \rangle$ and underestimations of $\langle X_{H_2O} \rangle$ in the central jet. Using either diffusion model, combustion occurs at $x/D_f = 43.1$ downstream of both $l_{f,0}$ and $l_{f,1}$. As Figure 5.6 shows, the numerical overprediction of $\langle X_{H_2} \rangle$ and underpredictions of $\langle X_{OH} \rangle$ and $\langle X_{H_2O} \rangle$ in the central jet are less significant, especially using the unity-Lewis number assumption. In the flame regions at $x/D_f = 64.7$ in Figure 5.7, the mixture-averaged diffusion model achieves better accuracy in predicting $\langle X_{OH} \rangle$ and $\langle X_{H_2O} \rangle$ against the experimental data. The two numerical radial profiles of $\langle X_{H_2} \rangle$ deviate from the experimental ones in the central jet. Those of $\langle X_{N_2} \rangle$ are slightly underestimated near the jet symmetry with the dilution effects of unconsumed H_2. Overall, these statistics, especially $\langle X_{O_2} \rangle$, $\langle X_{N_2} \rangle$, and $\langle Z \rangle$, are well reproduced numerically at all the three streamwise distances using both diffusion models, considering uncertainties of asymmetric experimental profiles due to the imperfect burner orientation [140]. Note that the numerical results of $\langle X_{H_2} \rangle$, $\langle X_{O_2} \rangle$, $\langle X_{H_2O} \rangle$, $\langle X_{N_2} \rangle$, $\langle X_{OH} \rangle$, and $\langle Z \rangle$ in the present simulations show comparable accuracy with their counterparts in Ref. [74] which uses an alike fine mesh resolution but the MMC combustion model.

Figure 5.8 shows the profiles of $\langle Z \rangle$ along the centreline. Excellent agreement is observed between the numerical results of Cases C_0 and C_1 and their experimental counterparts, in consistency with the findings in Figures 5.5-5.7(f). The mixing of reactants, *i.e.*, H_2 and O_2, is accurately predicted by either diffusion model as such,

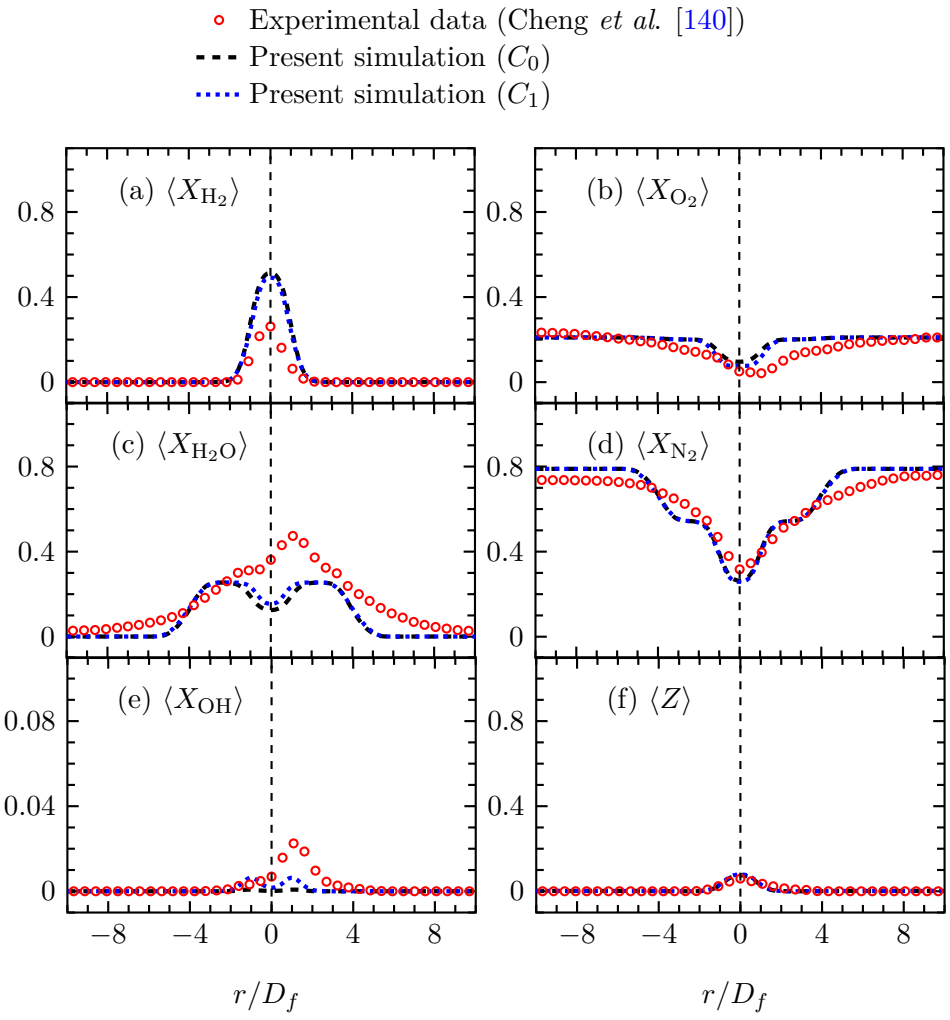


Figure 5.5: Radial profiles of mean (a)-(e) species mole fractions and (f) mixture fraction at $x/D_f = 32.3$.

on which the differences in Lewis numbers impose limited influences.

The role that the differences in Lewis numbers play in numerically capturing autoignition and flame stabilisation is then described. Time sequences of heat release rate fields, *i.e.*, $\widetilde{\omega}_T$, on the symmetry plane in the central region of

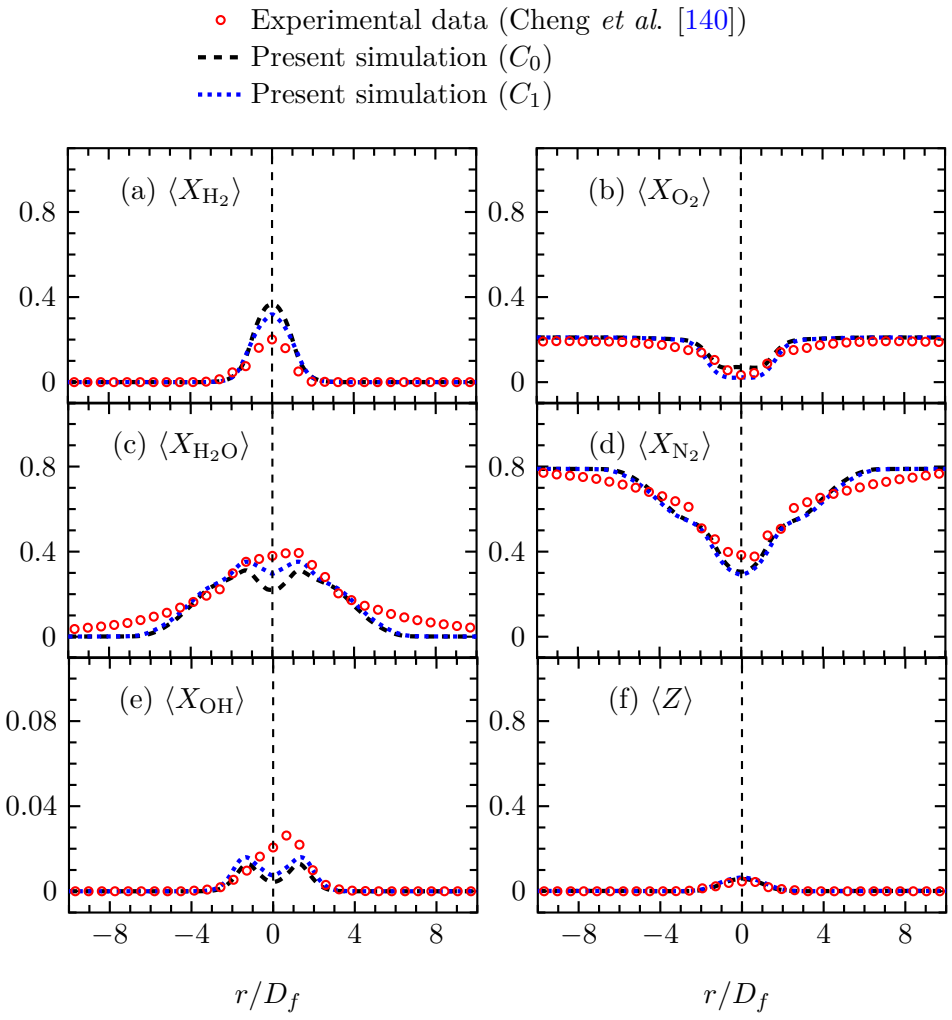


Figure 5.6: Radial profiles of mean (a)-(e) species mole fractions and (f) mixture fraction at $x/D_f = 43.1$.

$(20 - 50)D_f \times 5D_f \times 2\pi$ for Cases C_0 and C_1 are depicted in Figures 5.9(a)-(k). These frames cover the statistics collection period of 0.25 ms with an interval of 0.025 ms. Both numerical predictions report temporal variations of flame position subject to occasional prolonged and compact flames, similar to the work of

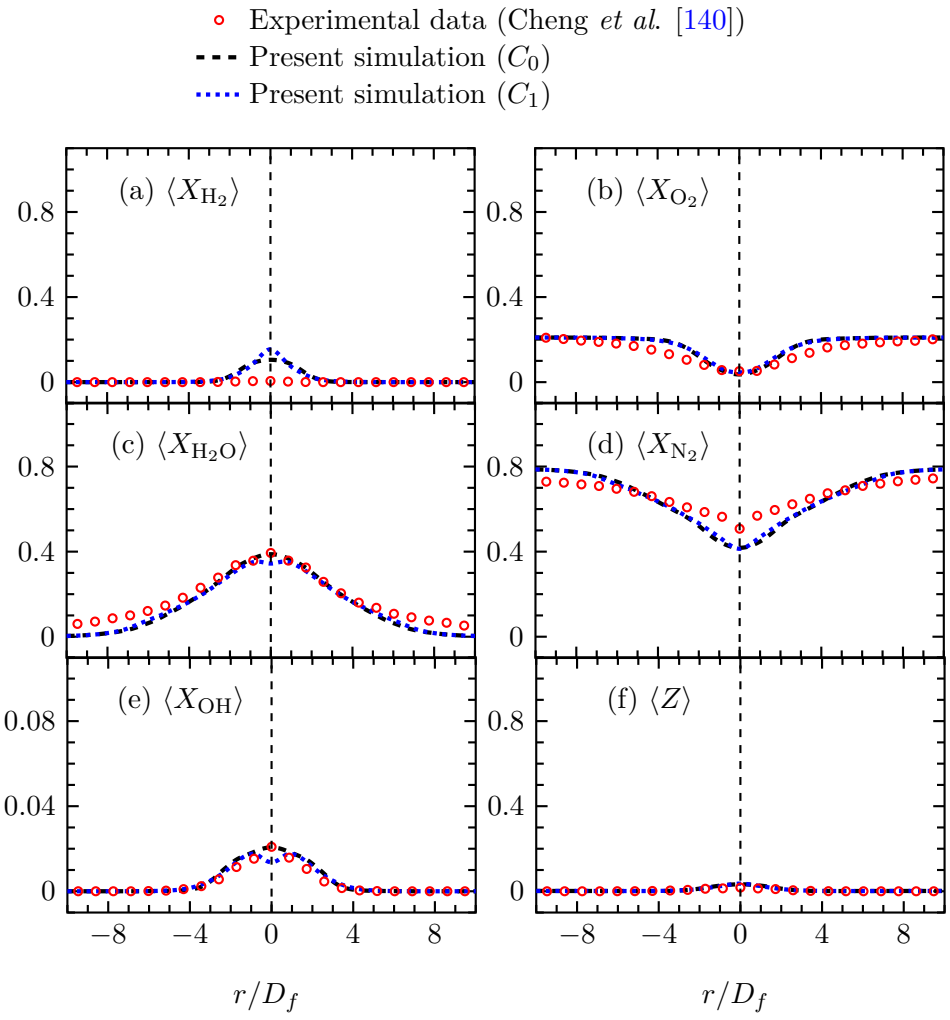


Figure 5.7: Radial profiles of mean (a)-(e) species mole fractions and (f) mixture fraction at $x/D_f = 64.7$.

Bouheraoua *et al.* [137]. This phenomenon is anticipated as a characteristic of turbulent lifted flames in supersonic or subsonic jets, see Refs. [166, 167]. Using either diffusion model, isolated autoignition spots, *e.g.*, AI_0 and AI_1 with spotty high values of $\widetilde{\omega}_T$ in Figures 5.9(h1) and (i2), periodically occur upstream of the

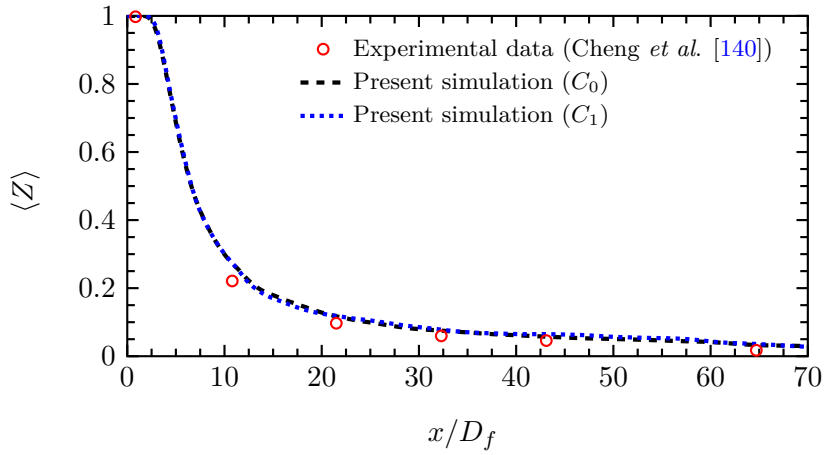


Figure 5.8: Centreline profiles of mean mixture fraction.

main burning zones. The autoignition spots are mostly captured in the shear layers of fuel and coflow jets by the mixture-averaged diffusion model and are generally weak. Those predicted by the unity-Lewis number assumption, whereas, recurrently form near the jet symmetry. They always accumulate into continuous reacting regions downstream and strengthen the main flame subsequently. The differences are distinguishable between Figures 5.9(k1) and (k2) in the two dashed boxes. Note that the unity-Lewis number assumption underestimates the mass diffusion of light species, *e.g.*, H_2 in the central fuel jet, while overestimates that of heavy species, *e.g.*, O_2 in the surrounding annular air stream, discussed later in Figure 5.12. Premixed unburned H_2-O_2 pockets as favourable locations for autoignition tend to build relatively away from the jet symmetry and each other using the mixture-averaged diffusion model, as more H_2 diffuses outwards but less O_2 diffuses inwards. These autoignition spots cannot co-strengthen effectively and

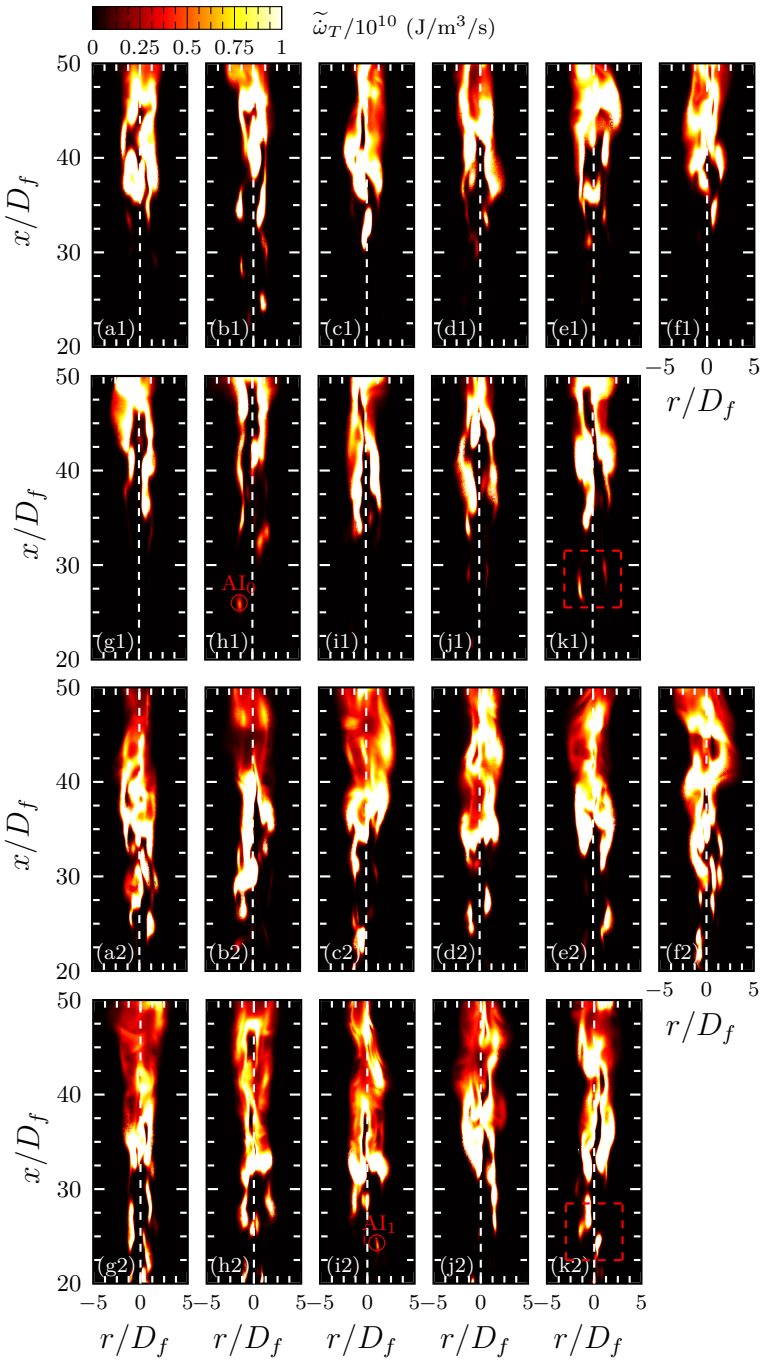


Figure 5.9: Instantaneous distributions of heat release rate at (a1)-(a2) 0.5 ms, (b1)-(b2) 0.525 ms, (c1)-(c2) 0.55 ms, (d1)-(d2) 0.575 ms, (e1)-(e2) 0.6 ms, (f1)-(f2) 0.625 ms, (g1)-(g2) 0.65 ms, (h1)-(h2) 0.675 ms, (i1)-(i2) 0.7 ms, (j1)-(j2) 0.725 ms, and (k1)-(k2) 0.75 ms on the symmetry plane in the central region of $(20-50)D_f \times 5D_f \times 2\pi$. Case ID: C_0 (top) and C_1 (bottom).

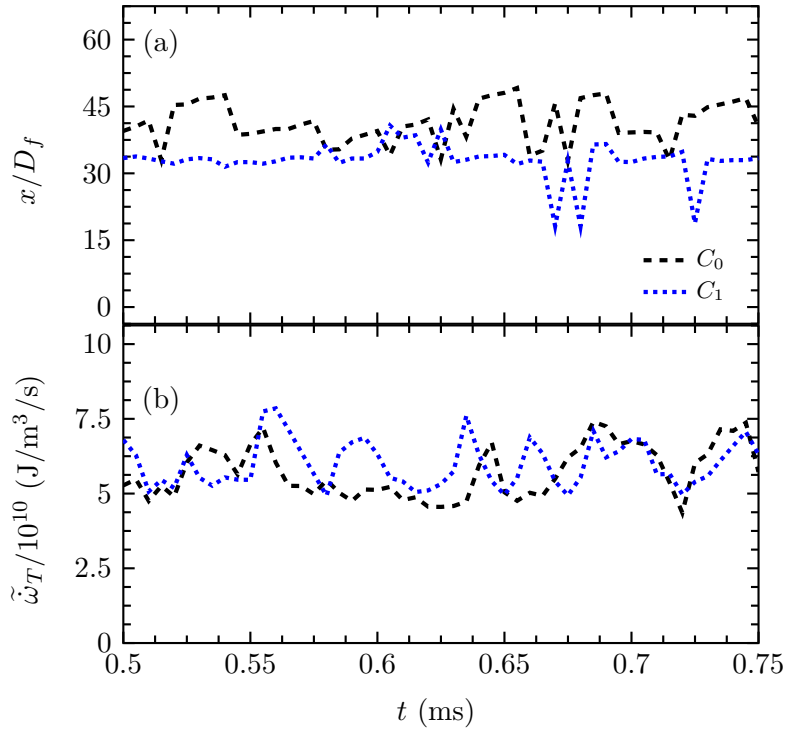


Figure 5.10: Temporal evolutions of (a) flame base location tracked by (b) maximum heat release rate.

thus own lower strengths. The underlying stabilisation mechanism of the flame is that the intricate coupling of autoignition and upstream diamond-shaped shocks controls its dynamics and position oscillations, which has been specified in Refs. [135, 137]. The different predictions of autoignition locations and strengths contribute to different flame structures solved using the two diffusion models. In Figure 5.9, the main flames demonstrated in the top frames further distribute on two sides of the jet symmetry and stabilise at higher streamwise positions compared to those in the bottom frames.

Figures 5.10(a) and (b) provide quantitative comparisons on temporal

evolutions of flame base location and maximum $\widetilde{\dot{\omega}}_T$ between Cases C_0 and C_1, respectively. The flame base is identified where $\widetilde{\dot{\omega}}_T$ peaks instantaneously as in Ref. [137]. It irregularly oscillates in a range of $x/D_f = 32.9 - 49.1$ using the mixture-averaged diffusion model, generally higher than $x/D_f = 18.1 - 40.7$ using the unity-Lewis number assumption. In contrast, the two corresponding ranges of maximum $\widetilde{\dot{\omega}}_T$, *i.e.*, $4.4 \times 10^{10} - 7.4 \times 10^{10}$ and $4.9 \times 10^{10} - 7.9 \times 10^{10}$ J/m^3/s, respectively, are close.

A signed flame index conditioning on localised $\widetilde{\dot{\omega}}_T$, *i.e.*, $\xi_{SFI-\widetilde{\dot{\omega}}_T}$, is used to analyse differences in mixed combustion modes attached to flame stabilisation predicted by the two diffusion models. It is defined as

$$\xi_{SFI-\widetilde{\dot{\omega}}_T} = \xi_{pre-\widetilde{\dot{\omega}}_T} + \xi_{dif-\widetilde{\dot{\omega}}_T}, \tag{5.14}$$

where $\xi_{pre-\widetilde{\dot{\omega}}_T}$ and $\xi_{dif-\widetilde{\dot{\omega}}_T}$ are respectively computed by

$$\begin{cases} \xi_{pre-\widetilde{\dot{\omega}}_T} = \max\left[\text{sign}\left(\nabla\widetilde{Y}_{\text{H}_2} \cdot \nabla\widetilde{Y}_{\text{O}_2} - \varepsilon\right), 0\right] \max\left[\text{sign}\left(\widetilde{\dot{\omega}}_T - \gamma\overline{\widetilde{\dot{\omega}}}_T\right), 0\right] \\ \xi_{dif-\widetilde{\dot{\omega}}_T} = \min\left[\text{sign}\left(\nabla\widetilde{Y}_{\text{H}_2} \cdot \nabla\widetilde{Y}_{\text{O}_2} + \varepsilon\right), 0\right] \max\left[\text{sign}\left(\widetilde{\dot{\omega}}_T - \gamma\overline{\widetilde{\dot{\omega}}}_T\right), 0\right]. \end{cases} \tag{5.15}$$

Here, $\max(x, y)$ and $\min(x, y)$ functions return the larger and smaller one between x and y, respectively; the $\text{sign}(x)$ function returns 1 if $x \geq 0$ and -1 if $x < 0$. $\widetilde{Y}_{\text{H}_2}$ and $\widetilde{Y}_{\text{O}_2}$ denote the mass fractions of H_2 and O_2, respectively. Non-negligible positive dot products of their gradients are distinguished from the rest with ε being a small positive constant, say 10^{-9} here. $\overline{\widetilde{\dot{\omega}}}_T$ is the volume average of $\widetilde{\dot{\omega}}_T$ over the whole computational domain, and $\gamma\overline{\widetilde{\dot{\omega}}}_T$ provides a threshold to identify non-negligible $\widetilde{\dot{\omega}}_T$ with γ being a small fraction, say 1% here.

Three combinations of $\xi_{pre-\widetilde{\dot{\omega}}_T}$ and $\xi_{dif-\widetilde{\dot{\omega}}_T}$ read

$$\begin{cases} \xi_{pre-\widetilde{\dot{\omega}}_T}=1,\ \xi_{dif-\widetilde{\dot{\omega}}_T}=0, & \text{if } \nabla\widetilde{Y}_{\mathrm{H_2}}\cdot\nabla\widetilde{Y}_{\mathrm{O_2}}\geq\varepsilon \text{ and } \widetilde{\dot{\omega}}_T\geq\gamma\overline{\widetilde{\dot{\omega}}}_T \\ \xi_{pre-\widetilde{\dot{\omega}}_T}=0,\ \xi_{dif-\widetilde{\dot{\omega}}_T}=-1, & \text{if } \nabla\widetilde{Y}_{\mathrm{H_2}}\cdot\nabla\widetilde{Y}_{\mathrm{O_2}}<-\varepsilon \text{ and } \widetilde{\dot{\omega}}_T\geq\gamma\overline{\widetilde{\dot{\omega}}}_T \\ \xi_{pre-\widetilde{\dot{\omega}}_T}=0,\ \xi_{dif-\widetilde{\dot{\omega}}_T}=0, & \text{if } -\varepsilon\leq\nabla\widetilde{Y}_{\mathrm{H_2}}\cdot\nabla\widetilde{Y}_{\mathrm{O_2}}<\varepsilon \text{ or } \widetilde{\dot{\omega}}_T<\gamma\overline{\widetilde{\dot{\omega}}}_T, \end{cases} \tag{5.16}$$

which correspond to three values of $\xi_{SFI-\widetilde{\dot{\omega}}_T}$ differentiating three regimes of flow fields: premixed combustion zones with $\xi_{SFI-\widetilde{\dot{\omega}}_T}=1$ (non-negligible co-gradient variations of H_2 and O_2 with non-negligible $\widetilde{\dot{\omega}}_T$), diffusion combustion zones with $\xi_{SFI-\widetilde{\dot{\omega}}_T}=-1$ (non-negligible counter-gradient variations of H_2 and O_2 with non-negligible $\widetilde{\dot{\omega}}_T$), and non-reacting zones with $\xi_{SFI-\widetilde{\dot{\omega}}_T}=0$ (negligible co- and counter-gradient variations of H_2 and O_2 or negligible $\widetilde{\dot{\omega}}_T$).

Figures 5.11(a) and (b) depict instantaneous contours of $\xi_{SFI-\widetilde{\dot{\omega}}_T}$ on the symmetry plane in the central region of $70D_f\times10D_f\times2\pi$ for Cases C_0 and C_1, respectively. Closely downstream of the fuel and coflow inlets, it is filled with a flameless region, *i.e.*, Zone I, using the mixture-averaged diffusion model but two thin diffusion flame stripes, *i.e.*, Zone II, using the unity-Lewis number assumption. Zone III with ribbon-like diffusion flames and two premixed combustion spots inside follows Zone I. Zone IV with spatially more continuous diffusion combustion enclosing more premixed combustion spots follows Zone II. These remarkable differences in distributions of both diffusion and premixed combustion zones are triggered by different predictions of the fuel (H_2) and oxidiser (O_2) mass diffusion in their shear layers. They affect flame structures and stabilisation further downstream.

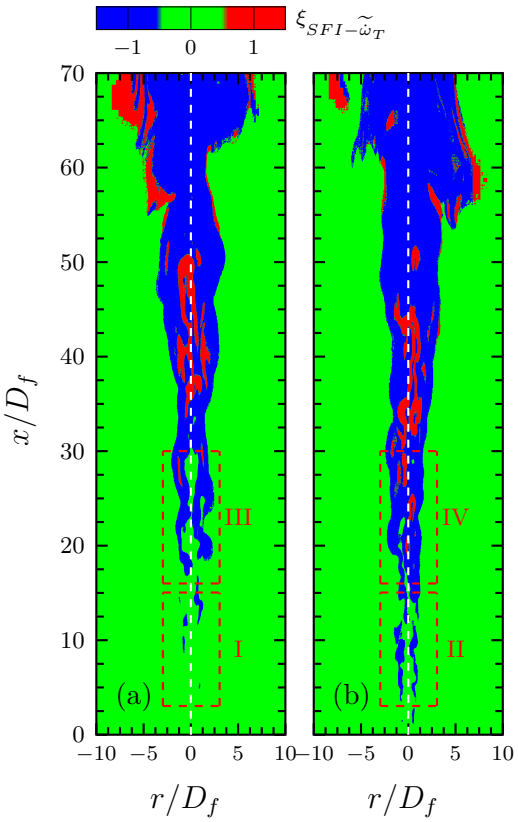


Figure 5.11: Instantaneous distributions of signed flame index on the symmetry plane in the central region of $70D_f \times 10D_f \times 2\pi$. Case ID: C_0 (a) and C_1 (b).

The choice of diffusion models directly changes the filtered mass and thermal diffusivities, *i.e.*, D_i and α. The mass and thermal diffusion terms, *i.e.*, $\left[-\nabla \cdot \bar{\mathbf{J}}_i\right]$ and $\left[-\nabla \cdot \bar{\mathbf{J}}_h\right]$, respectively determined by D_i and α in Eqs. (5.7) and (5.8), are consequently changed. Their different predictions co-contribute to the numerical results demonstrated in Figures 5.4-5.11 and are thus analysed and compared between Cases C_0 and C_1.

Instantaneous scatter plots of $\left[-\nabla \cdot \bar{\mathbf{J}}_i\right]$ for some species against their

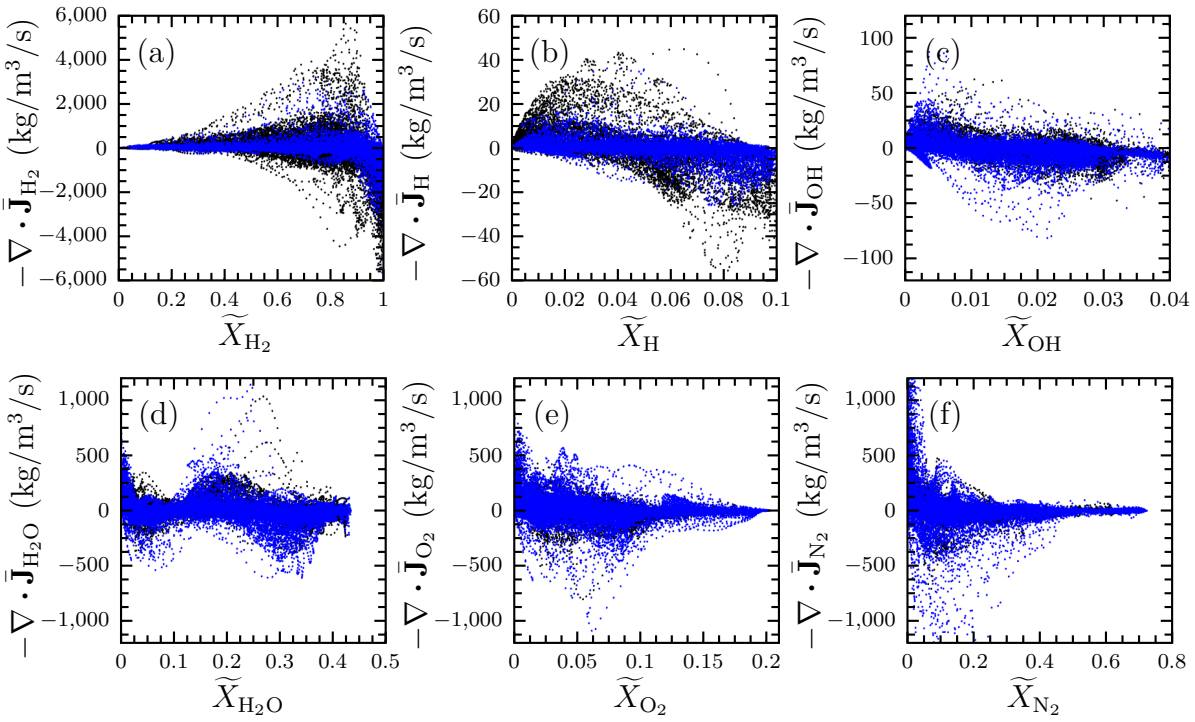


Figure 5.12: Instantaneous scatter plots of species diffusion term against mole fraction for (a) H_2, (b) H, (c) OH, (d) H_2O, (e) O_2, and (f) N_2 on the symmetry plane in the central region of $70D_f \times 5D_f \times 2\pi$. Case ID: C_0 (black scatters) and C_1 (blue scatters).

corresponding mole fractions, *i.e.*, $\widetilde{X}_i$, on the symmetry plane in the central region of $70D_f \times 5D_f \times 2\pi$ are presented in Figures 5.12(a)-(f). The evolutionary tendencies of $\left[-\nabla\cdot\bar{\mathbf{J}}_i\right]$ with respect to $\widetilde{X}_i$ predicted by the two diffusion models are alike. The species mass diffusion primarily occurs at fuel and coflow mixing layers where higher $\widetilde{X}_{\mathrm{H_2}}$ but lower $\widetilde{X}_{\mathrm{H_2O}}$, $\widetilde{X}_{\mathrm{O_2}}$, and $\widetilde{X}_{\mathrm{N_2}}$ are numerically observed, see Figures 5.4(a)-(d). Over the entire ranges of corresponding species mole fractions, $\left[-\nabla\cdot\bar{\mathbf{J}}_{\mathrm{O_2}}\right]$ and $\left[-\nabla\cdot\bar{\mathbf{J}}_{\mathrm{N_2}}\right]$ for heavy species are overestimated, while

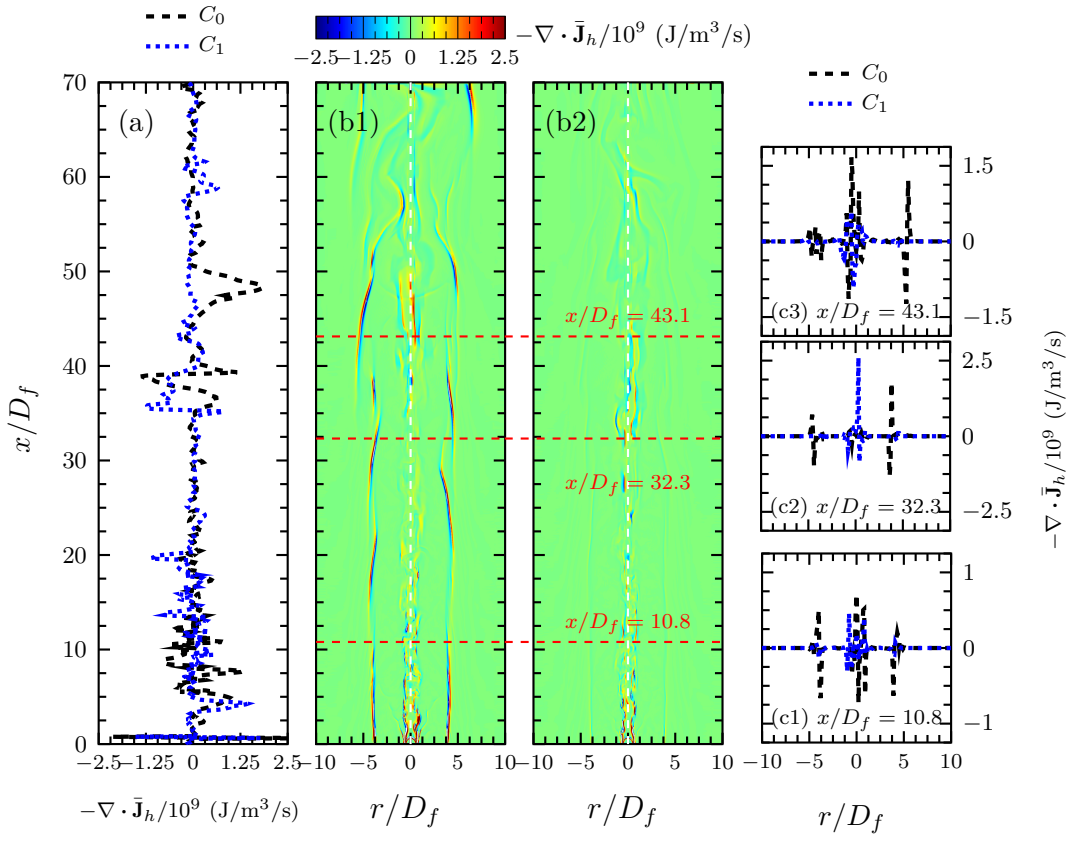


Figure 5.13: Instantaneous (a) centreline profiles, (b1)-(b2) distributions on the symmetry plane in the central region of $70D_f \times 10D_f \times 2\pi$, and (c1)-(c3) radial profiles of thermal diffusion term at $x/D_f = 10.8$, 32.3 and 43.1. Case ID: C_0 (b1) and C_1 (b2).

$\left[-\nabla\cdot\bar{\mathbf{J}}_{\mathrm{H_2}}\right]$ and $\left[-\nabla\cdot\bar{\mathbf{J}}_{\mathrm{H}}\right]$ for light species are highly underestimated using the unity-Lewis number assumption, compared to the mixture-averaged diffusion model. The two predictions of $\left[-\nabla\cdot\bar{\mathbf{J}}_{\mathrm{OH}}\right]$ and $\left[-\nabla\cdot\bar{\mathbf{J}}_{\mathrm{H_2O}}\right]$ for medium-weight species are equally matched. The most different numerical results of the mass diffusion for H_2 and H may play a considerable part in triggering those of autoignition locations and strengths, and thus flame structures and stabilisation.

Figures 5.13(a) and (c1)-(c3) quantitatively show centreline and radial profiles of instantaneous $\left[-\nabla \cdot \bar{\mathbf{J}}_h\right]$ at three streamwise distances, respectively. Instantaneous contours of $\left[-\nabla \cdot \bar{\mathbf{J}}_h\right]$ on the symmetry plane in the central region of $70D_f \times 10D_f \times 2\pi$ are qualitatively depicted in Figures 5.13(b1) and (b2). The thermal diffusion sees positive and negative peaks around the fuel and coflow inlets using both diffusion models in Figure 5.13(a). Along the centreline, its absolute value overall shrinks with fluctuations and localised growths inside the two premixed combustion zones downstream of Zones III and IV, see Figures 5.11(a) and (b). In Figure 5.13(b1), the mixture-averaged diffusion model numerically reports large values of $\left[-\nabla \cdot \bar{\mathbf{J}}_h\right]$ near both the coflow centre and circumference where it mixes with the fuel and the ambient air, respectively. The unity-Lewis number assumption, whereas, predicts noticeable thermal diffusion only at the fuel and coflow mixing layers in Figure 5.13(b2). Figure 5.13(c1)-(c3) support this. The former profiles have ups and downs of $\left[-\nabla \cdot \bar{\mathbf{J}}_h\right]$ at four spanwise locations, while only the two near the jet symmetry are noticeably displayed by the latter ones. More heat diffuses outwards at the coflow circumference where $\left[-\nabla \cdot \bar{\mathbf{J}}_h\right]$ acts as sink terms with its negative parts dominating positive parts using the mixture-averaged diffusion model, compared to the unity-Lewis number assumption.

The aforementioned differences in behaviours of the two diffusion models specify the impacts of Lewis number on the LES of Cheng supersonic flame. These findings are further validated by a scale analysis of the diffusion and convection terms in Eqs. (5.7) and (5.8). The absolute values of ratios between mass diffusion

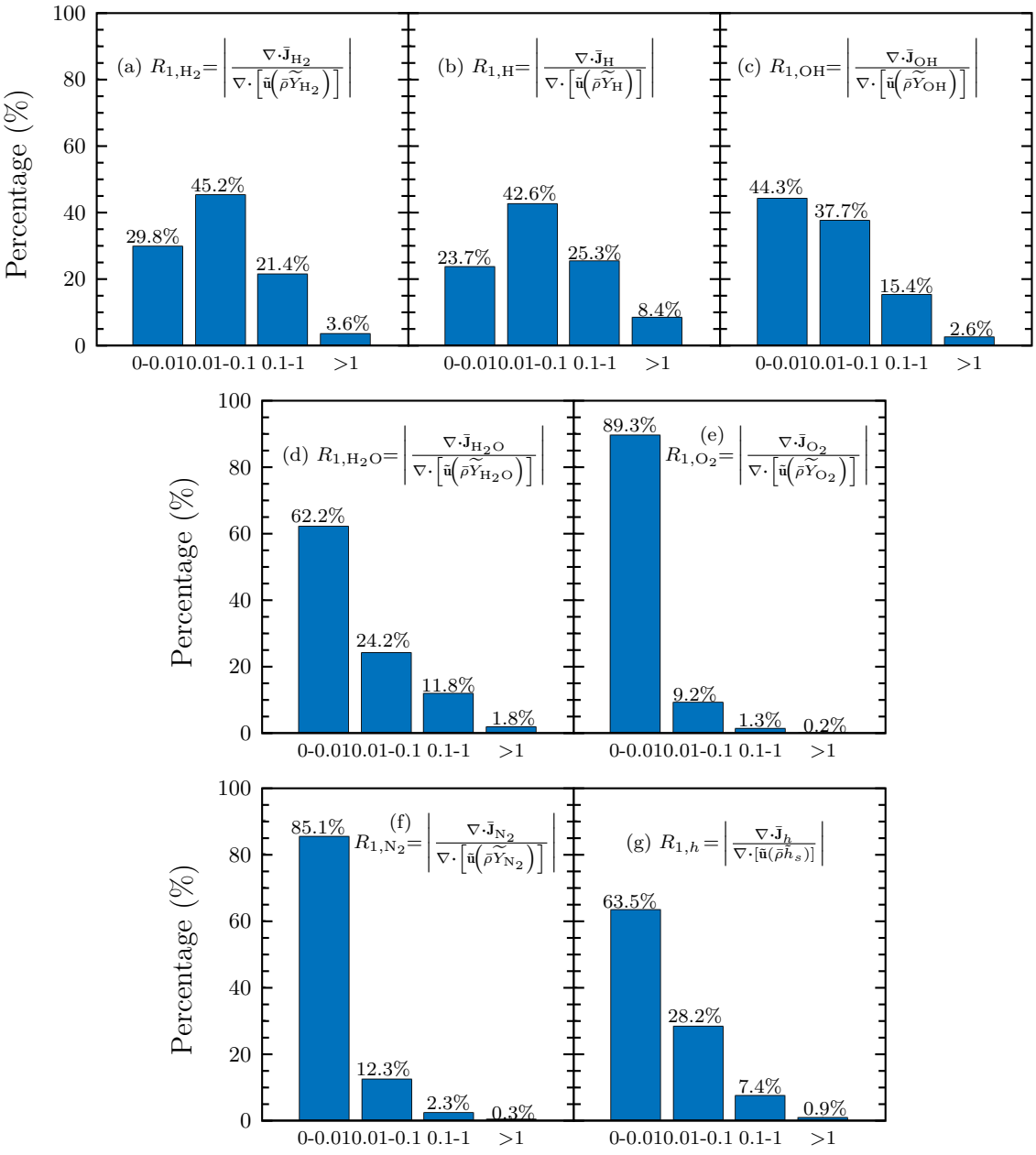


Figure 5.14: Instantaneous percentages of the absolute values of ratios between species diffusion and convection terms for (a) H_2, (b) H, (c) OH, (d) H_2O, (e) O_2, (f) N_2, and (g) thermal diffusion and convection terms in several ranges in the central region of $70D_f \times 5D_f \times 2\pi$. Case ID: C_0.

and convection terms, *i.e.*, $\left|\nabla \cdot \bar{\mathbf{J}}_i \Big/ \nabla \cdot \left[\tilde{\mathbf{u}}\left(\bar{\rho}\widetilde{Y}_i\right)\right]\right|$, for some species, and thermal diffusion and convection terms, *i.e.*, $\left|\nabla \cdot \bar{\mathbf{J}}_h \Big/ \nabla \cdot \left[\tilde{\mathbf{u}}\left(\bar{\rho}\tilde{h}_s\right)\right]\right|$, are examined. They are hereafter termed as $R_{1,i}$ and $R_{1,h}$, respectively, whose instantaneous percentages in the central region of $70D_f \times 5D_f \times 2\pi$ located in several ranges for Case C_0 are presented in Figures 5.14(a)-(f) and (g). $R_{1,\mathrm{H_2}}$ and $R_{1,\mathrm{H}}$ for light species exhibit similar proportional distributions. Their values are mostly between 0.01 and 0.1, accounting for 45.2% and 42.6%, respectively; next are the 0-0.01 and 0.1-1 groups; those over 1 are the least. The percentages of $R_{1,\mathrm{OH}}$ and $R_{1,\mathrm{H_2O}}$ for medium-weight species and $R_{1,h}$ are inversely related to magnitudes of these ranges. Those representing diffusion over one-tenth of convection, *i.e.*, 18%, 13.6%, and 8.3%, still matter. The mass diffusion of heavy species plays a secondary role in comparison with their convection with the percentages of $R_{1,\mathrm{O_2}} \leq 0.01$ and $R_{1,\mathrm{N_2}} \leq 0.01$ equal to 89.3% and 85.1%, respectively. In general, both the mass and thermal diffusions are less than convection but non-negligible, especially for H_2 and H, which explains the phenomena that the differences in Lewis numbers trigger those in the numerical results.

5.7 Impacts of turbulent Schmidt and Prandtl numbers

The impacts of turbulent Schmidt and Prandtl numbers on the LES of Cheng supersonic flame are assessed by comparing numerical results solved using different

combinations of the two parameters, *i.e.*, Cases C_0 and C_2-C_4. Figures 5.15(a) and (b) depict mean and instantaneous distributions of temperature, *i.e.*, $\langle T \rangle$ and $\widetilde{T}$, and axial velocity, *i.e.*, $\langle u_x \rangle$ and $\tilde{u}_x$, respectively. The left and right sides of each frame on the symmetry plane in the central region of $70D_f \times 10D_f \times 2\pi$ correspond to $\langle T \rangle \big/ \langle u_x \rangle$ and $\widetilde{T} \big/ \tilde{u}_x$, respectively. The four sets of turbulent Schmidt and Prandtl numbers with Sc_t and Pr_t equal to 0.5 or 1.0 agree relatively well in predicting the lower halves where $x/D_f \leq 30$ in both the instantaneous and mean contours. The upper halves of the instantaneous temperature fields, especially the flame regions with pronounced rises of $\widetilde{T}$, see noticeable localised differences. Those of $\tilde{u}_x$ accordingly demonstrate differences in flow patterns subject to turbulent eddies. Note that although the turbulent transfer of energy is calculated from that of momentum by Pr_t, the former affects the latter in turn as they are coupled [168]. The interplay of instantaneous flame and flow structures is likewise anticipated. The time-averaged flame lengths and widths along the streamwise and spanwise directions, respectively, are qualitatively identified from the predictions of $\langle T \rangle$. They significantly vary against Sc_t but are less dependent on Pr_t; longer and narrower flames are numerically captured with $Sc_t = 1.0$ for Cases C_0 and C_3. Similarities among the four mean flame lift-off heights, *i.e.*, $l_{f,0}$ at $38D_f$, $l_{f,2}$ and $l_{f,3}$ at $38.9D_f$, and $l_{f,4}$ at $39.3D_f$ marked in Figures 5.15(a1)-(a4), respectively, are predicted. These results indicate that both Sc_t and Pr_t impose minor influences on the mean flame lift-off height, compared to the choice of diffusion models with the inconsistency between $l_{f,0}$ and $l_{f,1}$. The contours of $\langle u_x \rangle$ are comparatively less sensitive to different Sc_t and Pr_t than those of $\langle T \rangle$, which has been reported by Zheng and Yan [152]. When $Sc_t = 1.0$, the two

central zones with large values of $\langle u_x \rangle$, roughly representing run-up distances of fuel and coflow jets, almost cover the whole computational domain. Their counterparts with $Sc_t = 0.5$ for Cases C_2 and C_4, whereas, are moderately shortened.

The radial profiles of $\langle u_x \rangle$ at $x/D_f = 32.3$ and $x/D_f = 43.1$ for Cases C_0 and C_2-C_4 are presented in Figures 5.16(a1) and (a2), respectively, along with the corresponding experimental data from Ref. [140]. At both streamwise distances, all of them display overestimations of $\langle u_x \rangle$ in the central jet but underestimations of radial coflow spreading into the ambient air. The experimental and numerical differences are likely caused by insufficient mesh resolution in the outer shear layers near the coflow circumference [74]. The fact that inflow velocity fluctuations in the experiments cannot be perfectly mimicked by the synthetic ones used in the present simulations may co-contribute to them [11, 73, 74]. The variations of $\langle u_x \rangle$ along the spanwise direction perfectly keep in step using either Sc_t/Pr_t. The quantitative results agree with the qualitative ones of mean axial velocity fields in Figures 5.15(b1)-(b4). Differences in Sc_t and Pr_t barely trigger those in the predictions of $\langle u_x \rangle$.

Figures 5.16(b1)-(b3) show three groups of radial profiles for $\langle T \rangle$. At $x/D_f = 32.3$ and $x/D_f = 43.1$, the numerical predictions of $\langle T \rangle$ are in good agreement among Cases C_0 and C_2-C_4. $\langle T \rangle$ is highly underestimated at $x/D_f = 32.3$ by all the combinations of Sc_t and Pr_t, as the streamwise location is upstream of $l_{f,0}$ and $l_{f,2}$-$l_{f,4}$ but downstream of the experimentally measured mean flame lift-off height, *i.e.*, $25D_f$. The local minima of its numerical profiles near the jet symmetry are consistent with that of $\langle X_{H_2O} \rangle$ in Figure 5.5(c) attached to little product generation.

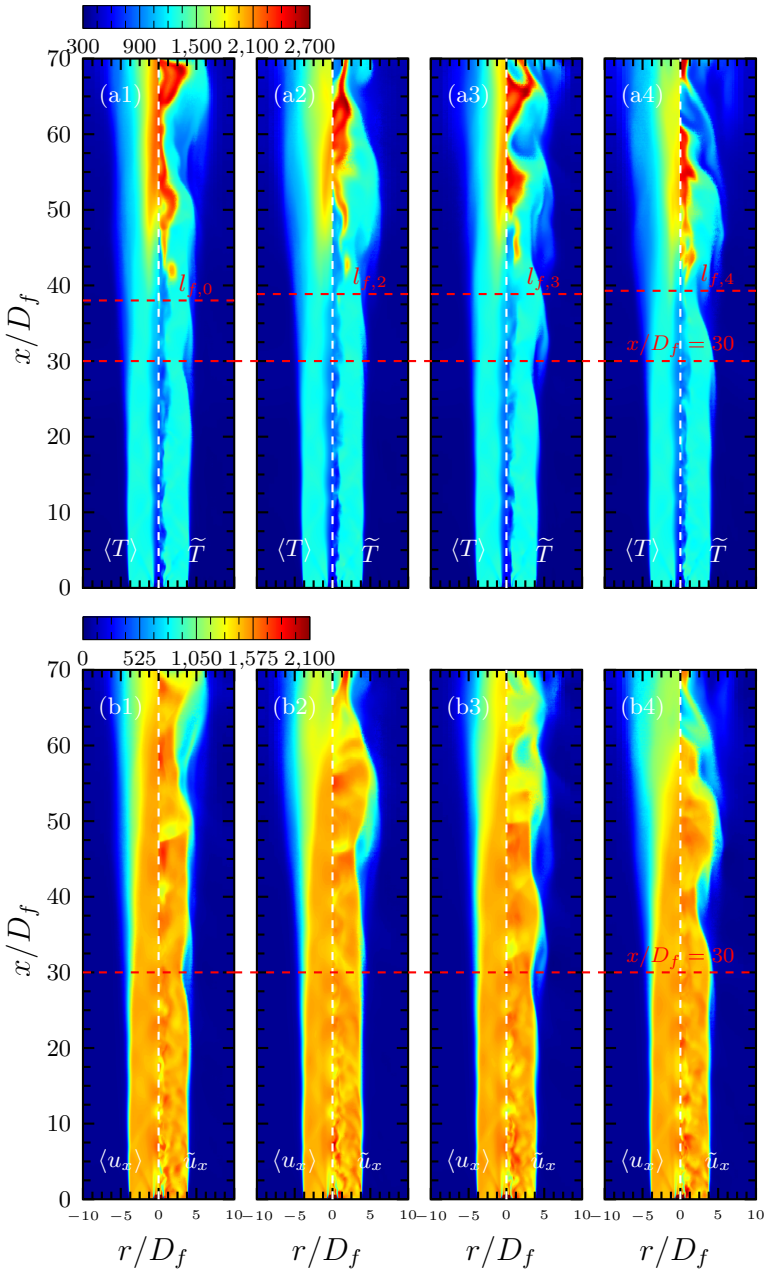


Figure 5.15: Mean (left) and instantaneous (right) distributions of (a1)-(a4) temperature (in K) and (b1)-(b4) axial velocity (in m/s) on the symmetry plane in the central region of $70D_f \times 10D_f \times 2\pi$. Case ID: C_0 (first column), C_2 (second column), C_3 (third column), and C_4 (last column).

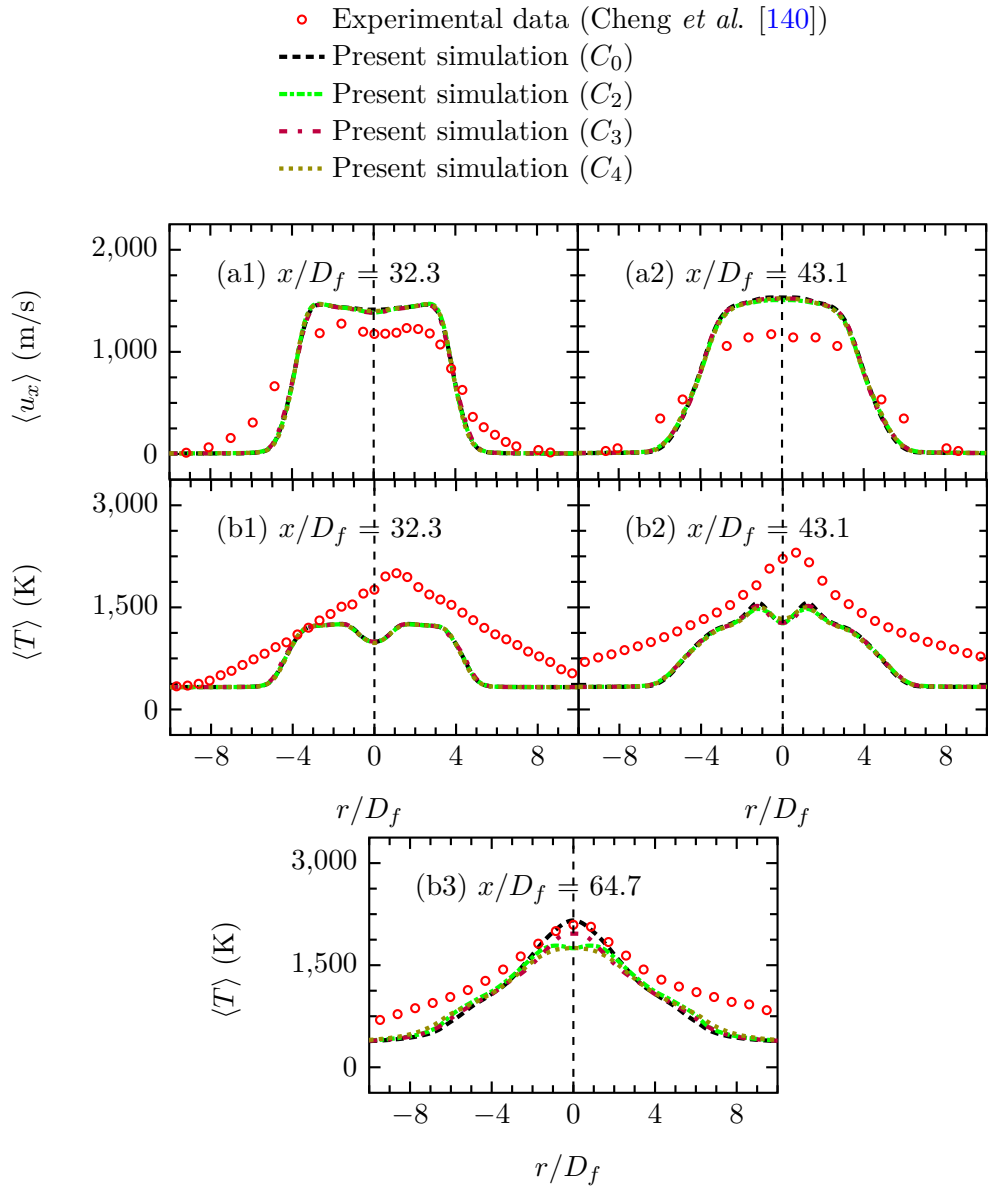


Figure 5.16: Radial profiles of mean (a1)-(a2) axial velocity and (b1)-(b3) temperature.

Improvements regarding the underestimations of $\langle T \rangle$ are observed at $x/D_f = 43.1$ in the flame regions. The numerical radial profiles of $\langle T \rangle$ at $x/D_f = 64.7$ are closer to their experimental counterparts but see differences among themselves in the central jet. The one predicted by $Sc_t = Pr_t = 1.0$ achieves the best accuracy against the experimental data. The set of $Sc_t = 1.0$ and $Pr_t = 0.5$ comes the second, followed by the rest with $Sc_t = 0.5$. Note that the numerical accuracy of $\langle u_x \rangle$ and $\langle T \rangle$ in the present simulations is generally worse than that of their counterparts in Ref. [74] due to the absence of combustion models.

The profiles of $\langle T \rangle$ along the centreline are compared among Cases C_0 and C_2-C_4 in Figure 5.17. The four numerical predictions deviate from the experimental data since about $x/D_f = 10$ due to the occurrence of combustion far more upstream in the experiments. Their centreline profiles continue to closely overlap downstream until over $x/D_f = 50$ where differences start to be triggered by those in Sc_t and Pr_t. The influences of Sc_t on $\langle T \rangle$ in the flame regions are more significant than those of Pr_t but still quite limited.

Figures 5.18(a)-(d) depict instantaneous contours of $\xi_{SFI-\widetilde{\omega}_T}$ on the symmetry plane in the central region of $70D_f \times 10D_f \times 2\pi$ for Cases C_0 and C_2-C_4, respectively. Predicted by either Sc_t/Pr_t, upstream areas where $x/D_f \leq 30$ consist of a flameless region followed by ribbon-like diffusion flames. Zones I-IV with some discretised bubbles of premixed combustion in an extensive background of diffusion flame follow them. Further downstream areas demonstrate a feature of premixed combustion blocks/stripes embedded on the left and right sides of spatially continuous diffusion combustion. When $Pr_t = 1.0$, the two distributions

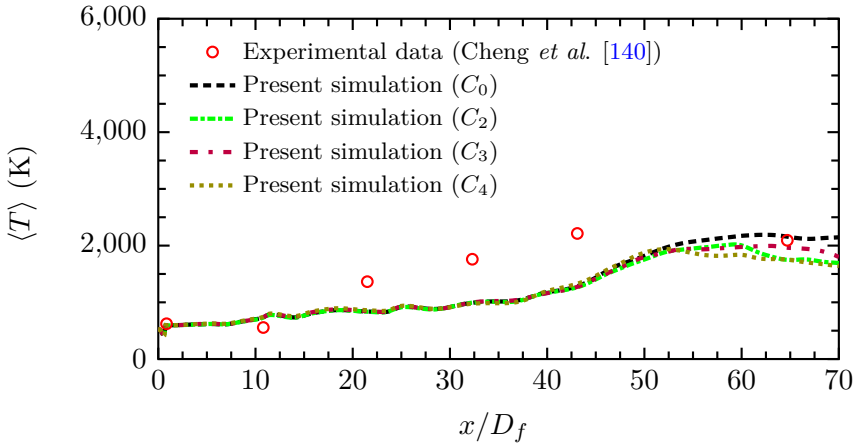


Figure 5.17: Centreline profiles of mean temperature.

of premixed combustion zones located downstream of Zones I and II are less expansive in the spanwise direction. The comparatively high turbulent transfer of energy with $Pr_t = 0.5$ promotes outward expansions of their counterparts. Differences in the turbulent transfer of species dependent on Sc_t also lead to such different predictions but play secondary roles. The premixed combustion blocks downstream of Zone IV are marginally more widespread than those downstream of Zone III.

The aforementioned differences in behaviours of the different combinations of Sc_t and Pr_t specify their impacts on the LES of Cheng supersonic flame. Both Sc_t and Pr_t affect flame structures and stabilisation, to which the degree, whereas, is less remarkable in comparison with Lewis number. These findings are further validated by a scale analysis of the SGS and filtered diffusion terms in Eqs. (5.7) and (5.8). The absolute values of ratios between SGS and filtered mass diffusion terms, *i.e.*,

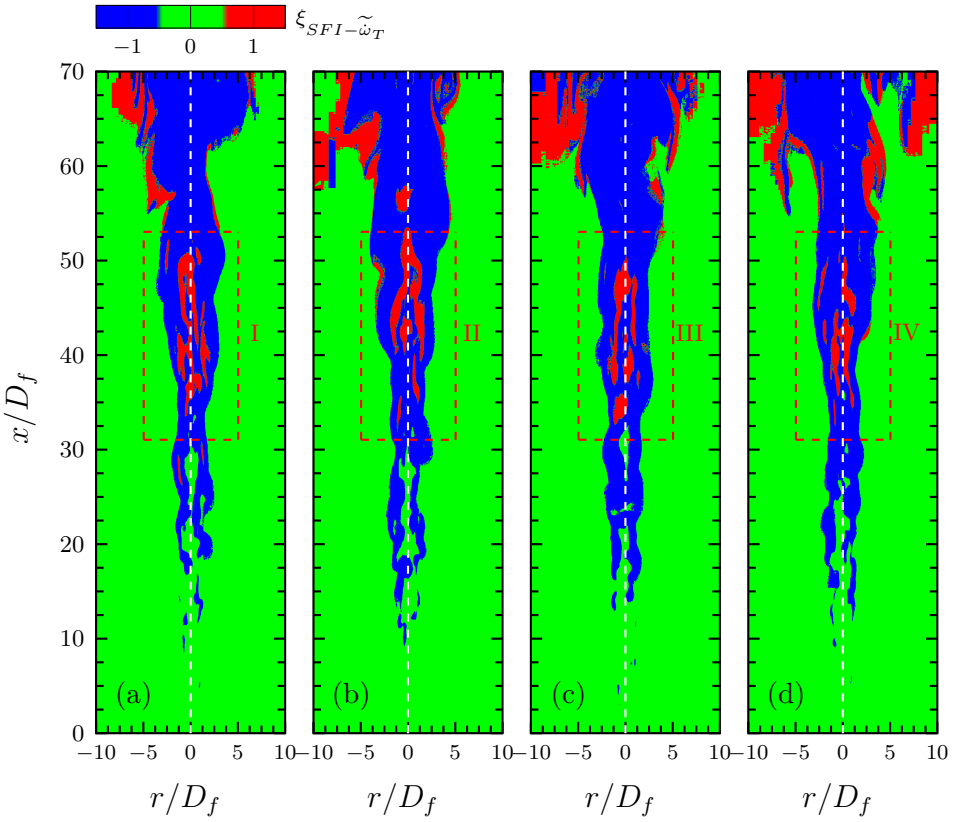


Figure 5.18: Instantaneous distributions of signed flame index on the symmetry plane in the central region of $70D_f \times 10D_f \times 2\pi$. Case ID: C_0 (a), C_2 (b), C_3 (c), and C_4 (d).

$\left|\nabla\cdot\left(\bar{\rho}D_{sgs}\nabla\widetilde{Y}_i\right)\Big/\nabla\cdot\left(\bar{\rho}D_i\nabla\widetilde{Y}_i\right)\right|$, for some species, and thermal diffusion terms, *i.e.*, $\left|\nabla\cdot\left(\bar{\rho}\alpha_{sgs}\nabla\tilde{h}_s\right)\Big/\nabla\cdot\left(\bar{\rho}\alpha\nabla\tilde{h}_s\right)\right|$, are examined. They are hereafter termed as $R_{2,i}$ and $R_{2,h}$, respectively, whose instantaneous percentages in the central region of $70D_f \times 5D_f \times 2\pi$ located in several ranges for Case C_4 are presented in Figures 5.19(a)-(f) and (g). The majorities of $R_{2,\mathrm{H_2}}$ and $R_{2,\mathrm{H}}$ for light species represent their SGS mass diffusion lower than filtered one. The sums of their percentages in

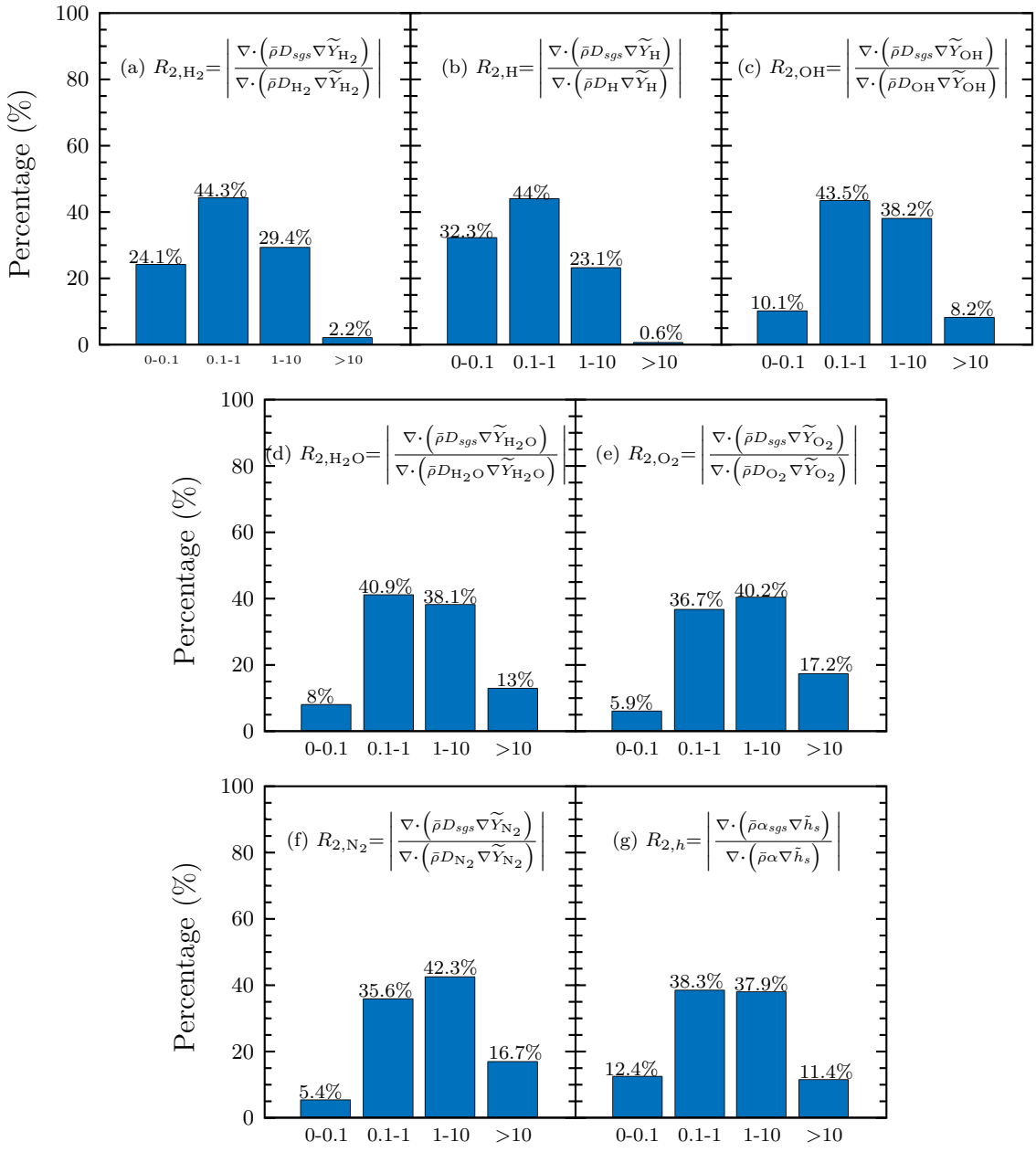


Figure 5.19: Instantaneous percentages of the absolute values of ratios between SGS and filtered species diffusion terms for (a) H_2, (b) H, (c) OH, (d) H_2O, (e) O_2, (f) N_2, and (g) thermal diffusion terms in several ranges in the central region of $70D_f \times 5D_f \times 2\pi$. Case ID: C_4.

the 0-0.01 and 0.1-1 groups are 68.4% and 76.3%, respectively. $R_{2,\mathrm{OH}}$ and $R_{2,\mathrm{H_2O}}$ for medium-weight species fall largely in the two middle ranges. Those between 0.1 and 1, accounting for 43.5% and 40.9%, respectively, are the most. The magnitudes of SGS and filtered thermal diffusions are comparable as the percentages of $R_{2,h}$ between 1 and 10 and over 10 almost counterbalance with those in the 0-0.1 and 0.1-1 groups, respectively. The proportionate distributions of $R_{2,\mathrm{O_2}}$ and $R_{2,\mathrm{N_2}}$ are alike. Their values over 1 occupying 57.4% and 59%, respectively, are more than the rest, indicating that SGS mass diffusion of heavy species matters. In general, with both maximum SGS mass and thermal diffusions when $Sc_t = Pr_t = 0.5$ among all the tests, filtered diffusion still slightly dominates, except for O_2 and N_2, which explains the phenomena that the impacts of Sc_t and Pr_t on the numerical results are subordinate to those of Lewis number.

5.8 Summary

The impacts of Lewis (Le_i of the i-th species), turbulent Schmidt and Prandtl numbers (Sc_t and Pr_t) on the LES of supersonic turbulent flames are the focus of this work. For this purpose, the parametric LES studies on Cheng supersonic flame are performed. The present LES quality and reliability are validated via a *posteriori* analysis of mesh resolution for Case C_0 (species-specific Le_i, $Sc_t = Pr_t = 1.0$). They are consolidated by the good agreement between the numerical solutions and the corresponding experimental measurements on statistics of scalars and velocity.

The differences in numerical results of instantaneous and/or time-averaged

species mole fractions, mixture fraction, heat release rate, flame base location, and mixed modes of premixed and diffusion combustion between Cases C_0 and C_1 (unity Le_i, $Sc_t = Pr_t = 1.0$) describe the impacts of Lewis number. The major findings are summarised on these points:

- Cases C_0 and C_1 see instantaneous localised differences in both the fuel-oxidiser mixing layers and the reacting regions and report different time-averaged flame lift-off heights.
- The autoignition spots are weaker and distribute relatively away from the jet symmetry and the main flames stabilise at higher streamwise positions in Case C_0 than Case C_1.
- The reason for the different numerical results is that the mass diffusion for light species and the thermal diffusion at the outer coflow-ambient air mixing layers are underestimated but the mass diffusion for heavy species is overestimated in Case C_1 than Case C_0.
- The impacts of Lewis number are explained by that both the mass and thermal diffusions are lower than convection in magnitude but remain non-negligible according to their scale analysis for Case C_0.

The differences in numerical results of instantaneous and/or time-averaged temperature, velocity, and mixed combustion modes among Cases C_0, C_2 (species-specific Le_i, $Sc_t = 0.5$, $Pr_t = 1.0$), C_3 (species-specific Le_i, $Sc_t = 1.0$, $Pr_t = 0.5$), and C_4 (species-specific Le_i, $Sc_t = Pr_t = 0.5$) describe the impacts of

Sc_t and Pr_t, to which the degree is less remarkable in comparison with Lewis number. The major findings are summarised on these points:

- Cases C_0, C_2-C_4 see instantaneous localised differences mostly in the reacting regions and report similar time-averaged flame lift-off heights.
- The relatively minor impacts of Sc_t and Pr_t than Lewis number are rationalised by that both the sub-grid scale mass and thermal diffusions are subordinate to filtered diffusion in magnitude according to their scale analysis for Case C_4.

Chapter 6

Conclusions, Claims for Originality, and Future Work

6.1 Conclusions

A new numerical solver named AHISsprayDetFoam has been developed to simulate high-speed chemically reactive flows within the framework of OpenFOAM. The AHISsprayDetFoam solver is a compressible multi-component reactive two-phase gas-droplet flow solver based on the Eulerian-Lagrangian method. It was customised from the built-in OpenFOAM density-based non-reactive rhoCentralFoam solver. Three modules were integrated into the solver to improve its accuracy and efficiency. The first module is the mixture-averaged diffusion model. The second module is the built-in OpenFOAM Lagrangian solver coupled with optimised droplet drag coefficient and convective

heat transfer coefficient sub-models. The last module is a sparse stiff chemistry solver based on dynamic adaptive hybrid integration (AHI-S).

In Chapter 3, the optimised droplet sub-models were verified in correct implementation in the modelling of ammonia droplet acceleration and cooling in the flowing and/or low-temperature air for subsequent simulations in this work. They show good accuracy against experimental and analytical data in reproducing the velocity and temperature evolutions of the ammonia droplet. The accuracy and efficiency gains related to the mixture-averaged diffusion model and the AHI-S chemistry solver were examined by simulating 1-D detonation propagation in ammonia droplet-free/laden ammonia-oxygen mixtures. Numerical results of detonation propagation speed, gaseous temperature, density, and species distributions around the induction zone show good agreement with experimental data and analytical solutions. Compared to the built-in OpenFOAM diffusion model, the mixture-averaged diffusion model provides different numerical predictions of pulsating instabilities in detonation propagation. It shows better accuracy in depicting the detonation structure within the droplet-free section attributed to improved multi-component diffusion modelling. Compared to the built-in OpenFOAM EulerImplicit solver (backward Euler), the AHI-S chemistry solver reduces the computational cost by around 50%. It achieves satisfactory accuracy in calculating detonation propagation speed within the droplet-free section with the optimal efficiency when the safety factor, β, equals 0.5.

In Chapter 4, parametric numerical simulations of detonation propagation and extinction in ammonia droplet-laden premixed ammonia-oxygen gas were performed

in a 2-D planar channel using the AHISsprayDetFoam solver. Numerical results of detonation velocity and cell width in the droplet-free carrier gas show generally fair agreement with experimental and analytical data. The sustained propagation and ultimate quenching of detonation with perturbations from the ammonia droplets were observed under lower and larger values of initial droplet number density ($N_{d,0}$) and diameter (d_0), respectively. The detonation always quenches under $d_0 = 15$ μm. The detonation propagation/extinction behaviour and cell structure were found to be dependent on both d_0 and $N_{d,0}$. The positive correlations between droplet volume fraction, inter-phase mass, momentum, and energy transfers and d_0 are more nonlinear than their counterparts of $N_{d,0}$. The ammonia droplets which freshly enter the post-detonation wave region complete evaporation, acceleration, and heating most and least quickly with $d_0 = 5$ and 15 μm, respectively, under fixed $N_{d,0}$. The post-Mach stem region experiences higher-intensity detonative combustion and thus droplet evaporative, accelerative, and heating effects than the post-incident wave region. During the detonation extinction process, the detonation wave degenerates into detonative spots which then decouple into shock and reaction fronts; the peaks of gaseous pressure, heat release rate, and nitric oxide volume fraction decline.

In Chapter 5, parametric Large Eddy Simulations (LES) of a supersonic lifted hydrogen flame were performed using the AHISsprayDetFoam solver. The emphases are on two aspects: impacts of (1) Lewis number (Le_i of the i-th species) and (2) turbulent Schmidt and Prandtl numbers (Sc_t and Pr_t) on supersonic turbulent flame and flow structures. Five cases were considered: species-specific Le_i, $Sc_t = Pr_t = 1.0$ (C_0); unity Le_i, $Sc_t = Pr_t = 1.0$ (C_1);

species-specific Le_i, $Sc_t = 0.5$, $Pr_t = 1.0$ (C_2); species-specific Le_i, $Sc_t = 1.0$, $Pr_t = 0.5$ (C_3); species-specific Le_i, $Sc_t = Pr_t = 0.5$ (C_4). The quality of the LES was validated via a *posteriori* mesh resolution analysis for Case C_0 and consolidated by the good agreement between subsequent numerical solutions and experimental measurements on statistics of scalars and velocity. Numerical results of instantaneous and/or time-averaged species mole fractions, mixture fraction, heat release rate, flame base location, and mixed modes of premixed and diffusion combustion were compared between Cases C_0 and C_1. Differences in autoignition locations and strengths, and flame structures and stabilisation specify the impacts of Lewis number. They are triggered by different predictions of species mass and thermal diffusions at fuel-coflow and/or coflow-ambient air mixing layers. These differences are rationalised by a scale analysis of mass/thermal diffusion and convection for Case C_0 which suggests the relatively low but non-negligible former against the latter. Cases C_0 and C_2-C_4 barely see differences in terms of instantaneous and/or time-averaged temperature, velocity, and mixed combustion modes except for further downstream areas where combustion occurs. Both Sc_t and Pr_t impose less significant influences than Lewis number, as sub-grid scale mass/thermal diffusion is subordinate to its resolved counterpart according to their scale analysis for Case C_4.

6.2 Claims for originality

The thesis introduces a new numerical solver developed specifically for the modelling of high-speed chemically reactive flows within the framework of OpenFOAM. The solver demonstrates numerical accuracy and computational efficiency in simulations of detonation and supersonic combustion in zero-carbon fuels (ammonia/hydrogen). Insights gained from these simulations include deeper understandings of detonation propagation and extinction in two-phase gas-droplet ammonia fuel and impacts of Lewis, turbulent Schmidt and Prandtl numbers on supersonic turbulent flame and flow structures. Therefore, the thesis sheds light on the feasibility of detonation propulsion systems powered by liquid ammonia spray as fuel. It also contributes to the knowledge about the optimal choice of Lewis, turbulent Schmidt and Prandtl numbers that balances accuracy and efficiency in LES of supersonic turbulent flames. Overall, the thesis advances theoretical understandings and investigates Computational Fluid Dynamics (CFD) tools of high-speed chemically reactive flows, as well as carries implications for the development of cleaner and more efficient propulsion and power generation systems.

6.3 Future work

The focuses of future work are suggested in the following two directions. First, while the observed accuracy and efficiency of the AHISsprayDetFoam solver were

only demonstrated in 1-D and 2-D detonation propagation in ammonia droplet-free/laden NH_3-O_2 mixtures under the specific operating conditions in Chapters 3 and 4, they are expected for 3-D multi-phase detonation problems as well. Second, while the impacts of Lewis number on the LES of supersonic turbulent flames were only assessed by comparing numerical solutions using the mixture-averaged diffusion model and the unity-Lewis number assumption in Chapter 5, the multi-component diffusion model is expected to further improve the numerical accuracy.

Bibliography

[1] H. G. Weller, G. Tabor, H. Jasak, and C. Fureby, "A tensorial approach to computational continuum mechanics using object-oriented techniques", Computers in Physics **12**, 620–631 (1998).

[2] Q. Yang, P. Zhao, and H. Ge, "Reactingfoam-sci: an open source cfd platform for reacting flow simulation", Computers & Fluids **190**, 114–127 (2019).

[3] C. J. Greenshields, H. G. Weller, L. Gasparini, and J. M. Reese, "Implementation of semi-discrete, non-staggered central schemes in a colocated, polyhedral, finite volume framework, for high-speed viscous flows", International Journal for Numerical Methods in Fluids **63**, 1–21 (2010).

[4] A. Kurganov and E. Tadmor, "New high-resolution central schemes for nonlinear conservation laws and convection–diffusion equations", Journal of Computational Physics **160**, 241–282 (2000).

[5] A. Kurganov, S. Noelle, and G. Petrova, "Semidiscrete central-upwind schemes for hyperbolic conservation laws and hamilton–jacobi equations", SIAM Journal on Scientific Computing **23**, 707–740 (2001).

[6] L. Gutiérrez Marcantoni, J. Tamagno, and S. Elaskar, "Rhocentralrffoam: an openfoam solver for high speed chemically active flows – simulation of planar detonations –", Computer Physics Communications **219**, 209–222 (2017).

[7] L. Gutiérrez Marcantoni, J. Tamagno, and S. Elaskar, "A numerical study on the impact of chemical modeling on simulating methane-air detonations", Fuel **240**, 289–298 (2019).

[8] L. Gutiérrez Marcantoni, J. Tamagno, and S. Elaskar, "Two-dimensional numerical simulations of detonation cellular structures in h2-o2-ar mixtures with openfoam®", International Journal of Hydrogen Energy **42**, 26102–26113 (2017).

[9] Z. Huang, M. Zhao, Y. Xu, G. Li, and H. Zhang, "Eulerian-lagrangian modelling of detonative combustion in two-phase gas-droplet mixtures with openfoam: validations and verifications", Fuel **286**, 119402 (2021).

[10] M. Zhao and H. Zhang, "Rotating detonative combustion in partially pre-vaporized dilute n-heptane sprays: droplet size and equivalence ratio effects", Fuel **304**, 121481 (2021).

[11] H. Zhang, M. Zhao, and Z. Huang, "Large eddy simulation of turbulent supersonic hydrogen flames with openfoam", Fuel **282**, 118812 (2020).

[12] Z. Huang, M. J. Cleary, and H. Zhang, "Application of the sparse-lagrangian multiple mapping conditioning approach to a model supersonic combustor", Physics of Fluids **32**, 105120 (2020).

[13] W. Sutherland, "Lii. the viscosity of gases and molecular force", The London, Edinburgh, and Dublin Philosophical Magazine and Journal of Science **36**, 507–531 (1893).

[14] B. E. Poling, J. M. Prausnitz, and J. P. O'connell, "Properties of gases and liquids", McGraw-Hill Education (2001).

[15] D. G. Goodwin, H. K. Moffat, and R. L. Speth, "Cantera: an object-oriented software toolkit for chemical kinetics, thermodynamics, and transport processes", Cantera Developers (2018).

[16] R. J. Kee, F. M. Rupley, E. Meeks, and J. A. Miller, "Chemkin-iii: a fortran chemical kinetics package for the analysis of gas-phase chemical and plasma kinetics", Sandia National Lab, SAND-96–8216 (1996).

[17] D. Zhou and S. Yang, "A robust reacting flow solver with detailed transport, chemistry, and steady-state preserving splitting schemes based on openfoam and cantera", AIAA Scitech 2020 Forum, 2139 (2020).

[18] M. X. Yao, J.-P. Hickey, P. C. Ma, and M. Ihme, "Molecular diffusion and phase stability in high-pressure combustion", Combustion and Flame **210**, 302–314 (2019).

[19] C. Bruno, V. Sankaran, H. Kolla, and J. H. Chen, "Impact of multi-component diffusion in turbulent combustion using direct numerical simulations", Combustion and Flame **162**, 4313–4330 (2015).

[20] C. T. Crowe, J. D. Schwarzkopf, M. Sommerfeld, and Y. Tsuji, "Multiphase flows with droplets and particles", CRC press (2011).

[21] G. Wang, D. Zhang, K. Liu, and J. Wang, "An improved ce/se scheme for numerical simulation of gaseous and two-phase detonations", Computers & Fluids **39**, 168–177 (2010).

[22] A. K. Hayashi, N. Tsuboi, and E. Dzieminska, "Numerical study on jp-10/air detonation and rotating detonation engine", AIAA Journal **58**, 5078–5094 (2020).

[23] Z. Ren, B. Wang, G. Xiang, and L. Zheng, "Effect of the multiphase composition in a premixed fuel–air stream on wedge-induced oblique detonation stabilisation", Journal of Fluid Mechanics **846**, 411–427 (2018).

[24] Z. Zhang, C. Wen, Y. Liu, D. Zhang, and Z. Jiang, "Application of ce/se method to gas-particle two-phase detonations under an eulerian-lagrangian framework", Journal of Computational Physics **394**, 18–40 (2019).

[25] D. A. Schwer, "Multi-dimensional simulations of liquid-fueled jp10/oxygen detonations, aiaa propulsion and energy 2019 forum", AIAA Propulsion and Energy 2019 Forum, 4042 (2019).

[26] H. Watanabe, A. Matsuo, A. Chinnayya, K. Matsuoka, A. Kawasaki, and J. Kasahara, "Numerical analysis of the mean structure of gaseous detonation with dilute water spray", Journal of Fluid Mechanics **887**, A4 (2020).

[27] Y. M. F. E. Hasadi and J. T. Padding, "On the existence of logarithmic terms in the drag coefficient and nusselt number of a single sphere at high reynolds numbers", arXiv: Fluid Dynamics (2020).

[28] S. Whitaker, "Forced convection heat transfer correlations for flow in pipes, past flat plates, single cylinders, single spheres, and for flow in packed beds and tube bundles", AIChE Journal **18**, 361–371 (1972).

[29] T. Lu and C. K. Law, "A directed relation graph method for mechanism reduction", Proceedings of the Combustion Institute **30**, 1333–1341 (2005).

[30] P. Pepiot-Desjardins and H. Pitsch, "An efficient error-propagation-based reduction method for large chemical kinetic mechanisms", Combustion and Flame **154**, 67–81 (2008).

[31] W. Sun, Z. Chen, X. Gou, and Y. Ju, "A path flux analysis method for the reduction of detailed chemical kinetic mechanisms", Combustion and Flame **157**, 1298–1307 (2010).

[32] R. Sankaran, E. R. Hawkes, J. H. Chen, T. Lu, and C. K. Law, "Structure of a spatially developing turbulent lean methane–air bunsen flame", Proceedings of the Combustion Institute **31**, 1291–1298 (2007).

[33] X. Zheng, T. Lu, and C. Law, "Experimental counterflow ignition temperatures and reaction mechanisms of 1,3-butadiene", Proceedings of the Combustion Institute **31**, 367–375 (2007).

[34] K. E. Niemeyer, C.-J. Sung, and M. P. Raju, "Skeletal mechanism generation for surrogate fuels using directed relation graph with error propagation and sensitivity analysis", Combustion and Flame **157**, 1760–1770 (2010).

[35] C. Xu, Y. Gao, Z. Ren, and T. Lu, "A sparse stiff chemistry solver based on dynamic adaptive integration for efficient combustion simulations", Combustion and Flame **172**, 183–193 (2016).

[36] P. N. Brown, G. D. Byrne, and A. C. Hindmarsh, "Vode: a variable-coefficient ode solver", SIAM Journal on Scientific and Statistical Computing **10**, 1038–1051 (1989).

[37] M. Caracotsios and W. E. Stewart, "Sensitivity analysis of initial value problems with mixed odes and algebraic equations", Computers & Chemical Engineering **9**, 359–365 (1985).

[38] A. Imren and D. Haworth, "On the merits of extrapolation-based stiff ode solvers for combustion cfd", Combustion and Flame **174**, 1–15 (2016).

[39] B. Wu, "High-fidelity modeling of buoyancy-driven diffusion flames towards fire suppression", University of Connecticut (2020).

[40] Y. Gao, Y. Liu, Z. Ren, and T. Lu, "A dynamic adaptive method for hybrid integration of stiff chemistry", Combustion and Flame **162**, 287–295 (2015).

[41] B. Wu, X. Zhao, B. R. Chowdhury, B. M. Cetegen, C. Xu, and T. Lu, "A numerical investigation of the flame structure and blowoff characteristics of a bluff-body stabilized turbulent premixed flame", Combustion and Flame **202**, 376–393 (2019).

[42] C. R. Wilke, "A Viscosity Equation for Gas Mixtures", The Journal of Chemical Physics **18**, 517–519 (1950).

[43] R. J. Kee, M. E. Coltrin, and P. Glarborg, "Chemically reacting flow: theory and practice", John Wiley & Sons (2005).

[44] S. Chapman and T. G. Cowling, "The mathematical theory of non-uniform gases: an account of the kinetic theory of viscosity, thermal conduction and diffusion in gases", Cambridge university press (1990).

[45] D. W. Green and M. Z. Southard, "Perry's chemical engineers' handbook", McGraw-Hill Education (2019).

[46] B. Abramzon and W. Sirignano, "Droplet vaporization model for spray combustion calculations", International Journal of Heat and Mass Transfer **32**, 1605–1618 (1989).

[47] Z. Huang, M. Zhao, and H. Zhang, "Modelling n-heptane dilute spray flames in a model supersonic combustor fueled by hydrogen", Fuel **264**, 116809 (2020).

[48] Z. Huang and H. Zhang, "On the interactions between a propagating shock wave and evaporating water droplets", Physics of Fluids **32**, 123315 (2020).

[49] E. N. Fuller, P. D. Schettler, and J. C. Giddings, "New method for prediction of binary gas-phase diffusion coefficients", Industrial & Engineering Chemistry **58**, 18–27 (1966).

[50] E. L. Cussler, "Diffusion: mass transfer in fluid systems", Cambridge university press (2009).

[51] W. E. Ranz and W. R. Marshall, "Evaporation from drops : part i", Chemical Engineering Progress **48**, 173–180 (1952).

[52] A. B. Liu, D. Mather, and R. D. Reitz, "Modeling the effects of drop drag and breakup on fuel sprays", SAE Technical Paper, 970032 (1993).

[53] P. P. Brown and D. F. Lawler, "Sphere drag and settling velocity revisited", Journal of Environmental Engineering **129**, 222–231 (2003).

[54] H. Kramers, "Heat transfer from spheres to flowing media", Physica **12**, 61–80 (1946).

[55] J. Will, N. Kruyt, and C. Venner, "An experimental study of forced convective heat transfer from smooth, solid spheres", International Journal of Heat and Mass Transfer **109**, 1059–1067 (2017).

[56] T. Yuge, "Experiments on heat transfer from spheres including combined natural and forced convection", Journal of Heat Transfer **82**, 214–220 (1960).

[57] S. H. Lam, "Model reductions with special csp data", Combustion and Flame **160**, 2707–2711 (2013).

[58] K. Wu, Y. Jiang, Z. Huo, D. Cheng, and X. Fan, "An improved stiff-ode solving framework for reacting flow simulations with detailed chemistry in openfoam", Combustion Theory and Modelling **27**, 57–82 (2023).

[59] D. A. Schwer, J. E. Tolsma, W. H. Green, and P. I. Barton, "On upgrading the numerics in combustion chemistry codes", Combustion and Flame **128**, 270–291 (2002).

[60] H. Curran, P. Gaffuri, W. Pitz, and C. Westbrook, "A comprehensive modeling study of n-heptane oxidation", Combustion and Flame **114**, 149–177 (1998).

[61] H. Wang and M. Frenklach, "A detailed kinetic modeling study of aromatics formation in laminar premixed acetylene and ethylene flames", Combustion and Flame **110**, 173–221 (1997).

[62] J. Crank and P. Nicolson, "A practical method for numerical evaluation of solutions of partial differential equations of the heat-conduction type", Mathematical Proceedings of the Cambridge Philosophical Society **43**, 50–67 (1947).

[63] B. van Leer, "Towards the ultimate conservative difference scheme. ii. monotonicity and conservation combined in a second-order scheme", Journal of Computational Physics **14**, 361–370 (1974).

[64] G. B. Macpherson, N. Nordin, and H. G. Weller, "Particle tracking in unstructured, arbitrary polyhedral meshes for use in cfd and molecular

dynamics", Communications in Numerical Methods in Engineering **25**, 263–273 (2009).

[65] J. K. Dukowicz, "A particle-fluid numerical model for liquid sprays", Journal of Computational Physics **35**, 229–253 (1980).

[66] M. Zhao, J.-M. Li, C. J. Teo, B. C. Khoo, and H. Zhang, "Effects of variable total pressures on instability and extinction of rotating detonation combustion", Flow, Turbulence and Combustion **104**, 261–290 (2020).

[67] M. Zhao and H. Zhang, "Origin and chaotic propagation of multiple rotating detonation waves in hydrogen/air mixtures", Fuel **275**, 117986 (2020).

[68] M. Zhao, M. J. Cleary, and H. Zhang, "Combustion mode and wave multiplicity in rotating detonative combustion with separate reactant injection", Combustion and Flame **225**, 291–304 (2021).

[69] Y. Xu and H. Zhang, "Interactions between a propagating detonation wave and circular water cloud in hydrogen/air mixture", Combustion and Flame **245**, 112369 (2022).

[70] Y. Xu and H. Zhang, "Pulsating propagation and extinction of hydrogen detonations in ultrafine water sprays", Combustion and Flame **241**, 112086 (2022).

[71] Z. Huang, Y. Xu, S. Li, Q. Meng, and H. Zhang, "Detailed simulations of one-dimensional detonation propagation in dilute n-heptane spray and air mixtures", Physics of Fluids **35**, 126116 (2023).

[72] Q. Meng, M. Zhao, Y. Xu, L. Zhang, and H. Zhang, "Structure and dynamics of spray detonation in n-heptane droplet/vapor/air mixtures", Combustion and Flame **249**, 112603 (2023).

[73] M. Zhao, Z. X. Chen, H. Zhang, and N. Swaminathan, "Large eddy simulation of a supersonic lifted hydrogen flame with perfectly stirred reactor model", Combustion and Flame **230**, 111441 (2021).

[74] Z. Huang, M. J. Cleary, Z. Ren, and H. Zhang, "Large eddy simulation of a supersonic lifted hydrogen flame with sparse-lagrangian multiple mapping conditioning approach", Combustion and Flame **238**, 111756 (2022).

[75] Z. Huang and H. Zhang, "Investigations of autoignition and propagation of supersonic ethylene flames stabilized by a cavity", Applied Energy **265**, 114795 (2020).

[76] Y. Li, M. Bi, B. Li, Y. Zhou, L. Huang, and W. Gao, "Explosion hazard evaluation of renewable hydrogen/ammonia/air fuels", Energy **159**, 252–263 (2018).

[77] Z. Yu and H. Zhang, "End-gas autoignition and knocking combustion of ammonia/hydrogen/air mixtures in a confined reactor", International Journal of Hydrogen Energy **47**, 8585–8602 (2022).

[78] R. Zhu, M. Zhao, and H. Zhang, "Numerical simulation of flame acceleration and deflagration-to-detonation transition in ammonia-hydrogen–oxygen mixtures", International Journal of Hydrogen Energy **46**, 1273–1287 (2021).

[79] H. Xiao, A. Valera-Medina, and P. J. Bowen, "Modeling combustion of ammonia/hydrogen fuel blends under gas turbine conditions", Energy & Fuels **31**, 8631–8642 (2017).

[80] G. Jourdan, L. Biamino, C. Mariani, C. Blanchot, E. Daniel, J. Massoni, L. Houas, R. Tosello, and D. Praguine, "Attenuation of a shock wave passing through a cloud of water droplets", Shock Waves **20**, 285–296 (2010).

[81] A. Chauvin, E. Daniel, A. Chinnayya, J. Massoni, and G. Jourdan, "Shock waves in sprays: numerical study of secondary atomization and experimental comparison", Shock waves **26**, 403–415 (2016).

[82] Z. Weng, R. Mével, and N. Chaumeix, "Detonation in ammonia-oxygen and ammonia-nitrous oxide mixtures", Combustion and Flame **251**, 112680 (2023).

[83] S. Browne, J. Ziegler, and J. Shepherd, "Numerical solution methods for shock and detonation jump conditions", GALCIT report FM2006 **6**, 90 (2008).

[84] R. Mével, S. Javoy, F. Lafosse, N. Chaumeix, G. Dupré, and C.-E. Paillard, "Hydrogen–nitrous oxide delay times: shock tube experimental study and kinetic modelling", Proceedings of the Combustion Institute **32**, 359–366 (2009).

[85] S. Yungster and K. Radhakrishnan, "Pulsating one-dimensional detonations in hydrogen–air mixtures", Combustion Theory and Modelling **8**, 745–770 (2004).

[86] W. Han, C. Wang, and C. K. Law, "Pulsation in one-dimensional h2–o2 detonation with detailed reaction mechanism", Combustion and Flame **200**, 242–261 (2019).

[87] M. Zhao, Z. Ren, and H. Zhang, "Pulsating detonative combustion in n-heptane/air mixtures under off-stoichiometric conditions", Combustion and Flame **226**, 285–301 (2021).

[88] R. Zhu, X. Fang, C. Xu, M. Zhao, H. Zhang, and M. Davy, "Pulsating one-dimensional detonation in ammonia-hydrogen–air mixtures", International Journal of Hydrogen Energy **47**, 21517–21536 (2022).

[89] J. H. S. Lee, "The detonation phenomenon", Cambridge University Press (2008).

[90] J. B. McVey and T. Y. Toong, "Mechanism of instabilities of exothermic hypersonic blunt-body flows", Combustion Science and Technology **3**, 63–76 (1971).

[91] A. Valera-Medina, H. Xiao, M. Owen-Jones, W. David, and P. Bowen, "Ammonia for power", Progress in Energy and Combustion Science **69**, 63–102 (2018).

[92] F. R. Westlye, A. Ivarsson, and J. Schramm, "Experimental investigation of nitrogen based emissions from an ammonia fueled si-engine", Fuel **111**, 239–247 (2013).

[93] K. Ryu, G. E. Zacharakis-Jutz, and S.-C. Kong, "Performance characteristics of compression-ignition engine using high concentration of ammonia mixed with dimethyl ether", Applied Energy **113**, 488–499 (2014).

[94] M. Ezzat and I. Dincer, "Energy and exergy analyses of a novel ammonia combined power plant operating with gas turbine and solid oxide fuel cell systems", Energy **194**, 116750 (2020).

[95] E. C. Okafor, K. K. A. Somarathne, R. Ratthanan, A. Hayakawa, T. Kudo, O. Kurata, N. Iki, T. Tsujimura, H. Furutani, and H. Kobayashi, "Control of nox and other emissions in micro gas turbine combustors fuelled with mixtures of methane and ammonia", Combustion and Flame **211**, 406–416 (2020).

[96] Z. Liu, L. Zhou, and H. Wei, "Experimental investigation on the performance of pure ammonia engine based on reactivity controlled turbulent jet ignition", Fuel **335**, 127116 (2023).

[97] K. Uddeen, Q. Tang, H. Shi, G. Magnotti, and J. Turner, "Multiple spark ignition approach to burn ammonia in a spark-ignition engine: an optical study", SAE Technical Paper, 2023-01–0258 (2023).

[98] A. Mercier, C. Mounaïm-Rousselle, P. Brequigny, J. Bouriot, and C. Dumand, "Improvement of si engine combustion with ammonia as fuel: effect of ammonia dissociation prior to combustion", Fuel Communications **11**, 100058 (2022).

[99] S.-Y. Huang, J. Zhou, S.-J. Liu, H.-Y. Peng, and X.-Q. Yuan, "Ammonia/oxygen-enriched air continuous rotating detonation in the hollow chamber", Fuel **311**, 122166 (2022).

[100] S.-Y. Huang, J. Zhou, S.-J. Liu, H.-Y. Peng, and X.-Q. Yuan, "Continuous rotating detonation engine fueled by ammonia", Energy **252**, 123911 (2022).

[101] R. Akbar, M. Kaneshige, E. Schultz, and J. Shepherd, "Detonations in h2-n2o-ch4-nh3-o2-n2 mixtures", Explosion Dynamics Laboratory Report FM97-3, Graduate Aeronautical Laboratories, California Institute of Technology (GALCIT) (1997).

[102] H. D. Ng, "The effect of chemical reaction kinetics on the structure of gaseous detonations", McGill University (2005).

[103] G. Thomas, "Flame acceleration and the development of detonation in fuel–oxygen mixtures at elevated temperatures and pressures", Journal of Hazardous Materials **163**, 783–794 (2009).

[104] G. Thomas, G. Oakley, and R. Bambrey, "An experimental study of flame acceleration and deflagration to detonation transition in representative process piping", Process Safety and Environmental Protection **88**, 75–90 (2010).

[105] Q. Jing, J. Huang, Q. Liu, D. wang, X. Chen, Z. Wang, and C. Liu, "The flame propagation characteristics and detonation parameters of ammonia/oxygen in a large-scale horizontal tube: as a carbon-free fuel and hydrogen-energy carrier", International Journal of Hydrogen Energy **46**, 19158–19170 (2021).

[106] H. Xiao, A. Valera-Medina, and P. J. Bowen, "Modeling combustion of ammonia/hydrogen fuel blends under gas turbine conditions", Energy & Fuels **31**, 8631–8642 (2017).

[107] G. Roy, S. Frolov, A. Borisov, and D. Netzer, "Pulse detonation propulsion: challenges, current status, and future perspective", Progress in Energy and Combustion Science **30**, 545–672 (2004).

[108] M. Hishida, T. Fujiwara, and P. Wolanski, "Fundamentals of rotating detonations", Shock waves **19**, 1–10 (2009).

[109] Z. Sun, Y. Huang, Z. Luan, S. Gao, and Y. You, "Three-dimensional simulation of a rotating detonation engine in ammonia/hydrogen mixtures and oxygen-enriched air", International Journal of Hydrogen Energy **48**, 4891–4905 (2023).

[110] F. Wang, Q. Liu, and C. Weng, "On the feasibility and performance of the ammonia/hydrogen/air rotating detonation engines", Physics of Fluids **35**, 066133 (2023).

[111] O. Kurata, N. Iki, T. Inoue, T. Matsunuma, T. Tsujimura, H. Furutani, M. Kawano, K. Arai, E. C. Okafor, A. Hayakawa, et al., "Development of a wide range-operable, rich-lean low-nox combustor for nh3 fuel gas-turbine power generation", Proceedings of the Combustion Institute **37**, 4587–4595 (2019).

[112] N. Iki, O. Kurata, T. Inoue, T. Matsunuma, T. Tsujimura, H. Furutani, M. Kawano, K. Arai, H. Kobayashi, A. Hayakawa, et al., "Rich-lean combustor

for a 50kw class micro gas turbine firing ammonia", Proceeding Of Global Power And Propulsion Society, 16–18 (2019).

[113] S. Ito, M. Uchida, T. Fujimori, and H. Kobayashi, "Nox emission of two-stage combustor for ammonia/natural gas co-fired gas turbine", 12th Asia-Pacific Conference on Combustion, ASPACC 2019 (2019).

[114] S. Ito, M. Uchida, S. Kato, T. Fujimori, and H. Kobayashi, "Emission characteristics of a lean-premixed ammonia/natural-gas gas-turbine combustor and effect of secondary ammonia injection", Mechanical Engineering Journal **6**, 19-00266-19–00266 (2019).

[115] F. Verkamp, M. Hardin, and J. Williams, "Ammonia combustion properties and performance in gas-turbine burners", Symposium (International) on Combustion **11**, 985–992 (1967).

[116] M. Bull, "Development of an ammonia-burning gas turbine engine", Defense Technical Information Center (1968).

[117] V. Scharl, T. Lackovic, and T. Sattelmayer, "Characterization of ammonia spray combustion and mixture formation under high-pressure, direct injection conditions", Fuel **333**, 126454 (2023).

[118] E. C. Okafor, H. Yamashita, A. Hayakawa, K. K. A. Somarathne, T. Kudo, T. Tsujimura, M. Uchida, S. Ito, and H. Kobayashi, "Flame stability and emissions characteristics of liquid ammonia spray co-fired with methane in a single stage swirl combustor", Fuel **287**, 119433 (2021).

[119] E. C. Okafor, O. Kurata, H. Yamashita, T. Inoue, T. Tsujimura, N. Iki, A. Hayakawa, S. Ito, M. Uchida, and H. Kobayashi, "Liquid ammonia spray combustion in two-stage micro gas turbine combustors at 0.25 mpa; relevance of combustion enhancement to flame stability and nox control", Applications in Energy and Combustion Science **7**, 100038 (2021).

[120] Z. Zhang, W. Long, Z. Cui, P. Dong, J. Tian, H. Tian, and X. Meng, "Visualization study on the ignition and diffusion combustion process of liquid phase ammonia spray ignited by diesel jet in a constant volume vessel", Energy Conversion and Management **299**, 117889 (2024).

[121] K. Somarathne, H. Yamashita, S. Colson, E. Okafor, A. Hayakawa, T. Kudo, and H. Kobayashi, "Liquid ammonia spray combustion and emission characteristics with gaseous hydrogen/air co-firing", Proceedings of the 13th Asia-Pacific Conference on Combustion (2021).

[122] K. D. K. A. Somarathne, H. Yamashita, S. Colson, K. Oku, K. Honda, E. C. Okafor, A. Hayakawa, T. Kudo, and H. Kobayashi, "Towards the development of liquid ammonia/air spray combustion in a gas turbine-like combustor at moderately high pressure", Applications in Energy and Combustion Science **16**, 100215 (2023).

[123] M. T. Lewandowski, M. Pasternak, M. Haugsvær, and T. Løvås, "Simulations of ammonia spray evaporation, cooling, mixture formation and combustion in a direct injection compression ignition engine", International Journal of Hydrogen Energy **52**, 916–935 (2024).

[124] Y. Xu, M. Zhao, and H. Zhang, "Extinction of incident hydrogen/air detonation in fine water sprays", Physics of Fluids **33**, 116109 (2021).

[125] Y. Xu, P. Zhang, Q. Meng, S. Li, and H. Zhang, "Transmission of hydrogen detonation across a curtain of dilute inert particles", Combustion and Flame **254**, 112834 (2023).

[126] H. Watanabe, A. Matsuo, A. Chinnayya, K. Matsuoka, A. Kawasaki, and J. Kasahara, "Numerical analysis of the mean structure of gaseous detonation with dilute water spray", Journal of Fluid Mechanics **887**, A4 (2020).

[127] Z. Weng and R. Mével, "Implementation of an openfoam solver for shock and detonation simulation at high pressure", Computers & Fluids **265**, 106012 (2023).

[128] V. Raman, S. Prakash, and M. Gamba, "Nonidealities in rotating detonation engines", Annual Review of Fluid Mechanics **55**, 639–674 (2023).

[129] H. Xiao and E. S. Oran, "Shock focusing and detonation initiation at a flame front", Combustion and Flame **203**, 397–406 (2019).

[130] R. Zhu, S. Tang, S. Lai, X. Fang, M. Davy, and C. Xu, "Parametric Studies of Deflagration-to-Detonation Transition in a Pre-Chamber/Main-Chamber System", Internal Combustion Engine Division Fall Technical Conference, ASME 2022 ICE Forward Conference, V001T06A003 (2022).

[131] C. J. Roy and J. R. Edwards, "Numerical simulation of a three-dimensional flame/shock wave interaction", AIAA Journal **38**, 745–754 (2000).

[132] A. Dauptain, B. Cuenot, and T. Poinsot, "Large eddy simulation of a supersonic hydrogen-air diffusion flame", Complex Effects in Large Eddy Simulation **71**, 98 (2005).

[133] H. Wang, N. Qin, M. Sun, H. Wu, and Z. Wang, "A hybrid les (large eddy simulation)/assumed sub-grid pdf (probability density function) model for supersonic turbulent combustion", Science China Technological Sciences **54**, 2694–2707 (2011).

[134] P. Boivin, A. Dauptain, C. Jiménez, and B. Cuenot, "Simulation of a supersonic hydrogen–air autoignition-stabilized flame using reduced chemistry", Combustion and Flame **159**, 1779–1790 (2012).

[135] Y. Moule, V. Sabelnikov, and A. Mura, "Highly resolved numerical simulation of combustion in supersonic hydrogen–air coflowing jets", Combustion and Flame **161**, 2647–2668 (2014).

[136] G. Ribert, L. Bouheraoua, and P. Domingo, "Large-eddy simulation of a supersonic burner", 52nd Aerospace Sciences Meeting, 0311 (2014).

[137] L. Bouheraoua, P. Domingo, and G. Ribert, "Large-eddy simulation of a supersonic lifted jet flame: analysis of the turbulent flame base", Combustion and Flame **179**, 199–218 (2017).

[138] Y. P. de Almeida and S. Navarro-Martinez, "Large eddy simulation of a supersonic lifted flame using the eulerian stochastic fields method", Proceedings of the Combustion Institute **37**, 3693–3701 (2019).

[139] L. Chen, W. Yao, and X. Fan, "Influence of compressibility effect on supersonic combustion modeling", AIAA Propulsion and Energy 2019 Forum, 4208 (2019).

[140] T. Cheng, J. Wehrmeyer, R. Pitz, O. Jarrett, and G. Northam, "Raman measurement of mixing and finite-rate chemistry in a supersonic hydrogen-air diffusion flame", Combustion and Flame **99**, 157–173 (1994).

[141] J. Jiang, X. Jiang, and M. Zhu, "A computational study of preferential diffusion and scalar transport in nonpremixed hydrogen-air flames", International Journal of Hydrogen Energy **40**, 15709–15722 (2015).

[142] H. C. Lee, P. Dai, M. Wan, and A. N. Lipatnikov, "Lewis number and preferential diffusion effects in lean hydrogen–air highly turbulent flames", Physics of Fluids **34**, 035131 (2022).

[143] W. Han, V. Raman, and Z. Chen, "Les/pdf modeling of autoignition in a lifted turbulent flame: analysis of flame sensitivity to differential diffusion and scalar mixing time-scale", Combustion and Flame **171**, 69–86 (2016).

[144] A. Aspden, M. Day, and J. Bell, "Lewis number effects in distributed flames", Proceedings of the Combustion Institute **33**, 1473–1480 (2011).

[145] D. Frederick and J. Chen, "Effects of differential diffusion on predicted autoignition delay times inspired by h2/n2 jet flames in a vitiated coflow using the linear eddy model", Flow, turbulence and combustion **93**, 283–304 (2014).

[146] B. Savard and G. Blanquart, "Broken reaction zone and differential diffusion effects in high karlovitz n-c7h16 premixed turbulent flames", Combustion and Flame **162**, 2020–2033 (2015).

[147] S. Lapointe, B. Savard, and G. Blanquart, "Differential diffusion effects, distributed burning, and local extinctions in high karlovitz premixed flames", Combustion and Flame **162**, 3341–3355 (2015).

[148] H. Zhou, T. Yang, and Z. Ren, "Differential diffusion modeling in les/fdf simulations of turbulent flames", AIAA Journal **57**, 3206–3212 (2019).

[149] R. Kai, T. Tokuoka, J. Nagao, A. L. Pillai, and R. Kurose, "Les flamelet modeling of hydrogen combustion considering preferential diffusion effect", International Journal of Hydrogen Energy **48**, 11086–11101 (2023).

[150] D. Eklund, R. Baurle, and M. Gruber, "Numerical study of a scramjet combustor fueled by an aerodynamic ramp injector in dual-mode combustion", 39th aerospace sciences meeting and exhibit, 379 (2001).

[151] X. Xiao, H. A. Hassan, and R. A. Baurle, "Modeling scramjet flows with variable turbulent prandtl and schmidt numbers", AIAA journal **45**, 1415–1423 (2007).

[152] Y. Zheng and C. Yan, "Numerical investigations on the impact of turbulent prandtl number and schmidt number on supersonic combustion", Fluid Dynamics & Materials Processing **16**, 637–650 (2020).

[153] M. C. Burrows and A. P. Kurkov, "An analytical and experimental study of supersonic combustion of hydrogen in vitiated air stream", AIAA Journal **11**, 1217–1218 (1973).

[154] R. Guerra, W. Waidmann, and C. Laible, "An experimental investigation of the combustion of a hydrogen jet injected parallel in a supersonic air stream", 3rd International Aerospace Planes Conference, 5102 (1991).

[155] A. Ingenito and C. Bruno, "Les of a supersonic combustor with variable turbulent prandtl and schmidt numbers", 46th AIAA Aerospace Sciences Meeting and Exhibit, 515 (2008).

[156] J. SMAGORINSKY, "General circulation experiments with the primitive equations: i. the basic experiment", Monthly Weather Review **91**, 99–164 (1963).

[157] C. Dancey, "The turbulent flow field downstream of an axisymmetric mach 2 supersonic burner-lda measurements", 32nd Joint Propulsion Conference and Exhibit, 3073 (1996).

[158] N. Kornev and E. Hassel, "Method of random spots for generation of synthetic inhomogeneous turbulent fields with prescribed autocorrelation functions", Communications in Numerical Methods in Engineering **23**, 35–43 (2007).

[159] N. Kornev, H. Kröger, and E. Hassel, "Synthesis of homogeneous anisotropic turbulent fields with prescribed second-order statistics by the random spots method", Communications in Numerical Methods in Engineering **24**, 875–877 (2008).

[160] S. B. Pope, "Turbulent flows", Cambridge University Press (2000).

[161] A. Masri, S. Pope, and B. Dally, "Probability density function computations of a strongly swirling nonpremixed flame stabilized on a new burner", Proceedings of the Combustion Institute **28**, 123–131 (2000).

[162] M. Ó Conaire, H. J. Curran, J. M. Simmie, W. J. Pitz, and C. K. Westbrook, "A comprehensive modeling study of hydrogen oxidation", International Journal of Chemical Kinetics **36**, 603–622 (2004).

[163] C. Duwig, K.-J. Nogenmyr, C.-k. Chan, and M. J. Dunn, "Large eddy simulations of a piloted lean premix jet flame using finite-rate chemistry", Combustion Theory and Modelling **15**, 537–568 (2011).

[164] M. C. Krol, M. J. Molemaker, and J. V. G. de Arellano, "Effects of turbulence and heterogeneous emissions on photochemically active species in the convective boundary layer", Journal of Geophysical Research: Atmospheres **105**, 6871–6884 (2000).

[165] A. Attili, F. Bisetti, M. E. Mueller, and H. Pitsch, "Effects of non-unity lewis number of gas-phase species in turbulent nonpremixed sooting flames", Combustion and Flame **166**, 192–202 (2016).

[166] L. Muñiz and M. Mungal, "Instantaneous flame-stabilization velocities in lifted-jet diffusion flames", Combustion and Flame **111**, 16–31 (1997).

[167] K. M. Lyons, "Toward an understanding of the stabilization mechanisms of lifted turbulent jet flames: experiments", Progress in Energy and Combustion Science **33**, 211–231 (2007).

[168] L.-Y. Jiang and I. Campbell, "Prandtl/schmidt number effect on temperature distribution in a generic combustor", International Journal of Thermal Sciences **48**, Nano Micro Mini Channels and Computational Heat Transfer, 322–330 (2009).